2013

NONINVASIVE NEAR-INFRARED DIFFUSE OPTICAL MONITORING OF CEREBRAL HEMODYNAMICS AND AUTOREGULATION

Ran Cheng
University of Kentucky, ran.cheng28@gmail.com

STUDENT AGREEMENT:

I represent that my thesis or dissertation and abstract are my original work. Proper attribution has been given to all outside sources. I understand that I am solely responsible for obtaining any needed copyright permissions. I have obtained and attached hereto needed written permission statements(s) from the owner(s) of each third-party copyrighted matter to be included in my work, allowing electronic distribution (if such use is not permitted by the fair use doctrine).

I hereby grant to The University of Kentucky and its agents the non-exclusive license to archive and make accessible my work in whole or in part in all forms of media, now or hereafter known. I agree that the document mentioned above may be made available immediately for worldwide access unless a preapproved embargo applies.

I retain all other ownership rights to the copyright of my work. I also retain the right to use in future works (such as articles or books) all or part of my work. I understand that I am free to register the copyright to my work.

REVIEW, APPROVAL AND ACCEPTANCE

The document mentioned above has been reviewed and accepted by the student's advisor, on behalf of the advisory committee, and by the Director of Graduate Studies (DGS), on behalf of the program; we verify that this is the final, approved version of the student's dissertation including all changes required by the advisory committee. The undersigned agree to abide by the statements above.

Ran Cheng, Student

Guoqiang Yu, Major Professor

Abhijit R. Patwardhan, Director of Graduate Studies

NONINVASIVE NEAR-INFRARED DIFFUSE OPTICAL MONITORING OF
CEREBRAL HEMODYNAMICS AND AUTOREGULATION

DISSERTATION

A dissertation submitted in partial fulfillment of the requirements for the degree of
Doctoral of Philosophy in the College of Engineering at the University of Kentucky

By

Ran Cheng

Lexington, Kentucky

Director: Dr. Guoqiang Yu, Associate professor of Biomedical Engineering

Lexington, Kentucky

2013

ABSTRACT OF DISSERTATION

NONINVASIVE NEAR-INFRARED DIFFUSE OPTICAL MONITORING OF
CEREBRAL HEMODYNAMICS AND AUTOREGULATION

Many cerebral diseases are associated with abnormal cerebral hemodynamics and impaired cerebral autoregulation (CA). CA is a mechanism to maintain cerebral blood flow (CBF) stable when mean arterial pressure (MAP) fluctuates. Evaluating these abnormalities requires direct measurements of cerebral hemodynamics and MAP. Several near-infrared diffuse optical instruments have been developed in our laboratory for hemodynamic measurements including near-infrared spectroscopy (NIRS), diffuse correlation spectroscopy (DCS), hybrid NIRS/DCS, and dual-wavelength DCS flow-oximeter. We utilized these noninvasive technologies to quantify CBF and cerebral oxygenation in different populations under different physiological conditions/manipulations. A commercial finger plethysmograph was used to continuously monitor MAP. For investigating the impact of obstructive sleep apnea (OSA) on cerebral hemodynamics and CA, a portable DCS device was used to monitor relative changes of CBF (rCBF) during bilateral thigh cuff occlusion. Compared to healthy controls, smaller reductions in rCBF and MAP following cuff deflation were observed in patients with OSA, which might result from the impaired vasodilation. However, dynamic CAs quantified in time-domain (defined by rCBF drop/MAP drop) were not significantly different between the two groups. We also evaluated dynamic CA in frequency-domain, i.e., to quantify the phase shifts of low frequency oscillations (LFOs) at 0.1 Hz between cerebral hemodynamics and MAP under 3 different physiological conditions (i.e., supine resting, head-up tilt (HUT), paced breathing). To capture dynamic LFOs, a hybrid NIRS/DCS device was upgraded to achieve faster sampling rate and better signal-to-noise. We determined the best hemodynamic parameters (i.e., CBF, oxygenated and total hemoglobin concentrations) among the measured variables and optimal physiological condition (HUT) for detecting LFOs in healthy subjects. Finally, a novel dual-wavelength DCS flow-oximeter was developed to monitor cerebral hemodynamics during HUT-induced vasovagal presyncope (VVS) in healthy subjects. rCBF was found to have the best sensitivity for the assessment of VVS among the measured variables and was likely the final trigger of VVS. A threshold of ~50% rCBF decline was observed which can completely separate subjects with or without presyncope, suggesting its potential role for predicting VVS. With further development and applications, NIRS/DCS techniques are expected to have significant impacts on the evaluation of cerebral hemodynamics and autoregulation.

Key words: cerebral blood flow (CBF); cerebral oxygenation; cerebral autoregulation (CA); near-infrared spectroscopy (NIRS); diffuse correlation spectroscopy (DCS)

Ran Cheng

Student's Signature

July 29, 2013

Date

NONINVASIVE NEAR-INFRARED DIFFUSE OPTICAL MONITORING OF
CEREBRAL HEMODYNAMICS AND AUTOREGULATION

By

Ran Cheng

<div style="text-align:right">

Guoqiang Yu
Director of Dissertation

Abhijit R. Patwardhan
Director of Graduate Studies

July 29, 2013

</div>

DEDICATION

This work is dedicated to

Qishan

and

Mom & Dad

for their endless support and encouragement over the years

ACKNOWLEDGMENTS

Over the past 5 years, I have received assistance from a great number of individuals. This dissertation would not have been possible without their help.

First and foremost, I would like to thank my advisor, Dr. Guoqiang Yu, for his invaluable mentorship. His dedication, brilliant ideas, broad vision, and critical thinking directed me through the whole training process, and will continue to inspire me in my future work.

Next, I would like to thank the members of my committee, Dr. Abhijit Patwardhan who provided his professional advice in signal processing, Dr. David Randall who helped me link my study results to physiological interpretations, Dr. David Puleo who supported not only my study but also my activities in Biomedical Engineering Society. I also appreciate Dr. Stephen Rankin, who reviewed and commented on my dissertation as an outside examiner.

I would also like to acknowledge my collaborators, Joyce Evans, Drs. Sibu Saha, Hainsworth Shin, Don Hayes, Jr., Abner Rayapati, Alan Daugherty, Siqi Wang, and Xiaoyan Zhang for their encouragement and assistance.

Moreover, I sincerely thank Dr. Yu Shang who had no hesitation to offer help both in my work and daily life. I appreciate Lixin Dong for his willingness to devote himself as research subject for improving my experimental protocol. Thanks go to Daniel Irwin for his careful review and beneficial comments for my manuscripts. I truly appreciate ideas and help from those above as well as all other lab-mates including Youquan Zhao, Yu Lin, Chong Huang, Katelyn Gurley, Lian He, Brad Henry, and Daniel Kameny.

My appreciation further extends to the faculties, staffs and students in the Department of Biomedical Engineering for their help.

Finally, I would like to thank my wife and my parents for their unwavering love and support.

TABLE OF CONTENTS

LIST OF TABLES

LIST OF FIGURES

CHAPTER 1 INTRODUCTION

1.1 Cerebral Hemodynamics and Cerebral Autoregulation (CA) in Health and Disease

Brain is one of the biggest and most complex organs in human which has a high metabolic demand. Maintenance of its normal functions requires the delivery of oxygen and glucose and the clearance of metabolic wastes through cerebral blood flow (CBF) that accounts for ~14% of the cardiac output (i.e., volume of the blood flow pumped out from heart) [1]. To keep CBF stable during blood pressure fluctuations, cerebral vasculatures are regulated by means of myogenic, neurogenic, and metabolic mechanisms; the so-called cerebral autoregulation (CA) [2, 3]. It is known that capillary membrane in cerebral microvasculature is the place where exchanges of nutrition and wastes occur. Therefore, adequate CBF and cerebral oxygenation as well as intact CA in cerebral microvasculature are critical in maintaining normal brain functions.

Many people suffering cerebral, cardiovascular or respiratory diseases are usually associated with abnormal cerebral microvasculature, cerebral hypoxia, and impaired CA. For example, more than 795,000 people in U.S. have stroke every year [4], and tissue hypoxia resulting from the ischemic stroke may damage cerebral microvasculature [5] and impair CA [6]. About 93,000 patients with carotid artery stenosis underwent carotid endarterectomy surgeries in 2009 to prevent stoke [4]. Limited CBF caused by the carotid artery stenosis may lead to impaired CA [7, 8]. Another example is obstructive sleep apnea (OSA) that affects about 15 million American adults [9, 10]. OSA increases the risk of stroke significantly [11] and may result in neurocognitive deficits (e.g.,

impairments in memory, attention, executive functions and constructional abilities) [12] and CA impairment [13].

CA in healthy subjects works in a relatively large range of mean arterial pressure (MAP) fluctuations (60 to 150 mm Hg, see Figure 1.1) [2]. When MAP variation is beyond this range, CA is unable to keep CBF stable. Syncope, which is defined by the sudden loss of consciousness and posture tone, may occur when CA is completely lost [14]. Vasovagal syncope (VVS) is the most common type of syncope [15, 16]. Decreases in blood pressure and heart rate resulting from a malfunction of autonomic nervous system lead to VVS [17]. Early predication of VVS may help people to avoid VVS and consequential accidents. Continuous and simultaneous monitoring of MAP and cerebral hemodynamic variables during VVS may provide critical information for predicting VVS and determining which variable eventually triggers VVS.

1.2 Quantification of CA

CA is usually quantified from the relationships between cerebral hemodynamic parameters (e.g., CBF and cerebral oxygenation) and blood pressure (e.g., MAP, arterial blood pressure (ABP) waveform, systolic blood pressure (SBP), and diastolic blood pressure (DBP)) [2, 18, 19]. Evaluation of CA includes static and dynamic methods, which are classified by whether the MAP and CBF are stable/static or not at the time of measurements [2, 18, 19].
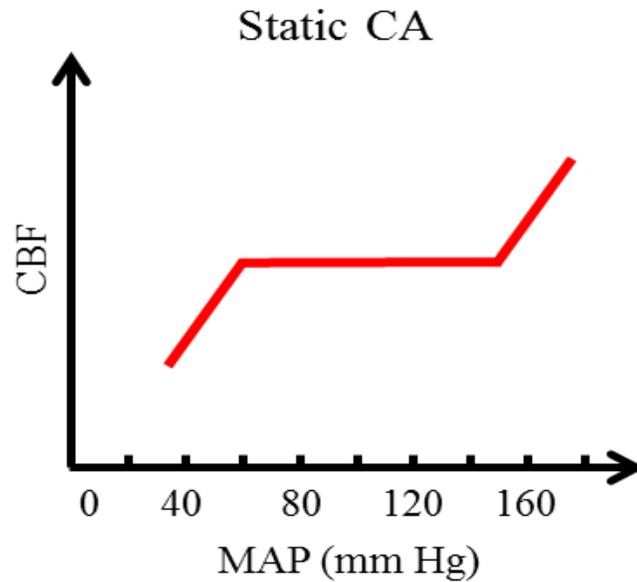
Figure 1.1 Quantification of static CA by simultaneously measuring CBF and MAP over a large range of MAP.

Static CA. Classic CA test was performed in a steady state (so called static CA) where stepwise changes of MAP in the interval of 30 to 180 mmHg were achieved by a pharmacological intervention [18]. CBF was measured for more than 30 seconds at each stable MAP via an indicator-dilution method using inert gas, such as N_2O, ^{85}Kr, or ^{133}Xe [20-22]. MAP was usually assessed by an intravascular catheter [22]. Figure 1.1 shows a typical CA testing result; a constant CBF can be maintained over a large range of 60 to 150 mmHg. The static method does not address the dynamic process of CA, e.g., whether there is a hypoperfusion period between the MAP change and eventual steady state of CBF. Evaluation of static CA is limited in clinic due to its invasive nature and sustained periods of hypotension and hypertension.
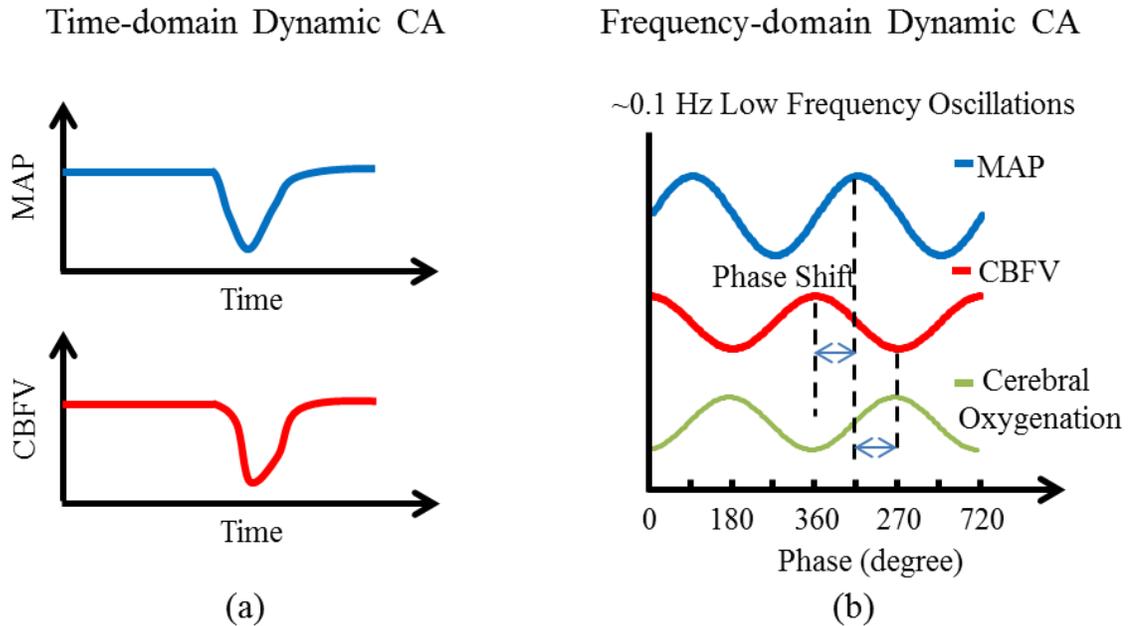
Figure 1.2 Quantification of dynamic CA in time-domain (a) and frequency-domain (b).
Vertical dashed lines in panel (b) indicate the peaks of low frequency oscillations at 0.1 Hz in MAP and cerebral hemodynamics.

Dynamic CA. More recently, researchers have explored a noninvasive method to evaluate CA dynamically through noninvasively quantifying cerebral blood flow velocity (CBFV) by transcranial Doppler (TCD) ultrasound and MAP by finger plethysmography [23, 24]. Analyses of dynamic CA (i.e., the relationship between CBFV and MAP) have been done in both time-domain (TD) and frequency-domain (FD) (Figure 1.2).

In evaluation of TD dynamic CA, an autoregulatory stimulus (e.g., the release of bilateral thigh pressure cuffs or head-up tilt (HUT)) is usually used to induce a sudden change in MAP. During physiological manipulations, dynamic CA in adjusting CBFV during MAP variations is challenged. The cerebral vascular conductance change, expressed as CBFV change/MAP change, is often used to determine dynamic CA. A

lower cerebral vascular conductance change indicates a better CA since less CBFV variation is caused by a unit MAP change. Figure 2.1a shows the analysis of TD dynamic CA by monitoring instantaneous responses of MAP and CBFV in major cerebral artery (MCA) to an autoregulatory stimulus (i.e., a rapid deflation of bilateral thigh pressure cuffs) that results in a sudden MAP drop [23].

It has been shown that low frequency oscillations (LFOs) of CBFV and cerebral oxygenation at ~0.1 Hz are related to similar intrinsic LFO presented in ABP [7, 25, 26]. Although the origin of LFOs in ABP and cerebral hemodynamics remains unclear, studies have found that brain exhibits myogenic [27], metabolic [28] and neurogenic [29] oscillations in the same low frequency range, which are dominated by sympathetic nervous system activity. The myogenic, metabolic, and neurogenic controls are three main mechanisms responsible for CA. Thus, evaluation of phase shift (i.e. time interval) between the LFOs of MAP and cerebral hemodynamics holds potential for assessing dynamic CA in FD [7, 18]. For example, Reinhard et al found a decrease/increase of phase lead/lag between LFOs in CBFV/cerebral oxygenation and MAP in patients with carotid artery stenosis [7]. According to the report by Hu et al, less phase lead between LFOs in CBFV and MAP was found in patients with higher degree carotid artery stenosis (i.e., narrow carotid artery) [8]. Figure 1.2b shows the analysis of FD dynamic CA through detecting the phase shifts of LFOs in MAP, CBFV, and cerebral oxygenation.

Current evaluations of dynamic CA in TD and FD are mostly limited to assess CA in large arteries (e.g., MCA), which does not always reflect the CA in cerebral microvasculature [30]. Furthermore, quantification of the relationships among CBF, cerebral oxygenation, and MAP under different physiological conditions/manipulations

5

may determine the most sensitive parameter(s) and robust protocol(s) for assessing dynamic CA in cerebral microvasculature. This dissertation focuses on the noninvasive evaluation of dynamic CAs in both TD and FD via simultaneously and continuously monitoring multiple cerebral hemodynamic parameters and MAP under different physiological conditions/manipulations.

1.3 Noninvasive Measurements of Cerebral Blood Flow (CBF) and Cerebral Oxygenation

Various noninvasive techniques have been attempted to monitor CBFV or CBF in human including TCD [31], xenon-enhanced computer tomography (XeCT) [32], dynamic perfusion computed tomography (PCT) [33], single photon emission computed tomography (SPECT) [34], positron emission tomography (PET) [35], arterial spin labeled MRI (ASL-MRI) [36], and dynamic susceptibility contrast MRI (DSC-MRI) [37]. TCD is widely used, but limited to measure CBFV in large vessels, which may not be consistent with CBF in microvasculature [38]. However, many cerebral diseases such as stroke and neurocognitive impairment are associated with abnormal microvasculature and tissue dysfunction in brain [39, 40]. Moreover, TCD measurements are not applicable for approximately 9% of adults due to their having poor acoustic windows [41]. Other techniques mentioned above use either endogenous (e.g., ASL-MRI) or exogenous tracers (e.g., PET, SPECT, XeCT, PCT, DSC-MRI) to evaluate CBF in microvasculature. However, those large imaging modalities are expensive and have relatively low temporal resolutions and poor mobility.

Noninvasive techniques for measuring cerebral oxygenation in human include blood oxygen level dependent MRI (BOLD-MRI) [42] and near-infrared spectroscopy (NIRS) tissue oximeter [43]. Both techniques are sensitive to cerebral oxygenation in microvasculature. Again, although BOLD-MRI can image cerebral hemodynamics with high spatial resolution, the high cost, low temporal resolution, and poor mobility limit its frequent use in clinic. By contrast, the inexpensive, portable, and easy-to-use NIRS allows for fast and longitudinal measurements at the bedside of clinic, although its spatial resolution is relatively low.

Since cerebral hemodynamic parameters (e.g., CBF and cerebral oxygenation) are usually coupled and interactive, it is desirable to simultaneously measure multiple hemodynamic variables and investigate their complex relationships. Combination measurements have been reported previously using NIRS, PET [44], ASL-MRI [45], and BOLD-MRI [46]. Nevertheless, inexpensive, portable, fast, and easy-to-use devices are needed for continuous and simultaneous measurements of both CBF and cerebral oxygenation at the bedside of clinic.

1.4 Near-infrared Spectroscopy (NIRS)

NIRS provides a noninvasive, rapid, portable, and low-cost alternative to monitor tissue oxygenation (including oxy-hemoglobin concentration ($[HbO_2]$), deoxy-hemoglobin concentration ($[Hb]$), total hemoglobin concentration (THC), blood oxygen saturation (StO_2)), which makes it ideal for research and clinical uses [47-50].
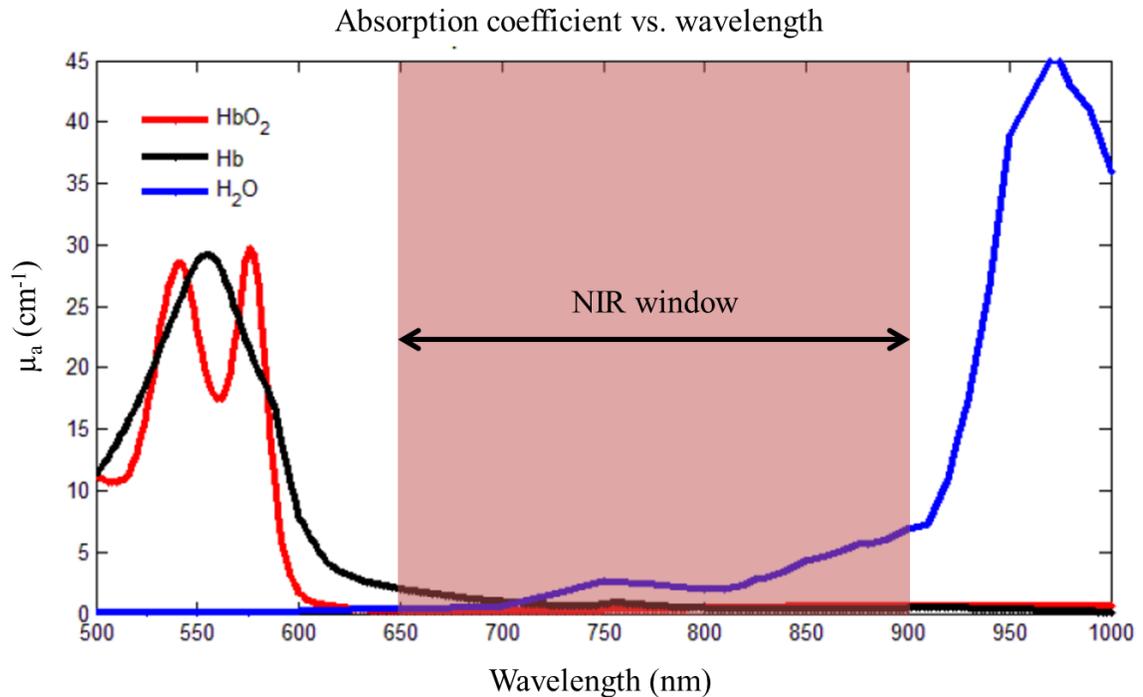
Figure 1.3 Absorption spectra of hemoglobin and water.
Tissue absorption coefficients (μ_a) are shown as a function of wavelength (λ). The oxygenated hemoglobin (HbO_2), deoxygenated hemoglobin (Hb), and water (H_2O) are major absorbers in biological tissues. Within the NIR spectral window (650 to 900 nm), light can penetrate tissues deeply due to the relatively low tissue absorption.

NIRS uses NIR light in the range of 650 to 900 nm where tissue absorption is relatively low (Figure 1.3). Therefore, NIR light can penetrate deep tissues up to several centimeters. Absorption and scattering occur when NIR photons interact with the tissue absorbers (e.g., HbO_2, Hb, H_2O) and scatterers (e.g., cell membranes, organelles, nuclei). Here HbO_2 represents the hemoglobin bound to four oxygen molecules, Hb represents the hemoglobin without binding of O_2 [51, 52], and H_2O represents water. NIR light transported in tissues is dominated by scattering events rather than absorption and can be approximated as a diffusive process (Chapter 2.1). Tissue optical properties are

characterized by absorption and reduced scattering coefficients, represented by μ_a and μ_s' (cm^{-1}), respectively.
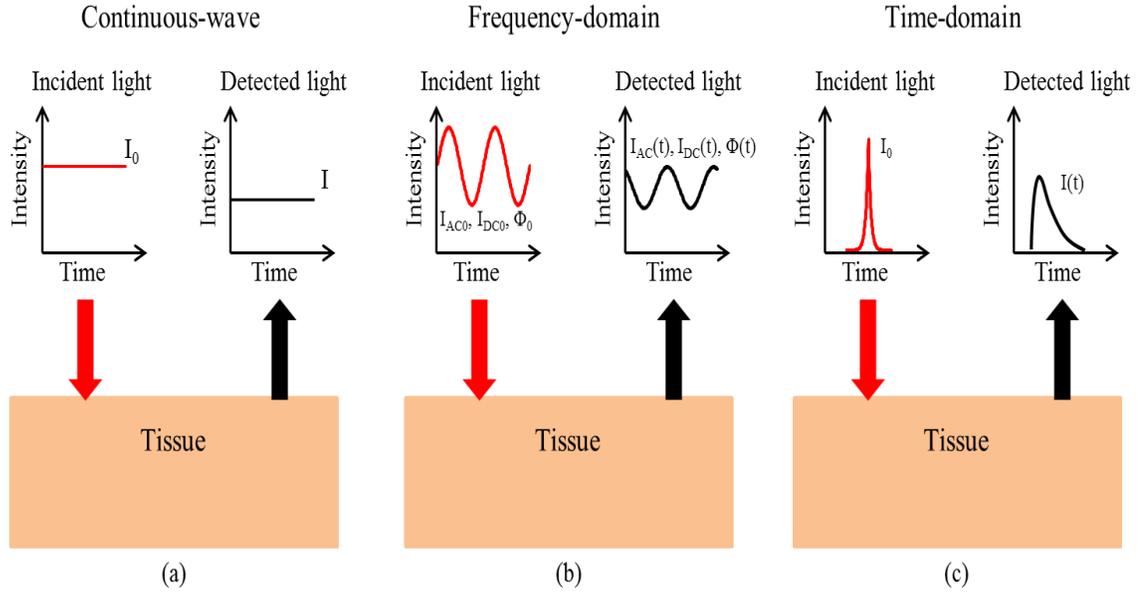
Figure 1.4 Three types of NIRS tissue oximeters.
Panel (a) shows a continuous-wave (CW) NIRS, in which attenuated intensity of continuous illumination light is monitored. Panel (b) represents a frequency-domain (FD) NIRS, in which incident light is modulated and the amplitude attenuation and phase shifts due to tissue absorption and scattering are detected. Here, I, I_{DC}, and I_{AC} represent light intensity, averaged intensity, and peak-to-peak intensity, respectively. Φ represents the phase of modulated light. Panel (c) demonstrates a time-domain (TD) NIRS, in which an impulse of light is emitted into the tissue, and the intensity change with respect to time is detected.

Three types of NIRS devices are currently used for diffuse optical measurements, which are classified based on the types of light sources utilized [53]. The continuous-wave (CW) system is the simplest approach which uses a CW light source (Figure 1.4a). The photodetector measures the attenuated light intensity caused by tissue absorption and scattering. The FD system utilizes an amplitude-modulated light source at a radio-frequency range (10 to 1000 MHz) and measures the light intensity reductions including

a DC component (average intensity) and an AC component (peak-to-peak intensity) as well as phase shift relative to the incident light. The TD system employs a very short pulse source (~100 ps) and detects the temporal broaden and delay of the output pulse [54].

Among the three paradigms, CW system is simplest and least expensive [55], but it provides only information of relative changes in [Hb], [HbO$_2$], and THC (i.e., Δ[Hb], Δ[HbO$_2$], and ΔTHC) [56]. FD technique enables quantification of absolute values of μ_a and μ_s', thus providing absolute assessments of [Hb], [HbO$_2$], THC, and StO$_2$. TD measurement provides more information than CW and FD systems (e.g., tissue properties at different depths) with the cost of expensive and complex instrumentation.

1.5 Near-infrared (NIR) Diffuse Correlation Spectroscopy (DCS)

DCS is a relatively new technique for CBF measurements [6, 38, 57-64]. Similar to NIRS (Figure 1.4), DCS uses NIR light to penetrate deep tissues. However, the light source used in DCS is a CW laser with long coherence length (> 5 meter) and the detector used is the very sensitive single-photon-counting avalanche photodetector (APD). DCS detector detects light intensity fluctuations at a single speckle area on the tissue surface using a single-mode fiber connected to the APD. Interactions between photons and moving scatterers (primarily red blood cells in microvasculature) result in light intensity fluctuations at a single speckle area. Through quantification of the time scale of light intensity fluctuation, DCS generates a blood flow index (BFI) which is related to the motion of red blood cells (Chapter 2.3). Relative change of blood flow

(rBF) is determined subsequently by normalizing time-course BFI data to its baseline value before the physiological change.

DCS for rBF measurements has been extensively validated against other techniques in various organs/tissues, including TCD in premature infant brain [65, 66], power spectral Doppler ultrasound in murine tumors [67], laser Doppler flowmetry in rat and mouse brains [68, 69], fluorescent microsphere measurement of CBF in piglet brain [70], ASL-MRI in human brain and muscle [71, 72], and Xenon computed tomography in traumatic brain [73].

1.6 Current Study Limitations

Quantification of dynamic CA requires simultaneous measurements of MAP and cerebral hemodynamic variables including CBF and cerebral oxygenation. Although many techniques are capable of measuring cerebral hemodynamics, current studies of dynamic CA are mostly limited to evaluate CA in large cerebral vessel (e.g., MCA) using CBFV measured by TCD [13]. It is known that abnormal microvasculature and tissue hypoxia have been observed in cerebral diseases associated with impaired CA [74, 75]. Although researchers have attempted to assess dynamic CA in microvasculature through measuring cerebral tissue oxygenation by NIRS [7], cerebral oxygenation changes may not be consistent with CBF variations. In addition, previous studies usually evaluate dynamic CA from one single hemodynamic parameter (e.g., CBFV or cerebral oxygenation). However, cerebral hemodynamic parameters are usually interactive. Therefore, concurrent measurements of multiple cerebral hemodynamic parameters are critical for the evaluation of CA.

Our strategy to overcome above limitations is to develop various noninvasive NIR diffuse optical instruments for simultaneous measurements of multiple cerebral hemodynamic parameters. The instruments that we have developed and/or built include a portable single-wavelength DCS flowmeter, a portable dual-wavelength DCS flow-oximeter, and a large hybrid NIRS/DCS device. The custom-made DCS flowmeter can directly measure CBF in the microvasculature of frontal cortex. Both custom-designed hybrid NIRS/DCS and DCS flow-oximeter can simultaneously measure variations in CBF and cerebral oxygenation. Although the hybrid NIRS/DCS provides absolute measurements of cerebral oxygenation, it is more expensive and larger than the portable DCS flow-oximeter. We then applied these instruments with different experimental protocols/stimuli (e.g., bilateral thigh pressure cuff occlusion or HUT) to evaluate dynamic CA in different populations (e.g., patients with OSA or healthy controls). The ultimate goal is to find the most sensitive cerebral hemodynamic parameters and most robust protocols for evaluating cerebral hemodynamics and dynamic CA.

This thesis is organized with the following chapters. Chapter 2 introduces the theory and instrumentation of NIRS and DCS technologies. Chapter 3 describes a study using a DCS flowmeter to evaluate TD dynamic CA in patients with OSA. Chapter 4 demonstrates the feasibility of evaluating FD dynamic CA using the phase shifts of LFOs between the MAP and cerebral hemodynamics (CBF and cerebral oxygenation) measured by an upgraded hybrid NIRS/DCS instrument. Chapter 5 depicts diffuse optical monitoring of cerebral hemodynamics during VVS in healthy subjects using a novel dual-wavelength DCS flow-oximeter. Finally, Chapter 6 summarizes the novelties of the

present studies and my contributions to the field, discusses study limitations, and eventually points out future study directions.

CHAPTER 2 THEORY AND INSTRUMENTATION OF NIR DIFFUSE OPTICAL TECHNILOGIES

Several NIR diffuse optical instruments have been recently developed in our laboratory and used in the studies covered by this dissertation, including a single-wavelength DCS flowmeter, a hybrid NIRS/DCS device which integrates a commercial FD NIRS oximeter (Imagent, ISS Inc., IL, USA) and a custom-made CW DCS flowmeter [76], and a novel custom-designed dual-wavelength DCS flow-oximeter [77]. The single-wavelength DCS flowmeter measures only CBF while both hybrid NIRS/DCS and dual-wavelength DCS flow-oximeter are able to monitor both CBF and cerebral oxygenation. The hybrid NIRS/DCS device can quantify absolute values of cerebral oxygenation including $[HbO_2]$, $[Hb]$, THC, and StO_2. DCS flow-oximeter can detect relative changes of cerebral oxygenation including $\Delta[HbO_2]$, $\Delta[Hb]$, and ΔTHC. The dimensions/costs of the single-wavelength DCS flowmeter and dual-wavelength DCS flow-oximeter are similar, but much smaller/less than the hybrid NIRS/DCS.

2.1 Basics of NIR Diffuse Optical Techniques

When using NIR diffuse optical techniques to detect cerebral oxygenation or CBF, a pair of source and detector fibers is usually placed on the tissue surface with a distance of a few millimeters to centimeters. NIR light generated by a laser transmits into tissues through the source fiber (Figure 2.1). Based on the diffusion theory, photons transported in highly scattered biological tissues can be treated as a diffusive process [78, 79]. More specifically, some photons may be absorbed by tissue absorbers including hemoglobin, and water while more photons are scattered by tissue scatterers including cell membranes,

organelles, and nuclei. Only a few photons can be scattered back to the tissue surface and detected by the photodetector through the detector fiber. The penetration depth of NIR light in biological tissues is approximately half of the source-detector (S-D) separation (ρ) [80, 81]. NIRS measures the amplitude reductions and phase shifts (for a FD system) at multiple wavelengths to extract tissue blood oxygenation information [80, 81]. DCS blood flow measurement is accomplished by monitoring light intensity fluctuations (caused by the motion of red blood cells) at a single speckle area on tissue surface using a single-mode detection fiber [82-84].
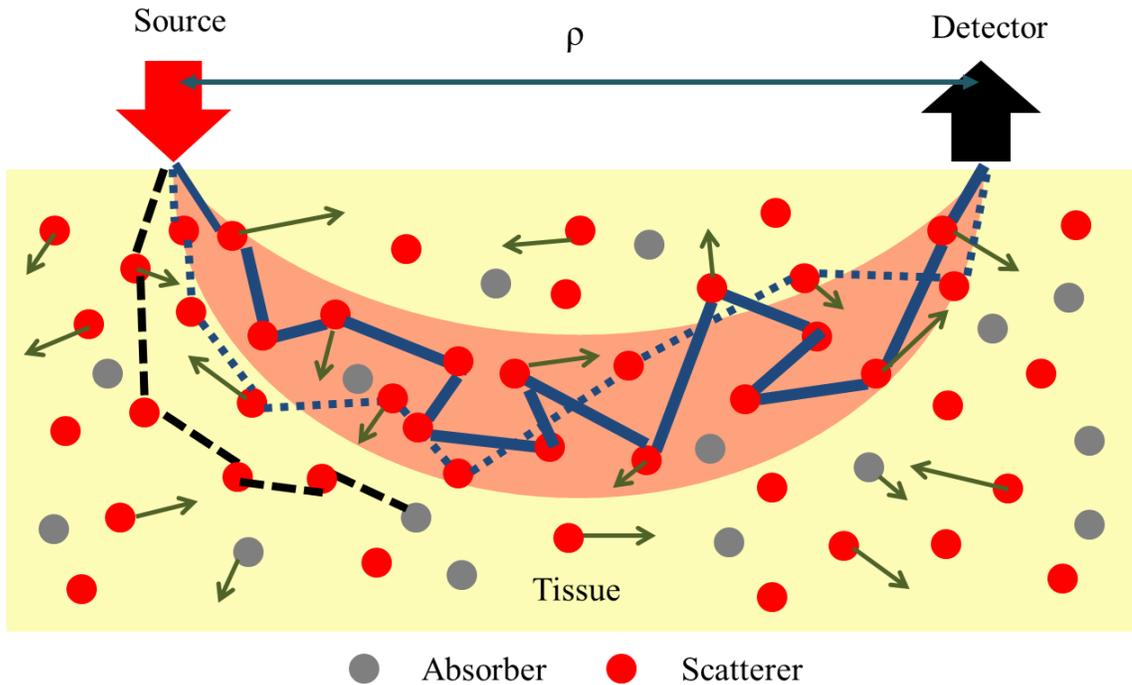
Figure 2.1 Photons transported in tissue experience absorption and scattering events.
The source and detector fibers are placed on the tissue surface at a distance ρ. Grey and red dots represent tissue absorbers (e.g., hemoglobins and water) and scatterers (e.g., cell membranes, organelles, and nuclei), respectively. The green arrows represent the moving directions of moving scatterers (primarily red blood cells). The solid and dashed blue lines indicate potential paths of the detected photons. The dashed black lines indicate the

potential paths of the photons absorbed by tissue absorbers. The pink banana shadow area indicates the average path of the detected photons.

2.2 NIRS for Cerebral Blood Oxygenation Measurement

Different physical models have been used to describe photon transportation in biological tissues, including a complex photon diffusion equation [78, 84] and a simple modified Beer-Lambert law (MBLL) [85]. One can extract either absolute μ_a using the photon diffusion equation or relative change of μ_a ($\Delta\mu_a$) using the MBLL. The measured μ_a or $\Delta\mu_a$ is then decomposed into the absorption contributions from different tissue chromophores:

$$\mu_a(\lambda) = \sum_i \varepsilon_i(\lambda) c_i \tag{2.1}$$

$$\Delta\mu_a(\lambda) = \sum_i \varepsilon_i(\lambda) \Delta c_i \tag{2.2}$$

Here $\varepsilon_i(\lambda)$ is the known molar extinction coefficient at wavelength (λ) for the ith chromophore. c_i is the concentration of the ith chromophore and Δc_i.is the change of c_i. The sum is over tissue chromophores which are mainly HbO_2 and Hb. Water (H_2O) absorption usually does not change much and is thus fixed based on the literature [86]. Two unknown chromophore's concentrations (or concentration changes) require the measurements at minimum two wavelengths. Using measured absolute concentrations of HbO_2 and Hb, one can further calculate THC and StO_2:

$$THC = [HbO_2] + [Hb] \tag{2.3}$$

$$StO_2 = [HbO_2]/THC*100\% \tag{2.4}$$

2.2.1 Theory of Continuous-wave (CW) NIRS

In CW NIRS, MBLL is often used to describe the change in light intensity due to $\Delta\mu_a$. The MBLL is written as:

$$\Delta OD(\lambda) = \log[I_B(\lambda)/I_T(\lambda)] = \Delta\mu_a(\lambda) * photon\ pathlength \qquad (2.5)$$

where $\Delta OD(\lambda)$ is the change in optical density measured at a given wavelength (λ), and $I_B(\lambda)$ and $I_T(\lambda)$ are the measured baseline and transient light intensities, respectively. $\Delta\mu_a(\lambda)$ results from the concentration changes in absorbing species (mainly [HbO$_2$] and [Hb]), and thus can be written as:

$$\Delta\mu_a(\lambda) = \varepsilon_{HbO_2}(\lambda)\Delta[HbO_2] + \varepsilon_{Hb}(\lambda)\Delta[Hb] \qquad (2.6)$$
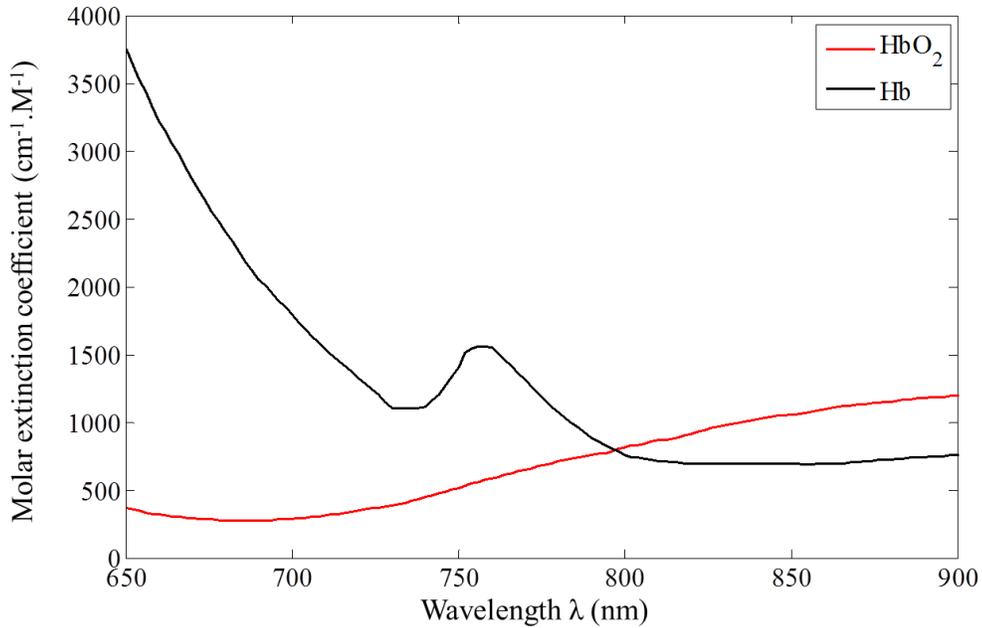
Figure 2.2 Wavelength-dependent molar extinction coefficients (cm^{-1}·M^{-1}) of oxygenated hemoglobin (HbO$_2$) and deoxygenated hemoglobin (Hb) in NIR window of 650 to 900 nm.

Here, $\varepsilon_{HbO}(\lambda)$ and $\varepsilon_{Hb}(\lambda)$ are molar extinction coefficients of HbO_2 and Hb at wavelength λ (Figure 2.2). Due to scattering effects, the pathlengths of detected photons are usually longer than the S-D separation ρ (Figure 2.1). The increased distance that light travels from the source to the detector can be determined by a differential pathlength factor (DPF):

$$\text{photon pathlength} = \rho * DPF(\lambda) \tag{2.7}$$

where $\varepsilon_{HbO_2}(\lambda)$, $\varepsilon_{Hb}(\lambda)$, and $DPF(\lambda)$ can be found from the literature [87].

Using the measured light intensity changes at two wavelengths (λ_1 and λ_2) and Equations 2.5 to 2.7, one can derive $\Delta[HbO_2]$ and $\Delta[Hb]$ in a unit of μM relative to their baselines (assigned to be 0):

$$\begin{bmatrix} \log[I_B(\lambda_1)/I_T(\lambda_1)] \\ \log[I_B(\lambda_2)/I_T(\lambda_2)] \end{bmatrix} = \begin{bmatrix} \varepsilon_{HbO_2}(\lambda_1) & \varepsilon_{Hb}(\lambda_1) \\ \varepsilon_{HbO_2}(\lambda_2) & \varepsilon_{Hb}(\lambda_2) \end{bmatrix} \begin{bmatrix} \Delta[HbO_2] \\ \Delta[Hb] \end{bmatrix} * \rho * DPF \tag{2.8}$$

Here μM represents $\mu mol/L$ and ΔTHC can be calculated by the sum of $\Delta[HbO_2]$ and $\Delta[Hb]$.

2.2.2 Instrumentation of CW NIRS

Figure 2.3 shows the schematics of a typical CW NIRS system. A transistor–transistor logic (TTL) signal is used to switch the two NIR sources/wavelengths alternately; only one source is on at a time. The photodetector senses the light intensity change which is associated with $\Delta\mu_a$. We can then extract $\Delta[HbO_2]$, $\Delta[Hb]$, and ΔTHC from the measured $\Delta\mu_a$ at the two wavelengths. The optical probe consists of an optical detector and two light sources.
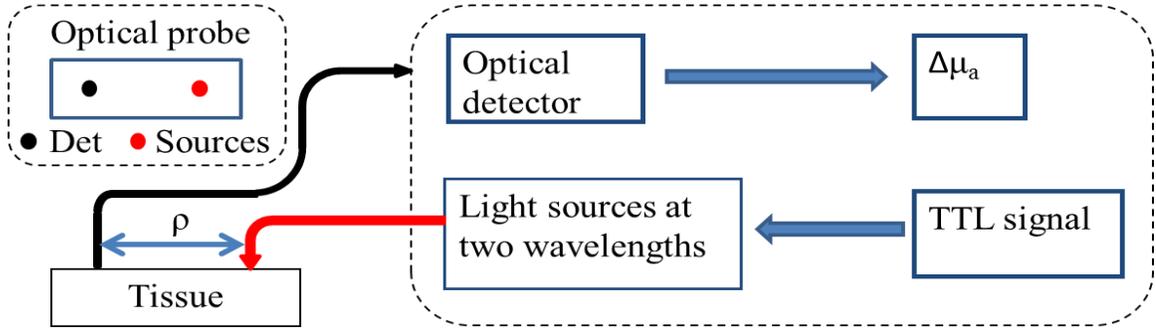
Figure 2.3 Schematics of a typical CW NIRS system.

2.2.3 Theory of Frequency-domain (FD) NIRS

Photon diffusion equation. Photon transportation in biological tissues can be approximately treated as a diffusing process because scattering events dominate photon propagation inside the tissue [78, 79]. μ_s' is often much larger (>10 folds) than μ_a in biological tissues. If one tracks the trajectory of each photon inside the tissue using Monte Carlo simulation, a random walking pattern would be observed. Photon propagation inside tissue as a diffusive process can be described by the photon diffusion equation [78, 88]. Specifically, the measured photon fluence rate $\Phi(r,t)$ (photons/[s·cm^2]) obeys the time-dependent photon diffusion equation in a homogeneous medium [78, 84, 88, 89]:

$$D\nabla^2\Phi(r,t) - v\mu_a\Phi(r,t) + vS(r,t) = \frac{\partial\Phi(r,t)}{\partial t} \tag{2.9}$$

Here v (cm/s) is the speed of light in medium and $D = v/3(\mu_a + \mu_s')$ (cm^2/s) is the photon diffusion coefficient. S(r, t) (photons/[s·cm^3]) is an isotropic source term which gives the number of photons emitted at position r and time t per unit volume per unit time. The right hand side (RHS) of Equation 2.9 shows the changing rate of photons

19

within a sample volume. This rate equals the number of photons scattered into the volume per unit time from its surroundings (the first term on the left hand side (LHS) of Equation 2.9), *minus* the number of photons absorbed per unit time within the volume (the second term on the LHS), *plus* the number of photons emitted per unit time from any sources in the volume (the third term on the LHS) [84].

In case of FD NIRS, a frequency modulated source is used. Then the source term S(r,t) and photon fluence rate $\Phi(r, t)$ are written as

$$S(r, t) = \left(S_{DC} + S_{AC}e^{-i\omega t}\right)\delta(r) \tag{2.10}$$

$$\Phi(r, t) = \Phi_{DC}(r) + \Phi_{AC}(r)e^{-i(\omega t - \varphi(r))} \tag{2.11}$$

where S_{DC} and S_{AC} are DC and AC components of source power indicating the number of photons emitted in unit time. ω is the modulation frequency (e.g., 110 MHz for the Imagent device). φ represents the phase difference between the source and detected lights. Substituting the S(r,t) and $\Phi(r, t)$ in Equation 2.9 with those in Equations 2.10 and 2.11, we can get the following two equations for the DC and AC components [76]:

$$D\nabla^2\Phi_{DC}(r) - v\mu_a\Phi_{DC}(r) + vS_{DC}\delta(r) = 0 \tag{2.12}$$

$$D\nabla^2\Phi_{AC}(r)e^{-i(\omega t - \varphi(r))} - v\mu_a\Phi_{AC}(r)e^{-i(\omega t - \varphi(r))} + vS_{AC}e^{-i\omega t}\delta(r)$$
$$= -i\omega\Phi_{AC}(r)e^{-i(\omega t - \varphi(r))} \tag{2.13}$$

Equations 2.12 and 2.13 can be further simplified as [76]:

$$\left(\nabla^2 - \frac{v\mu_a}{D}\right)\Phi_{DC}(r) = -\frac{vS_{DC}\delta(r)}{D} \tag{2.14}$$

$$\left[\nabla^2 - \frac{v\mu_a - i\omega}{D}\right]\Phi_{AC}(r) = -\frac{vS_{AC}e^{-i\varphi(r)}\delta(r)}{D} \tag{2.15}$$

Homogeneous solutions of photon diffusion equation in infinite tissue geometry. Analytical solutions of Φ_{DC}, Φ_{AC}, and φ for homogeneous medium with infinite geometry (see Figure 2.4a) are derived in **Appendix I**. Linear relations exist between $ln[\Phi_{DC}(\rho) \cdot \rho]$, $ln[\Phi_{AC}(\rho) \cdot \rho]$, or $\varphi(\rho)$ and ρ [76]:

$$ln[\Phi_{DC}(\rho) \cdot \rho] = -\rho \left(\frac{v\mu_a}{D}\right)^{1/2} + \ln\left(\frac{S_{DC}}{4\pi D}\right) \tag{2.16}$$

$$ln[\Phi_{AC}(\rho) \cdot \rho] = -\rho \left(\frac{v\mu_a}{2D}\right)^{1/2} \left[(1+x^2)^{1/2} + 1\right]^{1/2} + \ln\left(\frac{S_{AC}}{4\pi D}\right) \tag{2.17}$$

$$\varphi(\rho) = \rho \left(\frac{v\mu_a}{2D}\right)^{1/2} \left[(1+x^2)^{1/2} - 1\right]^{1/2} \tag{2.18}$$

where x is defined as $\omega/v\mu_a$. The slopes (SL_{AC}, SL_{DC}, SL_φ) of these linear regression can be fitted from the measured $ln[\Phi_{DC}(\rho) \cdot \rho]$, $ln[\Phi_{AC}(\rho) \cdot \rho]$, and $\varphi(\rho)$ at different ρ (e.g., ρ = 2.0, 2.5, 3.0, and 3.5 cm for the Imagent device, see Chapter 2.2.4). Meanwhile, these slopes are functions of μ_a and μ_s' (note that $D = v/3(\mu_a + \mu_s')$) according to the first terms on the RHS of Equations 2.16 to 2.18 [76].

$$SL_{DC} = -\left(\frac{v\mu_a}{D}\right)^{1/2} \tag{2.19}$$

$$SL_{AC} = -\left(\frac{v\mu_a}{2D}\right)^{1/2} \left[(1+x^2)^{1/2} + 1\right]^{1/2} \tag{2.20}$$

$$SL_\varphi = \left(\frac{v\mu_a}{2D}\right)^{1/2} \left[(1+x^2)^{1/2} - 1\right]^{1/2} \tag{2.21}$$

Therefore, μ_a and μ_s' can be extracted from the measured SL_{DC}, SL_{AC}, and SL_φ, using Equations 2.19 to 2.21. Since there are three equations and only two unknowns, any two slopes can be used. In practice, however, the small difference between SL_{DC} and

SL_{AC} observed in tissues prevents the use of this pair. SL_{AC} and SL_φ pair is often used, because SL_{AC} is less influenced by room light. Using SL_{AC} and SL_φ, we have [76]

$$\mu_a = \frac{\omega}{2v}\left(\frac{SL_\varphi}{SL_{AC}} - \frac{SL_{AC}}{SL_\varphi}\right) \tag{2.22}$$

$$\mu_{s'} = \frac{v\left(SL_\varphi{}^2 - SL_{AC}{}^2\right)}{3\mu_a} - \mu_a \tag{2.23}$$

Compared to the CW NIRS measurements, absolute values of μ_a and μ_s' at different wavelengths quantified by FD NIRS allow us to extract absolute values of cerebral oxygenation (i.e., [HbO$_2$], [Hb], THC, StO$_2$) using Equations 2.1, 2.3, and 2.4.
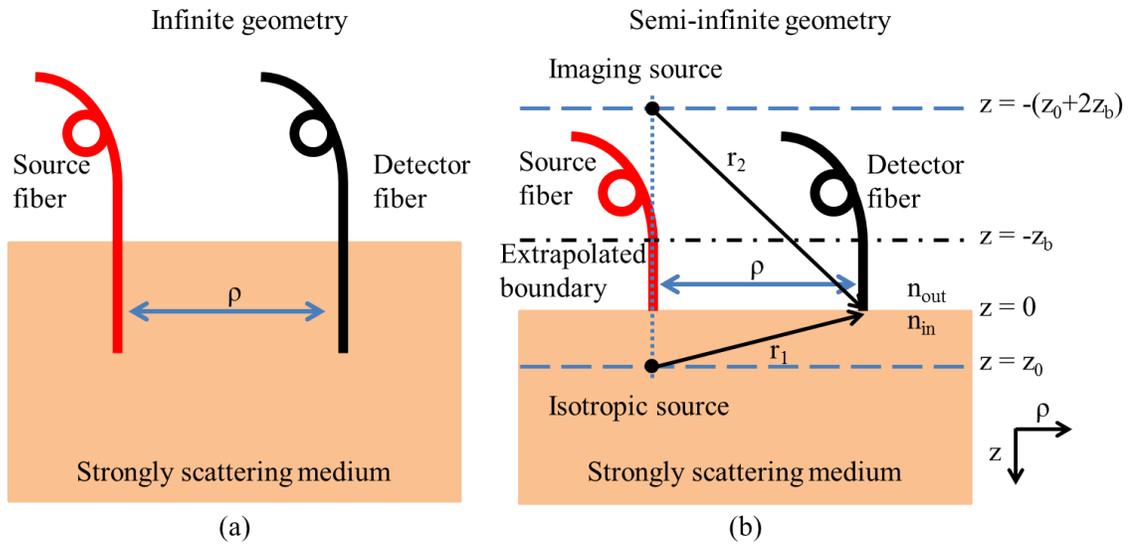
Figure 2.4 Illustration of infinite (a) and semi-infinite (b) geometries to solve the photon diffusion equation (see also Appendix I).

Homogeneous solutions in semi-infinite geometry. The infinite geometry is often not practical for *in vivo* tissue measurements. The solutions derived in semi-infinite geometry of homogenous medium (Figure 2.4b) is usually used for noninvasive real tissue measurements. A collimated light source is usually approximated as an isotropic

source located at $z = z_0 = 1/\mu_s$' inside the medium, as the direction of photon movement becomes random after its first scattering event [90].

The physical boundary condition at the interface between the scattering (e.g., biological tissues) and non-scattering (e.g., air) media is that there are no incoming photons at the boundary. Apparently, a mismatch of the refraction index at the interface of the strongly scattering medium (n_{in}) and the outside non-scattering medium (n_{out}) accounts for an inwardly directed component of the photon flux (J_{in}) at the boundary. An extrapolated zero boundary ($-z_b$) in the non-scattering medium where $J_{in}(z = -z_b) = 0$, can be determined from the zero partial flux boundary condition [91-93]:

$$J_{in}(r) = \frac{1}{4}\Phi(r) + \frac{D}{2v}\frac{1 - R_{eff}}{1 + R_{eff}}\frac{\partial\Phi(r)}{\partial\hat{n}} = 0 \qquad (2.24)$$

Here, R_{eff} = $-1.44n^{-2}$ + $0.71n^{-1}$ + 0.668 + 0.064n is the effective reflection coefficient determined by the ratio of refraction indices inside and outside the scattering medium, $n = n_{in}/n_{out} \simeq 1.33$ [90], and $\hat{n}$ is the vector normal to the boundary. Then $-z_b =$

$-\frac{2}{3\mu_s}\frac{1+R_{eff}}{1-R_{eff}}$ is extrapolated from Equation 2.24. For semi-infinite homogeneous geometry, the extrapolated zero boundary condition is satisfied by placing a negative isotropic imaging source located at $z = -(z_0 + 2z_b)$ (Figure 2.4b) [84].

The analytical solutions of Φ_{DC}, Φ_{AC}, and φ in semi-infinite geometry are derived in **Appendix I**. μ_a and μ_s' can be fitted iteratively from the analytical solutions although iterations are often time consuming. Therefore, faster approximate solutions defined by the following equations are often employed [94]:

$$ln[\Phi_{DC}(\rho)\cdot\rho^2] = \rho SL_{DC} + K_{DC} \qquad (2.25)$$

$$ln[\Phi_{AC}(\rho) \cdot \rho^2] = \rho SL_{AC} + K_{AC} \qquad (2.26)$$

$$\varphi(\rho) = \rho SL_{\varphi} + K_{\varphi} \qquad (2.27)$$

where SL_{DC}, SL_{AC}, and SL_φ are defined in Equations 2.19 to 2.21 and can be fitted from the measured $ln[\Phi_{DC}(\rho) \cdot \rho^2]$, $ln[\Phi_{AC}(\rho) \cdot \rho^2]$, and $\varphi(\rho)$ at different ρ. K_{DC}, K_{AC}, and Kφ are ρ-independent functions. μ_a and μ_s' can then be calculated using Equations 2.22 and 2.23 [94]. Finally, [HbO$_2$], [Hb], THC, and StO$_2$ can be calculated from the measured μ_a at different wavelengths (e.g., 690 and 830 nm for the Imagent device, see Chapter 2.2.4).

2.2.4 Instrumentation of FD NIRS
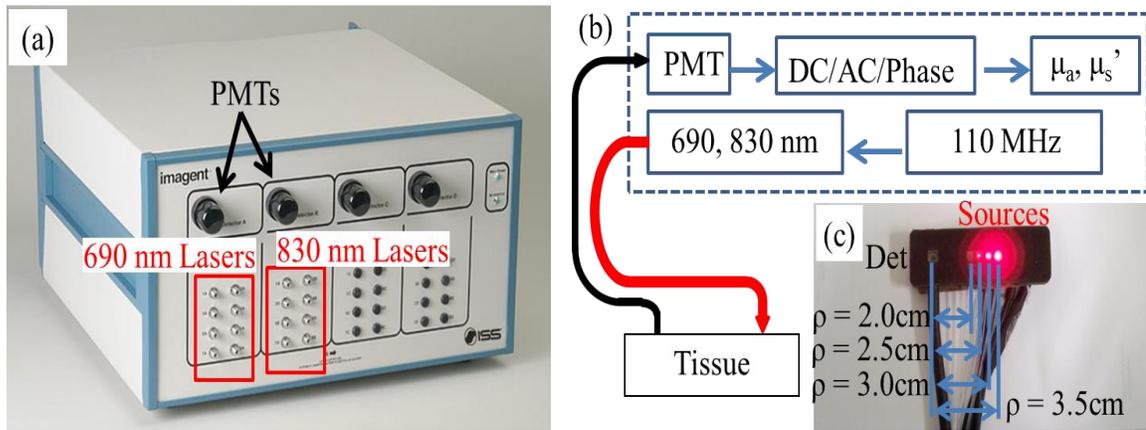
Figure 2.5 Photo (a) and schematics (b) of a commercial FD NIRS (Imagent, Iss Inc., IL, USA) and picture of a fiber-optic probe (c).

In this study a commercial FD NIRS (Imagent, Iss Inc., IL, USA) was used (Figure 2.5) which contains two banks of multiplexed sources (each bank has eight laser diodes at the same wavelength) and two photomultipliers (PMT) detectors. The two

detectors work in parallel and each serves its own multi-distance probe ($\rho = 2.0, 2.5, 3.0$, and 3.5 cm). The fiber-optic probe is optically coupled to laser-diode sources by multi-mode fibers (core diameter = 400 um). A large fiber bundle (core diameter = 2.5 mm) connected to the PMT is used to detect the reflected light from the tissue. Laser-emitted lights at 690 and 830 nm are modulated at 110 MHz and multiplexed so that only one source in each bank is on at a time. Φ_{DC}, Φ_{AC}, and φ are measured and used to calculate μ_a and $\mu_s{}'$ (at both wavelengths) and hemoglobin concentration values. Typically, the measurement time for each cycle covering all source-detector pairs and wavelengths is 150 ms. Data from several cycles can be averaged to improve signal-to-noise ratio (SNR) when high sampling rate is not necessary.

2.3 DCS for CBF Measurement

Similar to NIRS, DCS also utilizes NIR light to penetrate deep tissues. However, NIRS monitors tissue blood oxygenation variations through quantifying the relatively slow changes in light intensity level and phase (for FD system) due to the slow changes in tissue absorption and scattering, whereas DCS monitors directly the motion of moving scatterers (mainly red blood cells) in tissue through quantifying the fast temporal fluctuations in light intensity. Therefore, DCS is considered as a "dynamic NIR technique" as opposed to the "static NIRS".

2.3.1 Theory of DCS

DCS, also known as diffusing wave spectroscopy (DWS) [95, 96], originated from the single dynamic light scattering (DLS) technique. DLS has been widely applied to study particle suspension properties (e.g., particle size and shape) in optically thin physical systems. Later, Boas et al [82-84] derived a correlation diffusion equation from the correlation transport theory [97, 98], which described the propagation of unnormalized electric field temporal autocorrelation function in highly scattered turbid medium. **Appendix II** describes the derivation of correlation diffusion equation from both single scattering and multiple scattering events.

In most experiments, the normalized temporal intensity autocorrelation function, $g_2(r,\tau) = \langle I(r,t) \cdot I(r,t+\tau) \rangle / \langle I(r,t) \rangle^2$, is calculated from the detected intensity fluctuations of scattered light. Here r is the location vector which denotes a general vector from a source to a point of detection, and τ represents the delay time of autocorrelation function. $g_2(r,\tau)$ is related to the normalized electric field temporal autocorrelation function, $g_1(\tau)$, through the Siegert relationship [99]:

$$g_2(r,\tau) = 1 + \beta|g_1(r,\tau)|^2 \tag{2.28}$$

where β depends on laser stability and coherence length and the number of detected speckles, which can be determined experimentally from the measured $g_2(r,\tau)$ via $\beta = g_2(r,0) - 1$. The unnormalized electric field temporal autocorrelation is defined by

$$G_1(r,\tau) = g_1(r,\tau) \cdot G_1(r,0) = g_1(r,\tau) \cdot I(r,0) \tag{2.29}$$

The motions of moving scatterers in biological tissue (mainly red blood cells) contribute to the exponential decay of G_1. The transport of G_1 results in the following *correlation diffusion equation* in homogeneous medium for CW light source [82-84].

$$\left[\nabla^2 - \left(3\mu_a\mu_s' + \mu_s'^2 k_0^2 \langle \Delta r^2(\tau)\rangle\right)\right]G_1(r,\tau) = -\frac{vS_0\delta(r)}{D} \qquad (2.30)$$

Here $D \simeq v/3\mu_s'$. $S_0\delta(r)$ is the CW source term, where S_0 is a constant. $\langle\Delta r^2(\tau)\rangle$

is the mean-square displacement of moving scatterers in delay time τ. The scatterer

movement combining with photon absorption (i.e., $3\mu_a\mu_s' + \mu_s'^2 k_0^2 \langle\Delta r^2(\tau)\rangle$) gives an

effective "absorption" term for the attenuation of G_1 as it travels through the medium. The

formal similarity of Equation 2.14 (i.e., $(\nabla^2 - \frac{v\mu_a}{D})\Phi_{DC}(r) = -\frac{vS_{DC}\delta(r)}{D}$) and Equation

2.30 suggest that their solutions are also formally similar. In a semi-infinite homogeneous

medium (Figure 2.4b), analytical solutions of $G_1(r,\tau)$ and $g_1(r,\tau)$ can be obtained [84]:

$$G_1(\rho,\tau) = \frac{vS_0 e^{i\omega\tau}}{4\pi D}\left(\frac{e^{-K(\tau)r_1}}{r_1} - \frac{e^{-K(\tau)r_2}}{r_2}\right) \qquad (2.31)$$

$$g_1(\rho,\tau)_{analytical} = \frac{G_1(\rho,\tau)}{G_1(\rho,0)}$$

$$= \left(\frac{e^{-K(\tau)r_1}}{r_1} - \frac{e^{-K(\tau)r_2}}{r_2}\right) \Big/ \left(\frac{e^{-K(0)r_1}}{r_1} - \frac{e^{-K(0)r_2}}{r_2}\right) \qquad (2.32)$$

Here ρ is the S-D separation, $r_1 = \sqrt{\rho^2 + z_0^2}$, $r_2 = \sqrt{\rho^2 + (z_0 + 2z_b)^2}$ (Figure

2.4b), $z_0 = \frac{1}{\mu_s'}$, $z_0 = \frac{2}{3\mu_s'}\frac{1+R_{eff}}{1-R_{eff}}$, R_{eff} = -1.44n^{-2} + 0.71n^{-1} + 0.668 + 0.064n, n = n_{in}/n_{out}

(e.g., n = 1.33/1 for biological tissue/air interface) is the same as the previous definition

in Chapter 2.2.3, and $K(\tau) = 3\mu_a\mu_s' + \mu_s'^2 k_0^2 \langle\Delta r^2(\tau)\rangle$, where $k_0 = 2\pi n/\lambda$. Meanwhile,

the measured $g_1(\rho,\tau)_{measured}$ can be converted from the measured $g_2(\rho,\tau)$ using the

Siegert Relation [99] (Equation 2.28).

To adapt the correlation diffusion equation for the use in biological tissues, a

unitless factor α (ranging from 0 to 1) is introduced to represent the ratio of light

scattering events resulted from "moving" scatterers (e.g., red blood cells) to the total

scatterers, since some of the scatterers in tissue are "static" (e.g., organelles, mitochondria, and nuclei). The factor α is included as a pre-fix to $\langle \Delta r^2(\tau) \rangle$ (i.e., $\alpha \langle \Delta r^2(\tau) \rangle$) to indicate the mean square displacement of "moving" scatterers in biological tissues. Then $g_1(\rho, \tau)$ depends on $K(\tau) = 3\mu_a \mu_s' + \mu_s'^2 k_0^2 \alpha \langle \Delta r^2(\tau) \rangle$ and thus is a function of tissue optical properties (μ_a and μ_s') and the mean-square-displacement of the "moving" scatterers ($\alpha \langle \Delta r^2(\tau) \rangle$). By assuming from literature or measuring the values of μ_a and μ_s' by NIRS, $g_1(\rho, \tau)$ is solely determined by the term of $\alpha \langle \Delta r^2(\tau) \rangle$.

For the case of diffusive motion, $\alpha \langle \Delta r^2(\tau) \rangle = 6\alpha D_b \tau$, where D_b is the *effective* Brownian diffusion coefficient of tissue scatterers, and is distinct from the well-known thermal Brownian diffusion coefficient [100]. By varying αD_b in the $g_1(\rho, \tau)_{analytical}$ and fitting it to $g_1(\rho, \tau)_{measured}$, one can extract αD_b. Practically, we have observed that the diffusion model, i.e. $\langle \Delta r^2(\tau) \rangle = 6D_b \tau$, fits the autocorrelation curves rather well than the random flow model over a broad range of tissue types, ranging from mouse brain [69] and mouse muscle [101, 102], adult human skeletal muscle [77, 103-106], adult human tumors [107], and adult brain [25, 63]. The reason for the Brownian-motion like correlation curve is still not apparent and more investigations are needed to understand its underlying mechanism. Nevertheless, DCS tissue blood flow measurements have been adopted by many researchers in biomedical field [25, 30, 60, 61, 81, 108-110].

Although the unit of αD_b (cm^2/s) is different from the traditional blood perfusion unit [ml/min/100 g], relative changes in this blood flow index ($rBF = BFI/BFI_0$) have been found to correlate quite well with other blood flow measurement modalities [65-73] (see also Chapter 1.5), where BFI_0 is the baseline flow value measured before the physiological change.

2.3.2 Instrumentation of DCS
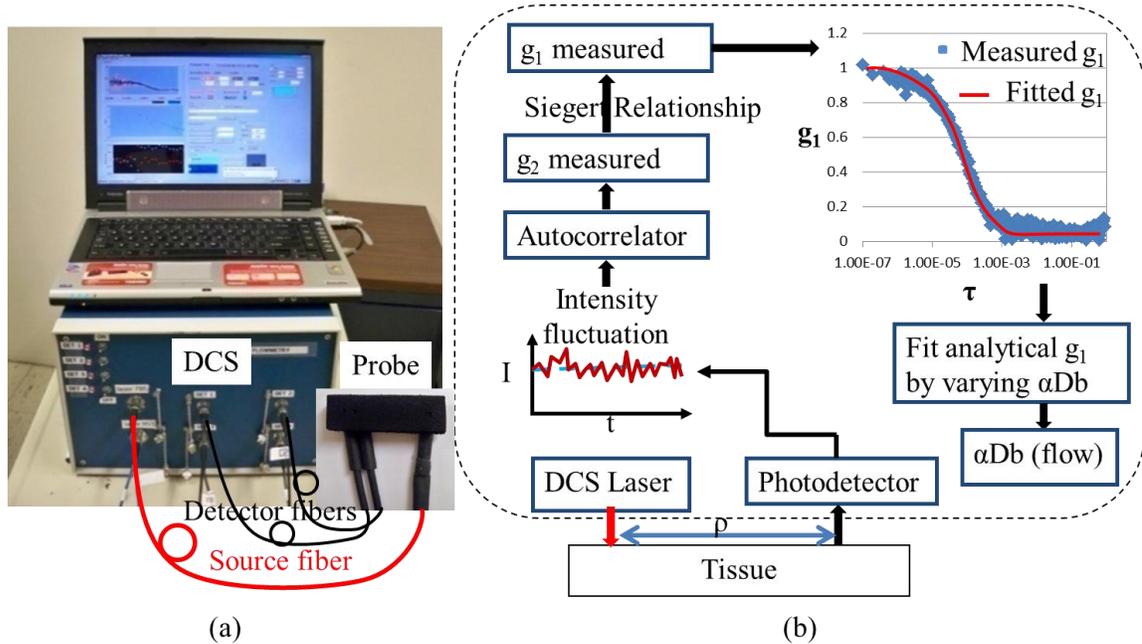
Figure 2.6 A typical 4-channel DCS device (a) and a diagram for DCS data processing (b).

Figure 2.6a shows a typical 4-channel DCS device consisting of a CW long-coherence (> 5 m) laser at 785 nm (100 mw, CrystaLaser Inc., NV, USA), 4 single-photon-counting avalanche photodiodes (APDs) (e.g., Perkin Elmer Inc., Canada), and an autocorrelator board (Correlator.com, NJ, USA). The laser diode shines the light through a multi-mode source fiber (diameter = 200 μm) into the tissue (Figure 2.6b). In a single speckle area on the tissue surface, the temporal light intensity variations caused by the moving scatterers (primarily red blood cells in the microvasculature) are detected by a single-mode fiber (diameter = 5 μm) connected to one of the APDs. The output of the APD is sent to an autocorrelator board for calculating the normalized light intensity temporal autocorrelation function (g_2), which is then converted to the normalized electric

field temporal autocorrelation function (g_1) for the quantification of αD_b (see the data processing diagram shown in Figure 2.6b).

A fiber-optic probe is usually made using source and detector fibers confined by a custom-designed soft foam pad (Figure 2.6a). The S-D separation is selected according to the tissue depth probed (e.g., $\rho = 2.5$ cm for adult brain measurements [25, 38, 61, 63, 64, 68, 108], $\rho = 0.6$ cm for mouse skeletal muscle measurements [69, 111]). The sampling rate of DCS also varies according to specific applications. For example, we have used a fast sampling rate of 2 Hz for quantifying LFOs in CBF [25] and a low sampling rate of 0.33 Hz for measuring rBF in calf muscle during thigh cuff occlusion [77]. There is generally a tradeoff between the sampling rate and SNR. The faster the sampling rate is, the less the light intensity detected associated with a lower SNR. In addition, both spatial and temporal averaging can improve the SNR.

2.4 Hybrid NIRS/DCS Instruments

As mentioned in Chapter 1, there is a critical need for simultaneous measurements of CBF and cerebral oxygenation. Previously, Yodh's group at the University of Pennsylvania combined a custom-made homodyne FD NIRS instrument with a DCS device for simultaneous measurements of tissue blood flow and oxygenation [57, 110, 112]. However, the homodyne detection system used for NIRS measurements had lower SNR than heterodyne FD NIR systems (e.g., Imagent, ISS Inc. IL, USA). Our group has initially attempted combination of the heterodyne FD Imagent (ISS Inc.) and DCS device (Figure 2.7) to improve the SNR [77].
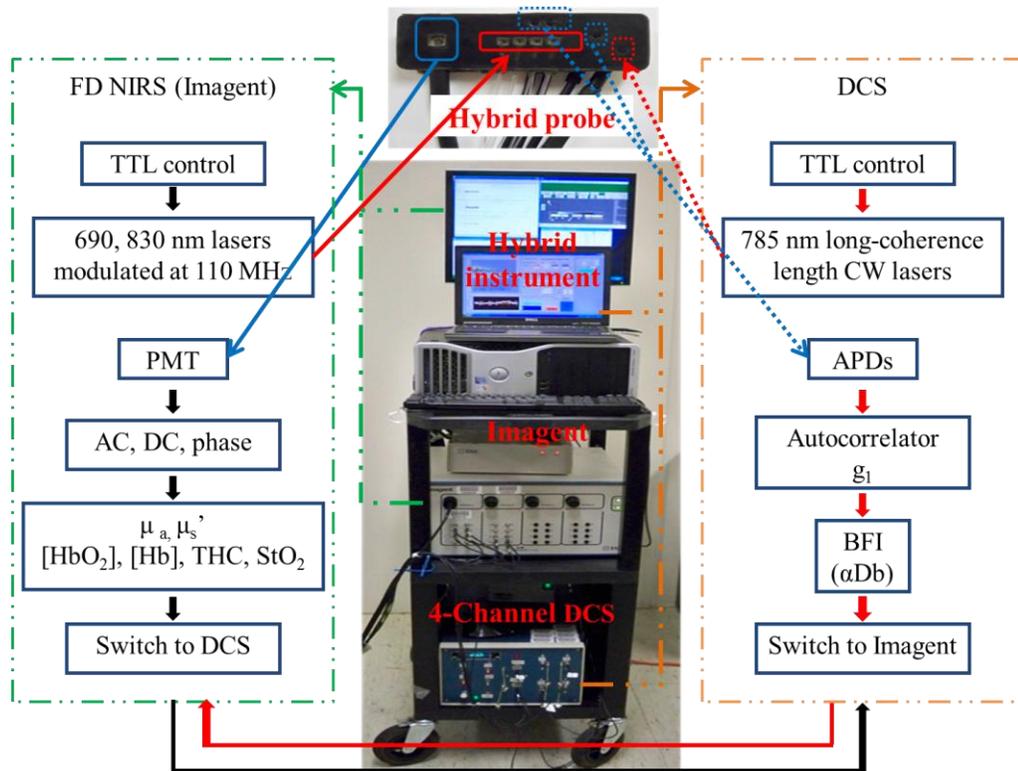
Figure 2.7 A typical hybrid NIRS/DCS instrument consisting of a commercial tissue oximeter (Imagent) and a custom-made 4-channel DCS flowmeter.

First generation hybrid NIRS/DCS instrument. Figure 2.7 shows the picture and diagram of our first generation hybrid Imagent/DCS instrument. Computer-controlled TTL signals were used to control the Imagent and DCS devices working sequentially. Acquisition times for Imagent and DCS measurements can be varied based on the needs for different studies. A 50 ms delay between the transition of Imagent and DCS measurements was set to avoid the potential cross-measurement interference. The design of the hybrid fiber-optic probe was based on the commercial Imagent probe (Figure 2.8). DCS source and detector fibers were housed inside the Imagent probe. The optical fibers for the DCS measurement were arranged in a particular pattern (Figure 2.8) for reducing the interference between DCS and NIRS measurements [77]. The probe regions and

penetration depths for CBF and cerebral oxygenation measurements are slightly different due to this specific probe design. Using this hybrid system, we have successfully quantified blood flow and blood oxygenation in brain [113], skeletal muscle [77, 103, 104, 114], head and neck tumor [107]. Since then [77], several other groups have also built similar hybrid Imagent/DCS systems for their studies [64, 66, 115].
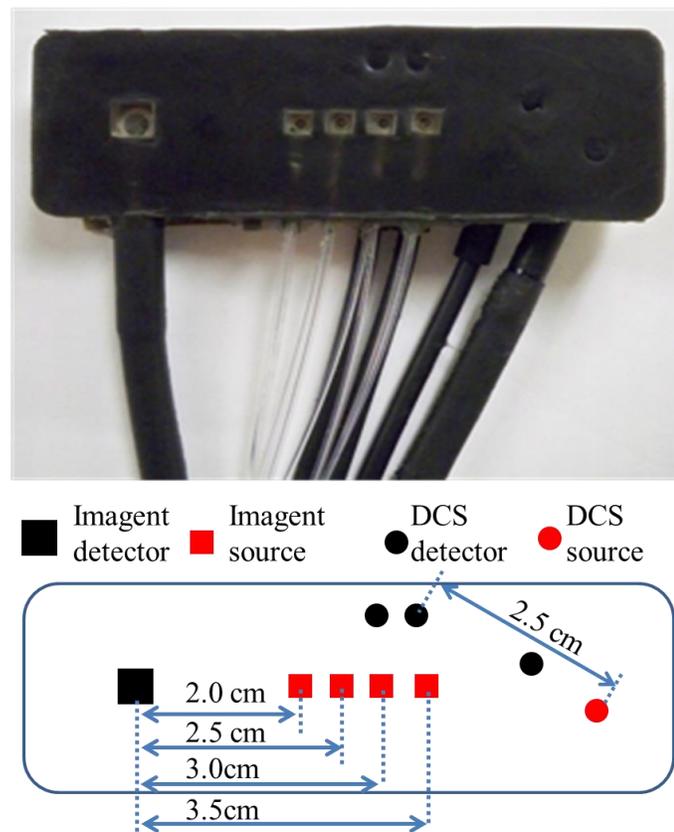
Figure 2.8 A typical fiber-optic probe used in the hybrid NIRS/DCS device.

Upgraded hybrid NIRS/DCS instrument. High sampling rate and SNR of optical measurements are needed to capture instantaneous changes in cerebral hemodynamics (e.g., LFO signals) for evaluation of dynamic CA (Chapter 4). For these purposes, an upgraded hybrid NIRS/DCS instrument was designed and built (Figure 2.9).

Instead of using a continuous-mode autocorrelator board in the first generation hybrid instrument (Figure 2.7), a new autocorrelator board capable of working in both continuous and burst modes (Correlator.com, NJ, USA) was adopted for DCS measurements. The autocorrelator communicated with DCS control panel (a laptop computer) through a USB port (Figure 2.9). The least time (6.5 ms) to obtain a correlation function curve using the burst mode was much shorter than that (104 ms) using the continuous mode. As a result, the burst mode increased the sampling rate by 16 times compared to the continuous mode. In addition, working in the burst mode the autocorrelator started only once at the beginning of data collection (Figure 10a). By contrast, the autocorrelator working in continuous mode restarted repeatedly for the collection of each correlation curve (Figure 10b). Frequent rebooting of the autocorrelator under continuous mode consumed time, thus significantly reducing the efficiency of data collection. Furthermore, more DCS detectors (16 detection channels) were added to the upgraded hybrid instrument, which allowed for spatial averaging of DCS signals to improve the SNR of DCS measurements (Chapter 4). Theoretically, spatial averaging signals from N detection channels can increase the SNR of CBF measurements by $\sqrt{N}$ times.
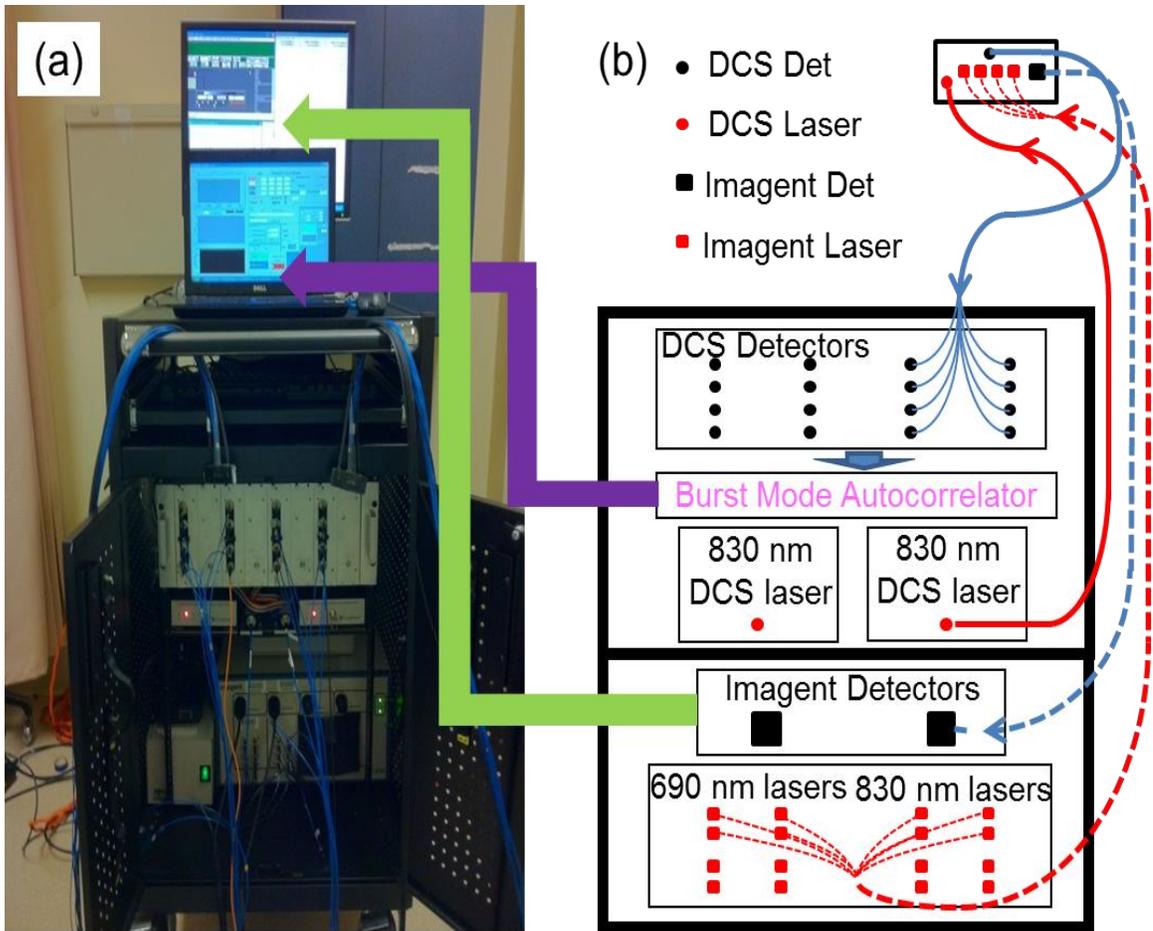
Figure 2.9 Photo (a) and diagram (b) of an upgraded hybrid NIRS/DCS instrument.
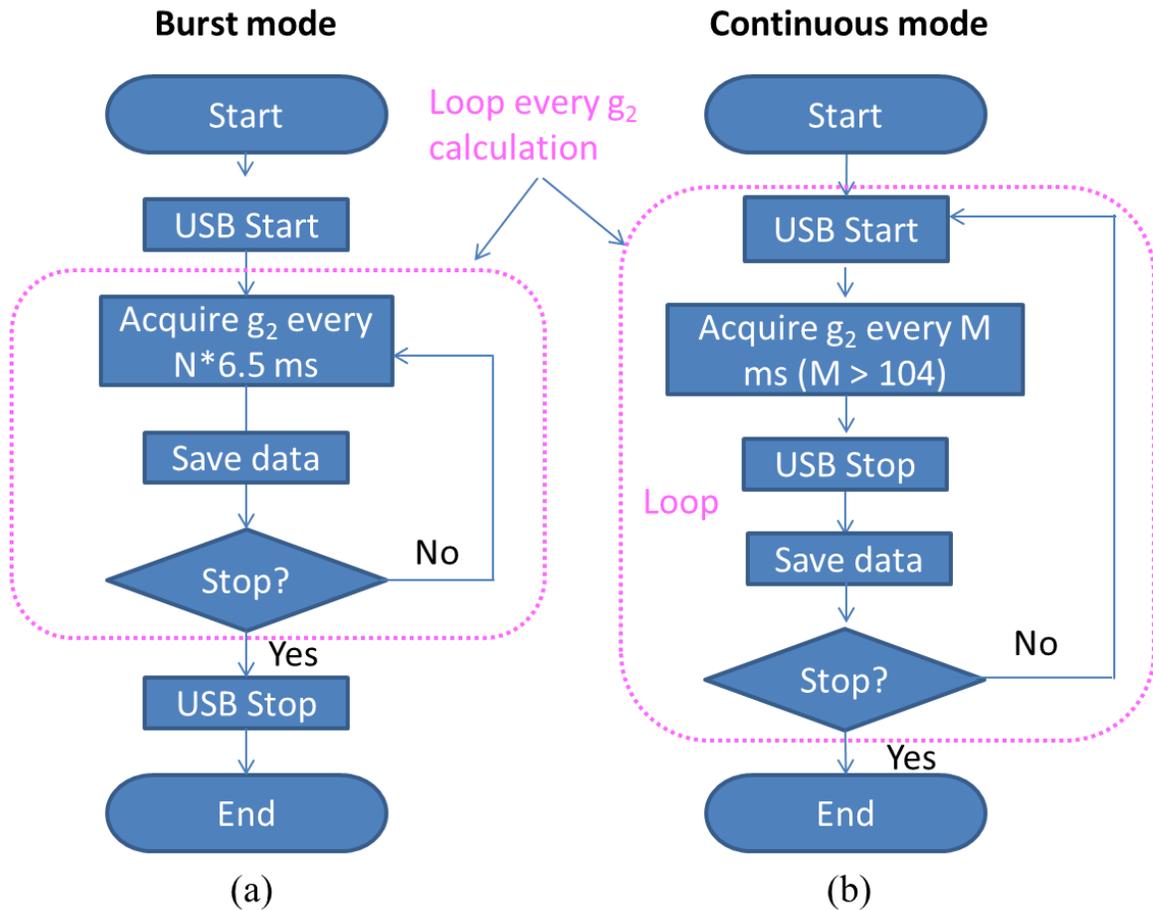
Figure 2.10 Flow charts of burst (a) and continuous (b) modes of an autocorrelator board.

Two identical hybrid fiber-optic probes (Figure 2.9b) were built for detecting both CBF and cerebral oxygenation changes in the left and right hemispheres of brain, respectively. For CBF measurements, each probe contained one DCS source fiber (diameter = 200 μm) connected to a laser diode at 830 nm and 8 single-mode fibers (core diameter = 5.6 μm) that were tightly bundled for detecting light intensity fluctuations at a small area (~0.16 mm^2). Signals from the 8 APDs were averaged to increase the SNR of DCS measurements [59]. Tissue heterogeneity within this small detection area can be

ignored. The S-D separation of DCS fibers was set to 2.5 cm, which allowed for the detection of CBF in adult prefrontal cortex [38, 61, 63, 64, 71, 108]. For cerebral oxygenation measurements, each probe contained 8 Imagent source fibers (4 per wavelength) connected to laser diodes and one detection fiber coupled to one PMT. The source fibers (diameter = 400 μm) were arranged at distances of 2.0, 2.5, 3.0, 3.5 cm from the detector fiber (diameter = 2.5 mm).

To avoid the light interference between flow and oxygenation measurements, the lasers for DCS and Imagent measurements were turned on sequentially in each probe. However, bilateral measurements in the two hemispheres were conducted simultaneously since the light emitted from one probe did not affect the detectors in another probe. The sampling time for one frame of cerebral hemodynamic data was ~500 ms (equivalent to a sampling rate f_s = 2 Hz) which included ~150 ms for DCS measurement, ~250 ms for Imagent measurement, and ~100 ms for switching between the two measurements. The data acquisition and communication between the two devices (through digital I/O lines) were automatically controlled by custom-designed software installed on the two control panels (computers) for DCS and Imagent, respectively [77, 81, 103].

2.5 Dual-wavelength DCS Flow-oximeter

Although the hybrid NIRS/DCS systems can effectively quantify both CBF and cerebral oxygenation, it is relative expensive, large and complicated to build and operate. In addition, the probing regions of CBF and cerebral oxygenation measurements are slightly different duo to the location discrepancy of Imagent and DCS fibers (Figure 2.8). A portable dual-wavelength DCS flow-oximeter was recently developed in our

laboratory, which can simultaneously measure the relative changes in CBF and cerebral oxygenation from the same region of tissues [77].
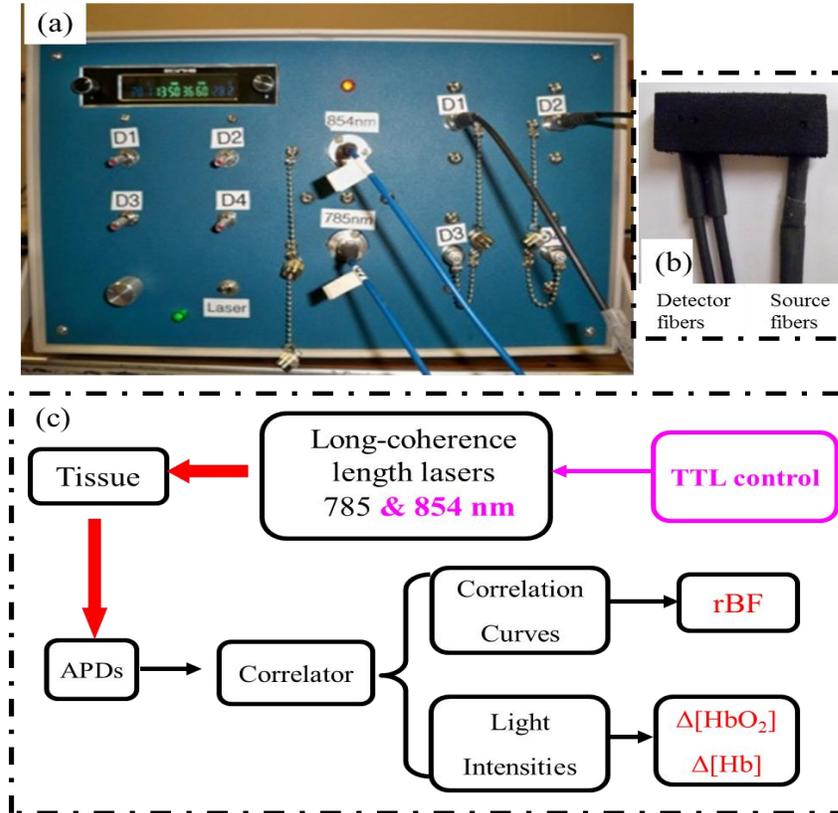
Figure 2.11 Photo (a), fiber-optic probe (b), and diagram (c) of a dual-wavelength DCS flow-oximeter.

Figure 2.11 shows a dual-wavelength 4-channel DCS flow-oximeter. Basically, we added another long-coherence CW laser at 854 nm to the previous single-wavelength (785 nm) DCS system. The two lasers were switched on and off alternately by TTL signals controlled automatically by DCS control panel. Similarly to CW NIRS, we can extract relative changes of tissue blood oxygenation (i.e., $\Delta[HbO_2]$, $\Delta[Hb]$, ΔTHC) via measuring light intensity changes at the two wavelengths (Chapter 2.2.1). The dual-wavelength DCS flow-oximeter used two source fibers (core diameter of each fiber = 200

μm, emission area $= 0.13$ mm^2) that were bundled tightly together (Figure 2.11c). To increase the SNR, signals from the 4 APDs were spatial averaged. The S-D separation was set to 2.5 cm for cerebral hemodynamic measurement. The probe pads used in DCS flowmeter (Figure 2.6a) and DCS flow-oximeter (Figure 2.11b) were very similar. DCS flow-oximeter shared the same source and detector fibers for both blood flow and oxygenation measurements, thus, it probed tissue hemodynamic parameters at an identical region of tissues.

Table 2.1 shows the comparison among hybrid NIRS/DCS devices and DCS flow-oximeter. Compared to the hybrid NIRS/DCS devices, DCS flow-oximeter measures the relative oxygenation changes, but is more portable, less expensive, and easier to operate. The upgraded hybrid NIRS/DCS employs a dual-mode autocorrelator which significantly improves the sampling rate, although it is bigger than the first generation hybrid instrument due to the increased number of DCS detectors.

Table 2.1 Comparison among hybrid NIRS/DCS devices and DCS flow-oximeter

	Hybrid NIRS/DCS device		DCS flow-oximeter
	Generation I	Upgraded	
Measurement Outcomes	rCBF, [Hb], [HbO$_2$], THC, StO$_2$	rCBF, [Hb], [HbO$_2$], THC, StO$_2$	rCBF, Δ[Hb], Δ[HbO$_2$], ΔTHC
Autocorrelator	Continuous mode	Continuous and Burst modes	Continuous mode
Dimensions	18"x24"x42"	32"x24"x42"	13"x21"x18"

Appendix I: Analytical Solutions of Photon Diffusion Equation in Different

Geometries

Analytical solutions in homogenous medium under infinite geometry.

Analytical solutions of Φ_{DC}, Φ_{AC}, and φ in Equations 2.14 and 2.15 exist for homogeneous medium under infinite geometries (Figure 2.4a)

$$\Phi_{DC}(\rho) = \frac{S_{DC}}{4\pi D} \frac{\exp\left[-\rho\left(\frac{v\mu_a}{D}\right)^{1/2}\right]}{\rho} \tag{2.33}$$

$$\Phi_{AC}(\rho) = \frac{S_{AC}}{4\pi D} \frac{\exp\left\{-\rho\left(\frac{v\mu_a}{2D}\right)^{1/2}\left[(1+x^2)^{1/2}+1\right]^{1/2}\right\}}{\rho} \tag{2.34}$$

$$\varphi(\rho) = \rho\left(\frac{v\mu_a}{2D}\right)^{1/2}\left[(1+x^2)^{1/2}-1\right]^{1/2} \tag{2.35}$$

where x is defined as $\omega/v\mu_a$. Then Equations 2.33 to 2.35 can be rewritten as Equations 2.16 to 2.18 shown in Chapter 2.2.3.

Analytical solutions in homogenous medium under semi-infinite geometry.

Under semi-infinite geometry (Figure 2.4b), the detected photon fluence rate can be calculated as the superposition of the infinite solution from the positive isotropic source (at z = z_0) and the negative imaging source (at z = -z_0 - 2z_b) [116, 117]. The solution for DC component (Φ_{DC}) is

$$\Phi_{DC}(\rho) = \frac{S_{DC}}{4\pi D}\left\{\frac{\exp\left[-r_1\left(\frac{v\mu_a}{D}\right)^{1/2}\right]}{r_1} - \frac{\exp\left[-r_2\left(\frac{v\mu_a}{D}\right)^{1/2}\right]}{r_2}\right\} \tag{2.36}$$

$$= \frac{2vS_{DC}}{(4\pi)^2 D} \frac{\exp\left[-\rho\left(\frac{v\mu_a}{D}\right)^{1/2}\right]}{\rho^3} \left[1 + \rho\left(\frac{v\mu_a}{D}\right)^{1/2}\right](z_b + z_0)$$

$$\times \left\{ z_b + \frac{3D}{v} \left\{ 1 - \frac{(z_b + z_0)^2 + 3z_b{}^2}{2\rho^2} \left[\frac{\rho^2 \frac{v\mu_a}{D}}{1 + \rho\left(\frac{v\mu_a}{D}\right)^{1/2}} + 3 \right] \right\} \right\}$$

Here, $r_1 = \sqrt{\rho^2 + z_0{}^2}$, $r_2 = \sqrt{\rho^2 + (z_0 + 2z_b)^2}$ (Figure 2.4b). Similarly, the solutions for Φ_{AC} and φ are:

$$\Phi_{AC}(\rho) = \frac{2vS_{AC}}{(4\pi)^2 D} \frac{\exp\left[-\rho\left(\frac{v\mu_a}{2D}\right)^{1/2} V^+\right]}{\rho^3}$$

$$\times \left[1 + \rho\left(\frac{2v\mu_a}{D}\right)^{1/2} V^+ + \rho^2 \frac{v\mu_a}{D}(1 + x^2)^{\frac{1}{2}}\right]^{\frac{1}{2}} \times (z_b + z_0)$$

$$\times \left\{ z_b + \frac{3D}{v} \times \left\{ 1 - \frac{(z_b + z_0)^2 + 3z_b{}^2}{2\rho^2} \right. \right.$$

$$\times \left[\frac{1 + \rho\left(\frac{v\mu_a}{2D}\right)^{\frac{1}{2}} V^+}{1 + \rho\left(\frac{2v\mu_a}{D}\right)^{1/2} V^+ + \rho^2 \frac{v\mu_a}{D}(1 + x^2)^{\frac{1}{2}}} \right.$$

$$\left. \left. \left. + \rho\left(\frac{v\mu_a}{2D}\right)^{1/2} V^+ + 3 \right] \right\} \right\}$$

(2.37)

$$\varphi(\rho) = \rho\left(\frac{v\mu_a}{2D}\right)^{1/2} V^- - arctan\left[\frac{\rho\left(\frac{v\mu_a}{2D}\right)^{1/2} V^-}{1 + \rho\left(\frac{v\mu_a}{2D}\right)^{1/2} V^+} \right] \qquad (2.38)$$

where $V^+ = \left[(1 + x^2)^{1/2} + 1\right]^{1/2}$, $V^- = \left[(1 + x^2)^{1/2} - 1\right]^{1/2}$.

To demonstrate the linear dependence of the logarithm of Φ_{DC} and Φ_{AC} and φ on ρ, we rewrite Equations 2.36 to 2.38 as:

$$\ln\left\{\frac{\rho^3\Phi_{DC}(\rho)}{\left[1+\rho\left(\frac{v\mu_a}{2D}\right)^{1/2}\right]F_{DC}(\rho,\mu_a,D,v,z_b,z_0)}\right\} \tag{2.39}$$

$$= -\rho\left(\frac{v\mu_a}{2D}\right)^{1/2} + G_{DC}(S_{DC},D,v,z_b,z_0)$$

$$\ln\left\{\frac{\rho^3\Phi_{AC}(\rho)}{\left[1+\rho\left(\frac{2v\mu_a}{D}\right)^{1/2}V^+ + \rho^2\frac{v\mu_a}{D}(1+x^2)^{\frac{1}{2}}\right]^{\frac{1}{2}}F_{AC}(\rho,\mu_a,D,\omega,v,z_b,z_0)}\right\} \tag{2.40}$$

$$= -\rho\left(\frac{v\mu_a}{2D}\right)^{1/2}V^+ + G_{AC}(S_{AC},D,v,z_b,z_0)$$

$$\varphi(\rho) + arctan[F_\varphi(\rho,\mu_a,D,\omega,v)] = \rho\left(\frac{v\mu_a}{2D}\right)^{1/2}V^- \tag{2.41}$$

where F_{DC}, F_{AC}, $F\varphi$, G_{DC}, and G_{AC} are defined by expanding the terms in Equations 2.36 to 2.38. The slopes of the straight lines (SL_{DC}, SL_{AC}, and SL_φ) can be fitted from the measured values in the LHS of Equations 2.39 to 2.41 at different ρ, respectively. Note that the slopes under semi-infinite geometry are defined by the same equations under infinite geometry (Equations 2.19 to 2.21). Thus using Equations 2.22 and 2.23, one can extract μ_a and μ_s' from the fitted slopes under semi-infinite geometry.

Overall, we extract μ_a and μ_s' from Equations 2.40, 2.41, 2.22, and 2.23, iteratively. More specifically, we ignore the terms that have μ_a and μ_s' (i.e., assuming $\mu_a = 0$ and $\mu_s' = 0$) on the LFH of the Equations 2.39 to 2.41 and obtain the slopes of $SL_{DC}(0)$, $SL_{AC}(0)$, and $SL_\varphi(0)$, and from which we determine $\mu_a(0)$ and $\mu_s'(0)$ using Equations 2.22 and 2.23, where 0 indicates the initial guess. We then use these values to

obtain $SL_{DC}(1)$, $SL_{AC}(1)$, and $SL_{\varphi}(1)$, $\mu_a(1)$, and $\mu_s{}'(1)$, where "1" represents the first iteration. We continue applying this procedure recursively until $\mu_a(i)$ and $\mu_s{}'(i)$ reproduce themselves within a difference of less than 0.1%. Here i represents the number of iterations. The convergence is usually reached after a few iterations.

Appendix II: Derivation of Correlation Diffusion Equation
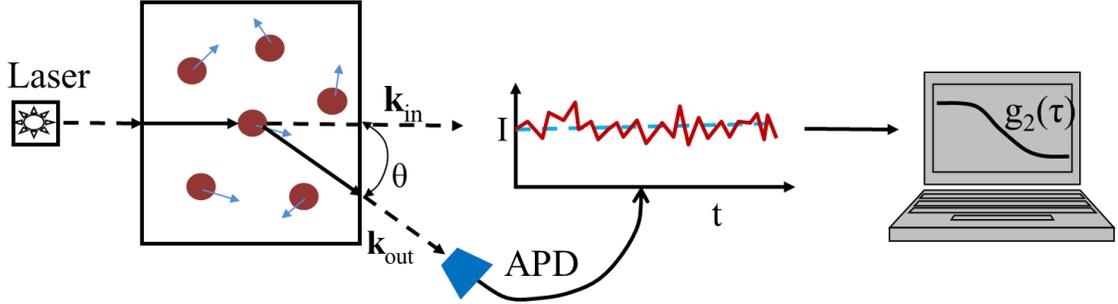
Figure 2.12 Single dynamic light scattering experiment.

    Single scattering events. In a single scattering DLS experiment, photons are usually scattered once (or not at all) before they leave the sample (Figure 2.12). A point-like photon detector is placed at an angle $\theta = k_{out} - k_{in}$ relative to the propagation direction of input beam. If the scatterers are moving, then the total electric field (E(t)) will vary in time and light intensity ($I = \langle E(t) \cdot E^*(t) \rangle$) fluctuations are observed. Thus the fluctuations of the electric field/light intensity are linked to dynamic properties of the medium, i.e., the motion of the particles/scatterers. The normalized temporal autocorrelation function of the scattered electric field ($g_1(\tau)$) for CW light source is:

$$g_1(\tau) = \frac{\langle E(t) \cdot E^*(t+\tau) \rangle}{\langle E(t) \cdot E^*(t) \rangle} = e^{-\frac{1}{6} q^2 \langle \Delta r^2(\tau) \rangle} \tag{2.42}$$

    Here, τ is the autocorrelation delay time, $q^2 = 2k_0^2(1 - cos\theta)$ is the square of the scattering wavevector, $k_0 = \frac{2\pi n}{\lambda}$ is the wavevector magnitude of the incident light field, n is the index of refraction of the medium, λ is the wavelength of the light field, and $\langle \Delta r^2(\tau) \rangle$ is the mean square displacement of the scatterers in the medium, which directly characterizes the particle movement.

Multiple scattering events. In case of photon transportation in biological tissue, multiple scattering effects are usually involved. Each scattering event from a moving scatterer contributes to the accumulation of the phase shift mentioned in Chapter 2.2.3 and also the decay of the electric field correlation function. If we assume the electric fields from individual photon path (Figure 2.1) are uncorrelated, the total temporal field autocorrelation function can be expressed as the weighted sum of the field autocorrelation function from each photon path. Furthermore, if we assume a homogeneous medium, and further assume that each scattering event is independent and that scatterers' displacements are uncorrelated, the field autocorrelation function from a single path can be written as:

$$g_1(\tau)_{onepath} = e^{-\frac{1}{3}k_0^2 Y \langle \Delta r^2(\tau) \rangle}$$ (2.43)

where $Y = N(1 - \langle cos\theta \rangle_N)$, and $\langle cos\theta \rangle_N$ is the average value of cosine over all the N scattering events along the path. When N is large, the average value approaches the ensemble average, $\langle cos\theta \rangle_N$, which is usually denoted by the so-called anisotropy factor (g) of the medium. The reduced photon scattering length or random-walk step length is $l_s^* = 1/\mu_s' = 1/(\mu_s \cdot (1 - \langle cos\theta \rangle_N))$, where μ_s is the scattering coefficient of the medium [118]. Let S represents the total pathlength associated with a particular photon path. Then the number of scattering events associated with this same path is N = s/($l_s^* \cdot (1 - \langle cos\theta \rangle_N)$), and Y = s/$l_s^*$ equals the total number of photon *random-walk* steps associated with the photon path.

The final detected electric field autocorrelation function includes the contributions of all photon paths. If we use P(Y) to represent the probability distribution for photon paths with a number of random walk steps, Y, then the total electric field autocorrelation

function can be computed by incoherently integrating the contributions from each photon path [96, 119], that is.:

$$g_1(\tau) = \int_0^\infty P(Y)\, e^{-\frac{1}{3}k_0^2 Y \langle \Delta r^2(\tau) \rangle}\, dY \tag{2.44}$$

In a highly scattering medium, Equation 2.44 can be equivalently expressed as an integral over all possible pathlengths using the pathlength distribution [96, 120, 121], P(s), i.e.,

$$g_1(\tau) = \int_0^\infty P(s)\, e^{-\frac{s}{3l_s^*}k_0^2 \langle \Delta r^2(\tau) \rangle}\, ds \tag{2.45}$$

Equation 2.45 is the primary result from diffusing-wave spectroscopy (DWS) for a homogeneous turbid scattering medium composed of moving particle-like scatterers. The DWS correlation function is typically measured at some point inside the sample or on its surface, and P(s) depends implicitly on both measurement location and source position. The distribution of P(Y) can be readily obtained from Monte Carlo simulation [122]. Alternatively, derivation of P(s) can be obtained experimentally from the normalized photo fluence rate (Φ) from a TD NIRS measurement [123-126]. For example, the solution to a pulsed CW light source with $S(r, t) = S_0 \delta(r, t = s/v = 0)$ is:

$$P(r, s) = \frac{\Phi(r, t = s/v)}{\int_0^\infty \Phi(r, t)dt} = \frac{\Phi(r, t = s/v)}{I(r)} \tag{2.46}$$

where r is the location inside or on the surface of the turbid medium, S_0 is the power of the CW source.

Correlation diffusion equation. Unnormalized electric filed temporal autocorrelation $G_1(r,\tau) = g_1(r,\tau) \cdot I(r)$ is linked with the $\Phi(r, s = vt)$ using Equations 2.45 and 2.46:

$$G_1(r,\tau) = I(r) \int_0^\infty P(r,s) e^{-\frac{s}{3l_s^*} k_0^2 \langle \Delta r^2(\tau) \rangle} ds = \int_0^\infty \Phi(r,s) e^{-\frac{s}{3l_s^*} k_0^2 \langle \Delta r^2(\tau) \rangle} ds \quad (2.47)$$

Following Ref [93], we can do a simple replacement of variables (s = vt), multiply e^{-ps}, where $p = -\frac{1}{3l_s^*} k_0^2 \langle \Delta r^2(\tau) \rangle$ to both sides of Equation 2.9 and integrate s from 0 to ∞,

$$D\nabla^2 \int_0^\infty \Phi(r,s) e^{-ps} \, ds - v\mu_a \int_0^\infty \Phi(r,s) e^{-ps} \, ds$$
$$+ v \int_0^\infty S_0 \delta(r, s = vt) e^{-ps} \, ds = v \int_0^\infty \frac{\partial \Phi(r,s)}{\partial s} e^{-ps} \, ds \quad (2.48)$$

The first and second terms on the LHS of Equation 2.48 is simplified as $D\nabla^2 G_1(r,\tau)$ and $v\mu_a G_1(r,\tau)$. The third term on LHS of Equations 2.48 can be calculated as $vS_0\delta(r)$ by integrating $S_0\delta(r, s = vt)e^{-ps}$ over s. Thus the RHS yields:

$$v \int_0^\infty \frac{\partial \Phi(r,s)}{\partial s} e^{-ps} \, ds = v \left[\Phi(r,s) e^{-ps} \big|_0^\infty + p \int_0^\infty \Phi(r,s) e^{-ps} \, ds \right]$$
$$= vp G_1(r,\tau) = \frac{1}{3} v\mu_s' k_0^2 \langle \Delta r^2(\tau) \rangle G_1(r,\tau) \quad (2.49)$$

We combine the results above and simplify Equations 2.48 as:

$$D\nabla^2 G_1(r,\tau) - v\mu_a G_1(r,\tau) + vS_0\delta(r) = \frac{1}{3} v\mu_s' k_0^2 \langle \Delta r^2(\tau) \rangle G_1(r,\tau) \quad (2.50)$$

By rearranging the above equation and dividing both sides by $D \approx v/3\mu_s'$, we get the *correlation diffusion equation* in homogenous medium for CW light source:

$$\left[\nabla^2 - \left(3\mu_a\mu_s' + {\mu_s'}^2 k_0^2 \langle \Delta r^2(\tau) \rangle\right)\right]G_1(r,\tau) = -\frac{vS_0\delta(r)}{D} \qquad (2.51)$$

CHAPTER 3 DIFFUSE OPTICAL EVALUATION OF CBF AND CA IN PATIENTS WITH OBSTRUCTIVE SLEEP APNEA (OSA)

3.1 Background

OSA is characterized by repetitive episodes of upper airway obstruction during sleep that disturbs sleep architecture and induces intermittent hypoxia, and it affects 15 million adult Americans [9, 10]. OSA episodes are associated with surges in blood pressure, hypercapnia, and fluctuations in CBFV/CBF. The OSA episode and breath holding maneuver perturb the cerebral circulatory control because of the hypoxia [127-130]. Specifically, systemic blood pressure and CBFV increase progressively during the apnea followed by an abrupt decrease in both during the post apnea hyperventilation period. These perturbations can adversely affect CA [13], leading to cerebral impairment or brain dysfunction.

Several studies have quantified dynamic CA in patients with OSA via measuring CBFV by TCD and MAP by finger plethysmograph [13, 131]. Nasr et al have found that the correlation coefficients between the MAP and CBFV in middle MCA were significantly higher in patients with OSA (n = 11) than those in healthy controls (n = 9) [131]. The higher correlation between the MAP and CBFV found in patients with OSA, indicating a worse CA. Urbano et al quantified dynamic CA in TD using orthostatic hypotension as an autoregulatory stimulus [13]. A sudden standing after 2-minute squatting was adopted to induce a decrease in MAP. Compared to control subjects (n = 26), significantly lower recovery rate of cerebral vascular conductance (i.e., slope of CBFV/MAP) were found in patients with OSA (n = 22), indicating an impaired CA [13].

Structural (e.g., the gray and white matter loss [132]) and functional (e.g., attention deficit, memory loss, impaired executive functions [12]) damages found in patients with OSA are usually associated with abnormal microvasculature [74]. However, due to the lack of techniques for CBF measurements, no one has ever quantified dynamic CA in microvasculature in this patient population. DCS offers noninvasive and inexpensive measurement of CBF, thus allowing for the evaluation of microvascular CA in patients with OSA.

Several physiological manipulations have been used as the autoregulatory stimuli in testing dynamic CA, including bilateral thigh pressure cuff deflation [23], squat-to-standing [13], head-up tilt (HUT) [133], and voluntarily breath holding [134]. Cuff inflation/deflation, squat-to-standing and HUT protocols create a MAP drop due to the reduction of cardiac outputs. However, the position changes during squat-to-standing and HUT may result in motion artifacts in MAP and optical measurements. The MAP measurement by the finger plethysmograph is sensitive to the relative height difference between the subject's heart and finger sensor. The voluntarily breath holding is a subjective test. Therefore, the bilateral thigh pressure cuff inflation/deflation protocol was selected in this study as an autoregulatory stimulus for dynamic CA test.

3.2 Methods

3.2.1 Subjects

Eleven (11) healthy controls and 13 patients with OSA participated in this study (Table 3.1) with signed consent forms approved by the University of Kentucky

Institutional Review Board. The apnea-hypopnea index (AHI), defined as apnea and hypopnea events occurred per hour during sleep, was used to classify the severity of OSA (i.e., healthy: AHI < 5, mild: 5 < AHI < 15, moderate: 15< AHI < 30, severe: AHI > 30) [135].

Table 3.1 Subject characteristics

	Total Number	Female	Male	Age (year)	Body Mass Index (BMI) (kg/m^2)	Apnea-Hypopnea Index (AHI)
Healthy Controls	11	7	4	42 ± 16 (23~68)	24 ± 4 (18~32)	< 5
OSA Patients	13	7	6	53 ± 13 (35~69)	39 ± 11 (22~58)	53 ± 43 (10~122)

3.2.2 Experimental Protocol

The subject laid supine on a table and his/her MAP was continuously monitored by a finger plethysmograph (Figure 3.1). The finger sensor for MAP measurements was placed on the subject's middle finger of left hand with his/her left arm fully extended at the same level of the heart. A DCS flowmeter was used to continuously monitoring CBF. A fiber-optic probe containing a multimode source fiber (x 1) and a single mode detector fiber (x 1) was taped on the middle of forehead for CBF measurement. An elastic bandage was used to wrap around the forehead to secure the probe and reduce the influence of room light. The measured light intensity was limited by the use of single-mode fiber for DCS detection, thus restricting the use of large S-D separation. The separation was set at 2.5 cm which allowed for the detection of cerebral hemodynamics in adult prefrontal cortex [25, 38, 61, 63, 64, 68, 108]. The sampling rate for CBF and

MAP was 0.64 Hz (1/1.56 s). After baseline measurements for 5 minutes, both thighs of the subject were occluded by two cuff occlusion machines (Aspen ATS1000, Zimmer Inc., IN, USA) at a pressure of 230 mm Hg for 5 minutes. The pressures on both thighs were then rapidly and concurrently released.
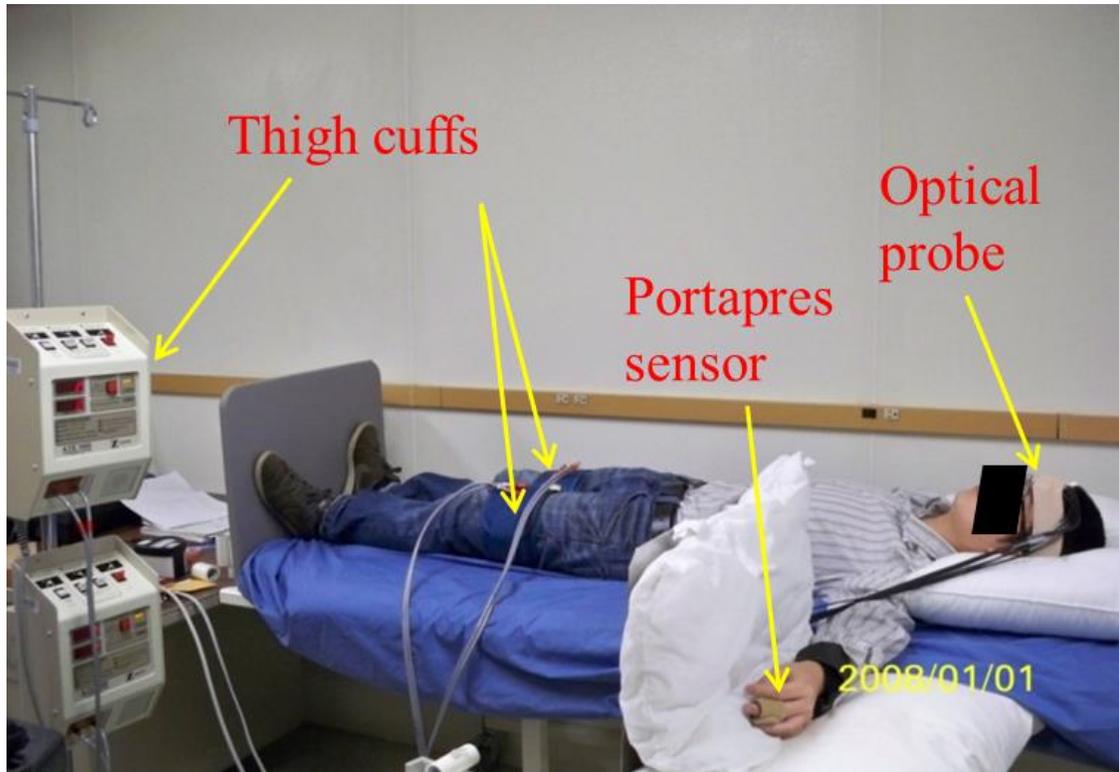
Figure 3.1 Experimental setup for assessing CBF and dynamic CA in patients with OSA.

3.2.3 Data Analysis.

Dynamic changes in MAP and rCBF after cuff deflation were defined as ΔMAP (mm Hg) and ΔrCBF (%), which were calculated as ΔMAP = MAP_{mean} - MAP_{min} and ΔrCBF = $rCBF_{mean}$ - $rCBF_{min}$. Here MAP_{mean} and $rCBF_{mean}$ were the averaged data from the 20-second before cuff deflation, and MAP_{min} and $rCBF_{min}$ were the minimum values

within 30 seconds after cuff deflation in MAP and rCBF, respectively (Figure 3.3). The negative ΔMAP or ΔrCBF indicated a decrease in MAP and rCBF. CA index (CAI) was calculated by ΔrCBF/ΔMAP (% / mm Hg), indicating the change of cerebral vascular conductance. Two-tailed Student t-test was used for statistical analysis. A p-value less than 0.05 indicated a significant difference.

3.3 Results

3.3.1 Individual Results
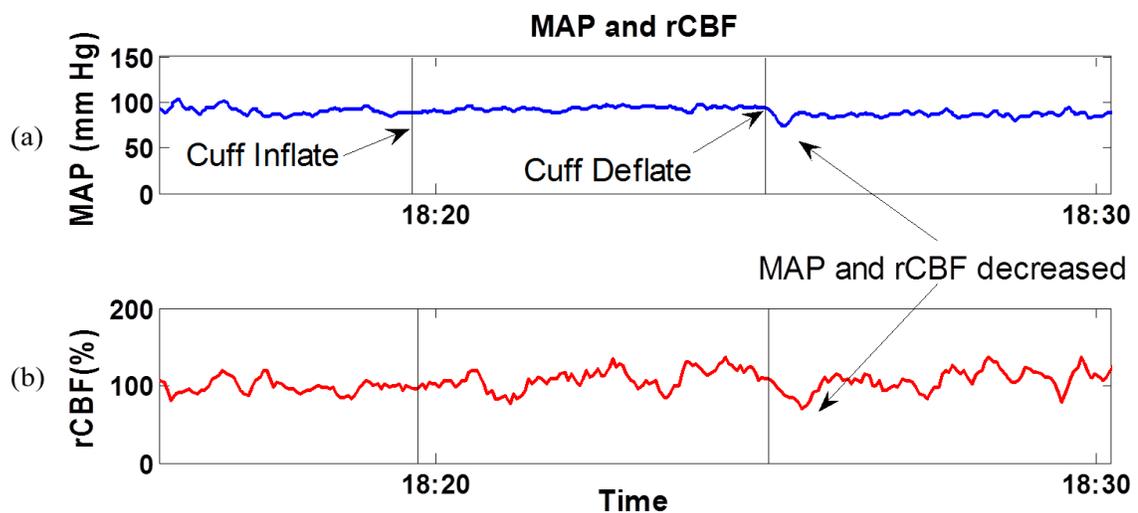
Figure 3.2 Typical MAP (a) and rCBF (b) results in response to cuff deflation in one healthy subject.

Figure 3.2 shows typical time course responses of MAP and rCBF before, during and after cuff deflation measured in one healthy subject. After cuff deflation, MAP and rCBF decreased immediately and then recovered in a short time. Figure 3.3 shows typical results after cuff deflation in a patient with OSA (a) and a healthy control (b). Smaller

ΔMAP and ΔrCBF were found in the patient with OSA (ΔMAP = -8.8 mm Hg and ΔrCBF = -15%) than those in the control subject (ΔMAP = -17 mm Hg and ΔrCBF = -32%).
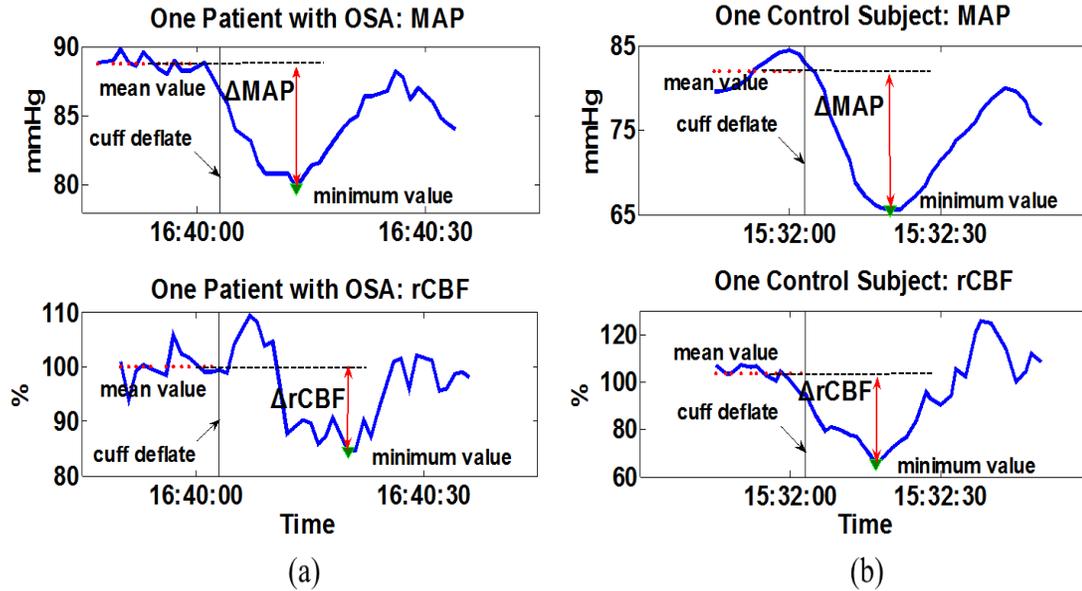
Figure 3.3 Typical ΔMAP and ΔrCBF responses in a patient with OSA (a) and a control subject (b).
The vertical lines indicate the beginning of cuff deflation. The horizontal dashed lines represent the mean values of rCBF/MAP before cuff deflation. The green triangles show the minimum values of rCBF/MAP within 30 seconds after cuff deflation. The red lines with arrows show relative changes of rCBF/MAP after cuff deflation.

3.3.2 Average Results

On average (Figure 3.4), significantly smaller (p = 0.014) ΔrCBF was found in the OSA group (-17 ± 9%) compared to the control group (-26 ± 8%). The OSA group also had a significantly lower (p = 0.005) ΔMAP (-8.6 ± 4.5 mmHg) compared to the control group (-15.0 ± 5.5 mmHg). However, there was no significant difference (p =

0.967) in CA index (CAI) between the OSA (0.023 ± 0.014 %/mm Hg) and control (0.019 ± 0.008 %/mm Hg) groups.
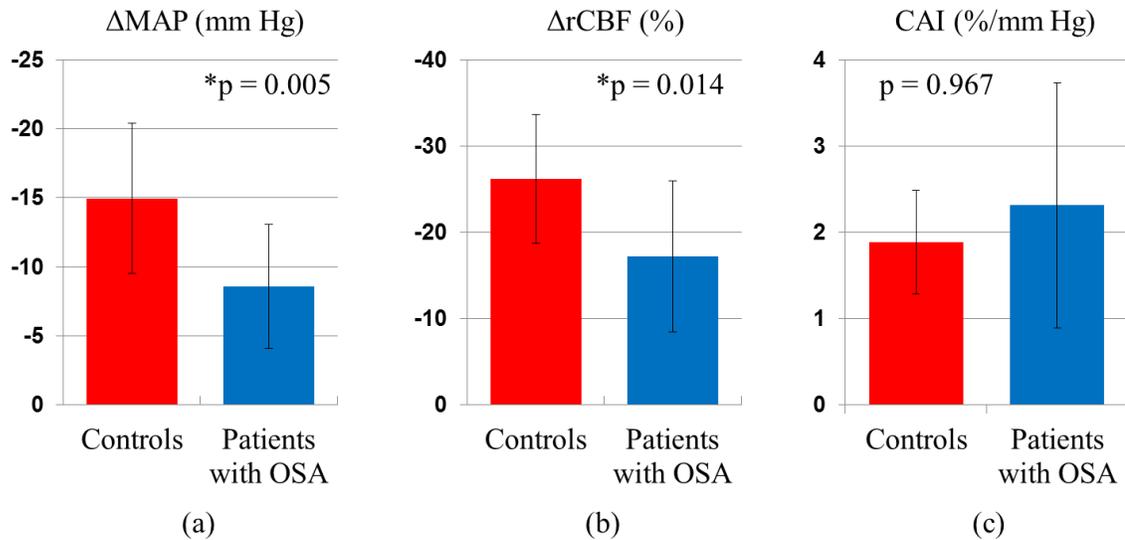
Figure 3.4 Average results of ΔMAP (a), ΔrCBF (b), and CAI (c) in the control and OSA groups.

3.4 Discussion and Conclusions

Previous studies have shown that quantifying recovery rate of cerebral vascular conductance in MCA can be used for the evaluation of TD dynamic CA in large vessels [13]. However, the CBFV in large arteries does not always reflect the CBF in brain microvasculature [38]. In the present study, we have evaluated TD dynamic CA in frontal cortex, *for the first time*, using the rCBF and MAP measured by the novel DCS and a commercial finger plethysmography during bilateral thigh pressure cuff deflation.

Compared to healthy subjects, the smaller changes in MAP after cuff deflation in patients with OSA might be due to the less vasodilation in the lower extremities. The impaired endothelial function in patients with OSA [136] may have impaired the

vasodilation ability which is related to nitric oxide mechanisms [137]. Moreover, high sympathetic nervous activity has been found in patients with OSA [138], which can cause high resting constriction tone of blood vessels. The less decrease in MAP after cuff deflation may lead to the small changes in rCBF in the patient group. More investigations are needed to confirm these hypotheses.

Surprisingly, we couldn't find significant difference in CAI between the control and OSA groups during cuff deflation. The relatively small changes in MAP (< 15 mm Hg) created by the cuff deflation were much less than the CA range (60 ~ 150 mm Hg) [139], which might be the major reason contributing to this surprise. In other words, both patients and healthy controls might be able to maintain a stable CBF when there were relatively small disturbances in MAP. However, the small number of subjects with large inter-subject hemodynamic variations may also play a role for this surprise. Furthermore, the relatively low sampling rate (0.64 Hz) of DCS measurements working under the continuous mode might bring errors in quantifying rapid changes in rCBF and MAP during cuff deflation.

More subjects are needed to increase the statistical power of our study. A DCS flowmeter with higher sampling rate (e.g., working in the burst mode) is needed to detect rapid dynamic changes in CBF in response to the autoregulatory stimulus. Other physiological manipulations should be explored to create larger MAP changes with less inter-subject variations for testing potential CA impairments in patients with OSA. Nevertheless, DCS flowmeter shows potential for detecting CBF directly and evaluating dynamic CA in cerebral microvasculature.

CHAPTER 4 DIFFUSE OPTICAL EVALUATION OF SPONTAENOUS LOW FREQUENCY OSCILLATIONS (LFOS) IN CEREBRAL HEMODYNAMICS

4.1 Background

As mentioned early (Chapter 1.2), dynamic CA can be evaluated in time-domain (TD) and frequency-domain (FD). TD methods (see the example in Chapter 3) quantify dynamic CA from the rapid changes of MAP and CBF/CBFV in the short period (e.g., ~30 seconds during bilateral thigh pressure cuff deflation, see Chapter 3) during autoregulatory stimulus, which greatly relies on the SNR of the detected signals in the short period with limited data points. By contrast, FD methods (e.g., quantification of the phase shifts in LFOs between the MAP and cerebral hemodynamics) extract dynamic CA from the relatively stable data of MAP and cerebral hemodynamics in a relatively long period (e.g., 10 minutes). It is expected that more data points with smaller variations should provide better SNRs. Furthermore, LFO phase shift depends mainly on the relation of oscillation frequencies of MAP and cerebral hemodynamics rather than on the detected signal intensities, which should provide more robust results. We thus started testing dynamic CA in FD.

In 1876, Mayer first found the spontaneous LFOs around 0.1 Hz in blood pressure which were later named as "Mayer waves" [140]. The LFOs in blood pressure are believed to be originated from residual oscillations of baroreflex at ~0.1 Hz [141]. With the development of noninvasive techniques for cerebral hemodynamic measurements, people have also detected LFOs in CBFV of MCA by TCD [142], in cerebral blood oxygenation quantified by NIRS [143], and in BOLD signal measured by fMRI [144].

The CBF control mechanism underlying blood pressure oscillations may be extracted from the relationship between LFOs of ABP and cerebral hemodynamics, therefore holding potential for evaluating dynamic CA in FD [7, 18] and neurocognitive function [29]. For example, the decrease/increase in phase lead/lag of LFOs between CBFV/oxygenation and ABP in patients with carotid artery stenosis had been found by Reinhard et al. [7]. Wang et al. also showed that cerebral functional connections extracted from LFO signals of BOLD MRI were different in patients with impaired neurocognitive function (i.e., Alzheimer disease) compared to healthy subjects [145].

It is relatively easy to measure LFOs in resting state, but previous results showed weak oscillations at rest [142, 146, 147]. Physiological manipulations have been applied in subjects in order to increase the SNRs of LFOs, such as HUT [142, 146, 147] and paced breathing at 0.1 Hz [7, 26, 148]. HUT increases sympathetic nervous activity, thus elevating LFOs in cerebral hemodynamics and MAP [142]. During paced breathing, a superimposed strong 0.1 Hz oscillation enhances the LFOs of both MAP and cerebral hemodynamics. However, complex chemical and neural reactions disturbing CA may be created from the change of respiratory rate during paced breathing.

The goal of this study was to find the most sensitive cerebral hemodynamic variables and the most robust protocols for evaluating dynamic CA. For this purpose, I upgraded a hybrid NIRS/DCS instrument to achieve a higher sampling rate and a better SNR (Chapter 2.4). With these improvements we successfully detected LFO signals in cerebral hemodynamics which cannot be extracted by the previous generation I hybrid device (Figure 2.7). Using this upgraded instrument, CBF, [HbO$_2$], [Hb] and THC were continuously monitored at rest, during 70 $^{\circ}$ HUT, and during paced breathing at 0.1 Hz in

15 healthy subjects. Power spectral analysis was used to extract LFOs from the measured variables [24], and transfer function analysis was used to calculate the corresponding phase shifts and coherences of LFOs between the MAP and each of the measured cerebral hemodynamic parameters [7, 142, 148]. Reliable LFOs between the paired signals were selected based on the levels of coherence. The success rates of capturing LFOs of hemodynamic variables under the three physiological conditions were finally compared to determine the best hemodynamic parameter among the measured variables and optimal physiological condition in detecting cerebral hemodynamic LFOs.

4.2 Methods

4.2.1 Subjects

Fifteen young healthy adults participated in this study with signed consent forms approved by the University of Kentucky Institutional Review Board. The average age of subjects was 27 ±5 years.

4.2.2 Experimental Protocols

Cerebral hemodynamic parameters and MAP were simultaneously measured by the upgraded hybrid NIRS/DCS instrument and a finger plethysmograph under three conditions: at rest, during HUT and during paced breathing at 0.1 Hz (Figure 4.2). The sampling rate of measurements for all physiological parameters was ~2 Hz. The subject lay supine on a tilting table (Hausmann Inc., USA) and then was immobilized by two Velcro straps placed over the chest and thighs. A padded cushion was used to place the

left forearm at the heart level. The plethysmograph sensor was put on the middle finger of left hand and monitored the beat-to-beat MAP (mm Hg) continuously. Two fiber-optic probes were taped on the left and right sides of the forehead respectively at a position about 2 cm from the midline and 1 cm above the eyebrows (Figure 4.1a). A self-adhesive elastic band was then stretched around the forehead to fix both probes tightly and minimize the influence of room light on optical measurements. All data were continuously recorded throughout the experimental protocols which included 10 min baseline at rest, 10 min HUT at 70 °, 10 min break after HUT back to 0 °, and 10 min paced breathing at 0.1 Hz (Figure 4.2). During HUT test, the left forearm was held by an adjustable medical sling to keep the pressure sensor at the heart level. Before the test, each subject was trained to breathe regularly at 0.1 Hz following audio cues made by Microsoft PowerPoint. During experiments, room light was turned off to reduce the influence of ambient light.
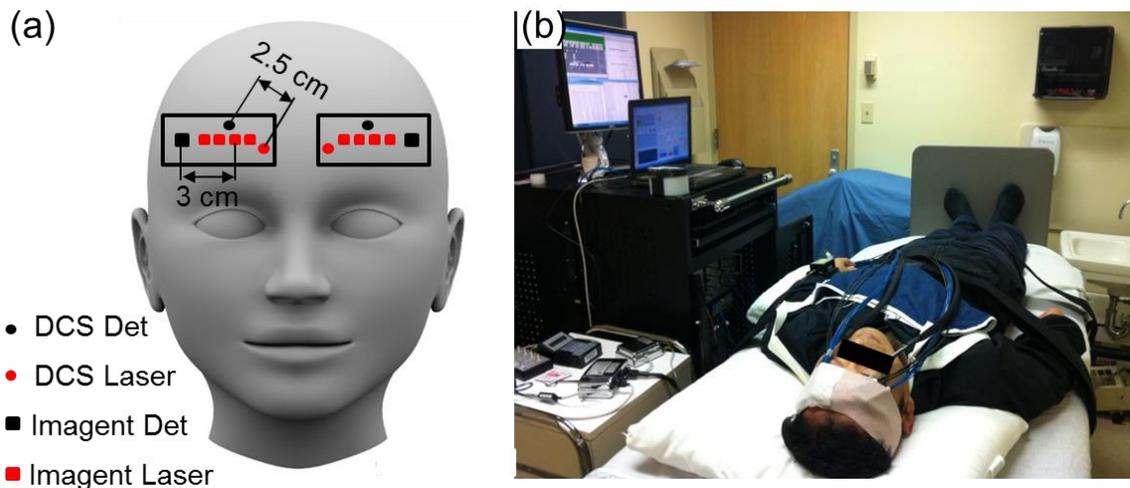
Figure 4.1 Placement of two hybrid fiber-optic probes on the forehead (a), and experimental setup (b) for noninvasive measurements of LFOs in cerebral hemodynamics.
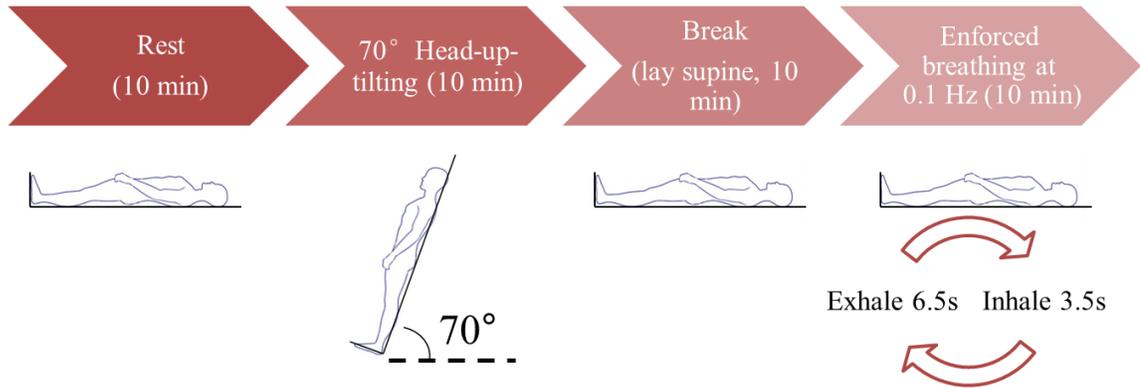
Figure 4.2 Experimental protocols.

4.2.3 Data Analysis

Although the Imagent could measure the absolute values of tissue blood oxygenation (i.e., $[HbO_2]$, $[Hb]$, THC, StO_2) [76, 81], the measured time courses of absolute values were found too noisy to extract reliable LFOs. This was mainly due to the unstable phase slopes over time. Thus, the phase data were ignored from our analysis. We used the measured amplitudes at the two wavelengths from a single S-D pair (S-D separation = 3 cm) to calculate the relative changes of cerebral blood oxygenation (i.e., $\Delta[HbO_2]$ and $\Delta[Hb]$) based on MBLL [50, 64] (Chapter 2.2.1). The molar extinction coefficients were found from the literature [87]. DPF values were calculated from measured absolute baseline values of μ_a and μ_s' [81, 149], and were assumed constant over time. The ΔTHC was calculated by sum of $\Delta[HbO_2]$ and $\Delta[Hb]$.

According to the methods described in previous studies [7, 142, 148], power spectral densities (PSDs) of MAP and cerebral hemodynamic parameters (i.e., rCBF, $\Delta[HbO_2]$, $\Delta[Hb]$, and ΔTHC) under the three physiological conditions (i.e., at rest, during HUT, and during paced breathing at 0.1 Hz) were used to determine the LFO intensities

in those physiological variables. The PSD was calculated using Welch's method (Figure 4.3) [24]. Briefly, the linear trend of ~10 min time-course dataset (~1200 data points at a sampling rate f_s = ~2 Hz) for each variable under a specific physiological condition were removed firstly. Note that we excluded noisy data during the short periods of physiological state transition (i.e., table tilting up/down). The detrended data were then divided into 8 segments [7]. The two adjacent segments had 50% overlap [24]. Therefore each segment had a length of ~267 (1200*2/9) data points. A Hanning window was applied to each segment to decrease the effect of spectral leakage. The FD spectrum of each segment was calculated by fast Fourier transform: FFT(x_{seg}). Here x_{seg} indicated time-course data in one segment. One smooth spectrum F_x(f) was yielded by averaging the 8 spectra, where f was the frequency. The frequency resolution of the averaged spectrum was ~0.0075 Hz (f_s/267). LFO intensity was calculated as PSD_{xx}(f) = F_x*(f) F_x(f)/f_s. Here f was in the low frequency range of 0.05 to 0.15 Hz and F_x*(f) was the complex conjugate of F_x(f).

$$F_x(f) = \frac{1}{8} \sum FFT(x_{seg}) \qquad F_y(f) = \frac{1}{8} \sum FFT(y_{seg})$$

$$PSD_{xx}(f) = F_x^*(f)F_x(f)/2Hz \quad CSD_{xy}(f) = F_x^*(f)F_y(f)/2Hz \quad PSD_{yy}(f) = F_y^*(f)F_y(f)/2Hz$$

$$HF(f) = CSD_{xy}(f)/PSD_{xx}(f) \qquad Coh(f) = |CSD_{xy}(f)|^2/[PSD_{xx}(f)PSD_{yy}(f)]$$

$$\Phi(f) = \arctan [HF_I(f)/HF_R(f)] \qquad Coh(f) = |CSD_{xy}(f)|^2/[PSD_{xx}(f)PSD_{yy}(f)]$$

Find the frequency f_0 (0.05<f_0<0.15 Hz) at which the $Coh(f_0)$ exhibits the largest value

Unsuccessful measurement ← No — Is $Coh(f_0)$>0.4 ?

Yes ↓

Successful measurement
LFO frequency = f_0
phase shift = $\Phi (f_0)$
Leading Time = $\Phi (f_0)/360°/f_0$

Figure 4.3 Data analysis procedures to identify successful LFO measurements and extract phase shifts and leading times in cerebral hemodynamic parameters.

CA has been hypothesized as a linear system with input of MAP and output of cerebral hemodynamics [7, 142, 148]. The property of this linear system (e.g., phase shifts between the inputs and outputs) quantified by transfer function analysis indicates the characteristics of CA. To perform transfer function analysis, cross spectral densities (CSDs) between MAP and each of the cerebral hemodynamic parameters were needed. Similar to the calculation of PSD, CSD were quantified by $CSD_{xy}(f) = F_x^*(f) F_y(f)/f_s$ (Figure 4.3). Here x and y indicated MAP and one of the cerebral hemodynamic parameters, respectively. The transfer function was then determined: $H(f) = CSD_{xy}(f)/PSD_{xx}(f)$. Here $PSD_{xx}(f)$ represented the PSD of MAP. Using the equations: $\Phi(f)$

= arctan[$H_I(f)/H_R(f)$] and Coh(f) = $|CSD_{xy}(f)|^2/[PSD_{xx}(f)\ PSD_{yy}(f)]$, one could assess the phase shift and coherence between the paired signals. Here $H_I(f)$ and $H_R(f)$ were the imaginary and real parts of H(f), respectively.

A high level of coherence represents a reliable and constant phase relationship between paired parameters. The success of LFO measurements and the relative phase shift thus can be determined by Coh(f). Based on previous studies [8, 150], if the largest Coh(f_0) found in the low frequency range ($0.05 < f_0 < 0.15$ Hz) was higher than 0.4 the LFO measurement was judged to be successful. The reliable LFO frequency and phase shift respectively were then determined by f_0 and $\Phi(f_0)$. The positive/negative $\Phi(f_0)$ represented that the corresponding LFO of a hemodynamic parameter preceded/followed the LFO of MAP in time. LFO leading time ($T_{leading}$) could be converted from $\Phi(f_0)$ by the equation: $T_{leading} = \Phi(f_0)/360\ \%f_0$. The best parameter(s)/protocols(s) for future LFO study were determined by comparing the success rates of capturing reliable LFOs and phase shifts for all hemodynamic parameters under the three conditions in two hemispheres. Figure 4.3 shows a flowchart for better understanding the data analysis procedures described above.

4.3 Results

4.3.1 Individual Results
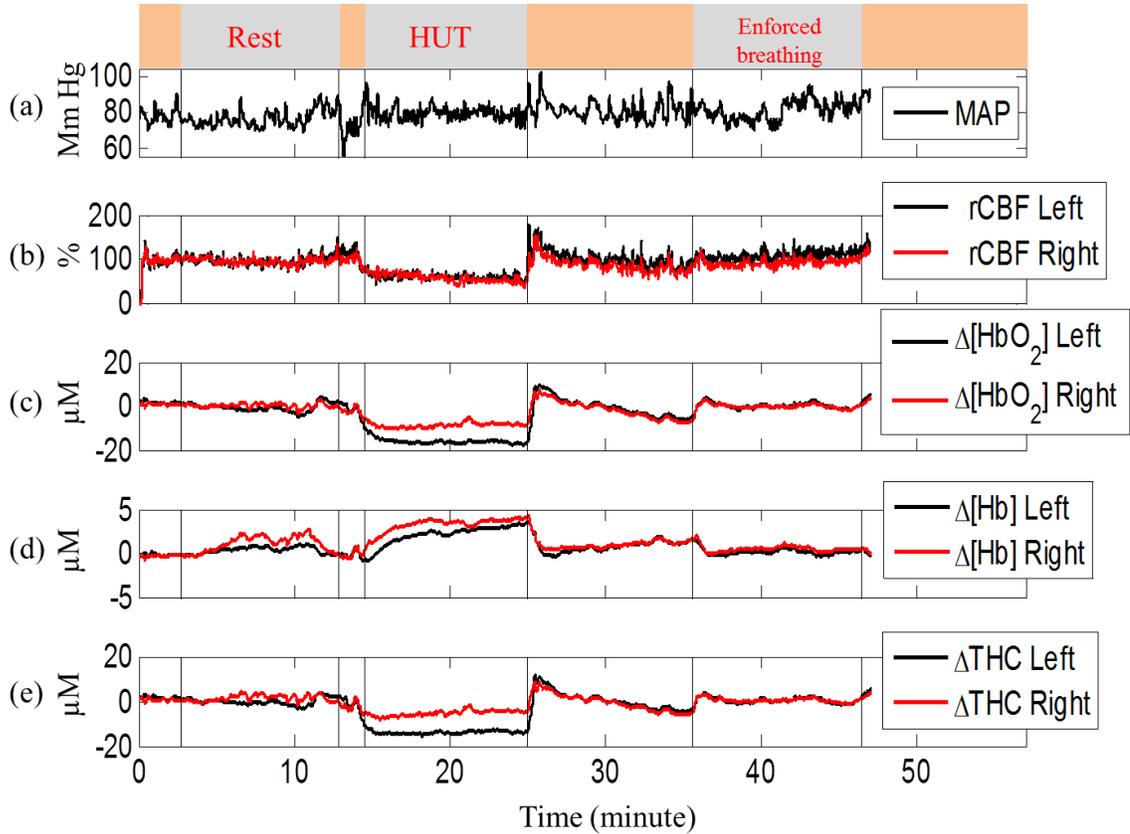
Figure 4.4 Typical time course responses of MAP and cerebral hemodynamics in a reprehensive subject.
(a) MAP measured by the finger plethysmograph, (b) rCBF, and (c) to (e): cerebral oxygenation changes measured in the left and right hemispheres. The vertical lines indicate the beginning and end of different physiological conditions.

Typical time-course data of MAP and cerebral hemodynamics throughout the entire protocol measured from one subject's left and right hemispheres are shown in Figure 4.4. Over the entire experiment, similar average levels of MAP (~80 mm Hg) were observed at all physiological conditions (Figure 4.4a). Due to cerebral heterogeneous responses, slight differences existed in cerebral hemodynamics between

the left and right hemispheres (especially during HUT). However, bilateral response trends were same. Inverse responses were found in $\Delta[HbO_2]$ and $\Delta[Hb]$, and $\Delta[HbO_2]$ had larger changes. As the sum of $\Delta[HbO_2]$ and $\Delta[Hb]$, ΔTHC followed the larger change of $\Delta[HbO_2]$. Relatively stable cerebral hemodynamic variables were found at rest, since there were no physiological changes. During HUT, rCBF decreased slightly due to the increase of cerebral vasculature resistance as well as the decrease of cardiac output induced by orthostatic stress [151]. Previous studies have also found reduced CBFV during HUT [152]. The decreased rCBF caused the reduction of oxygen delivery. Consequently, $\Delta[HbO_2]$ decreased while $\Delta[Hb]$ increased. During the protocol of paced breathing at 0.1 Hz, MAP and cerebral hemodynamics showed slight fluctuations. In total, similar trends to this subject were observed in eight of the 15 subjects. However, the other seven subjects exhibited slight decreases in rCBF and $\Delta[HbO_2]$ during paced breathing (data not shown). This was due to that the relatively slow and deep breathing at 0.1 Hz might induce hypocapnia [150] and lead to a vasoconstriction. As a result, rCBF and $\Delta[HbO_2]$ decreased in those subjects.

Figure 4.5 shows typical PSDs of all measured physiological variations at the three physiological conditions. All PSDs were quantified from the time-course data of the same subject shown in Figure 4.4. Since similar results were found in both hemispheres, only data acquired from the left hemisphere are presented. At rest, small PSD peaks exhibited in MAP (Figure 4.5a1) and rCBF (Figure 4.5b1) in the low frequency range. During HUT, obvious peaks around 0.08 Hz were found in PSDs of all physiological variables (Figures 4.5a2, 4.5b2, 4.5c2, 4.5d2, and 4.5e2). Meanwhile, the PSD signals in the low frequency range were significantly enhanced. Similar to the results during HUT,

paced breathing at 0.1 Hz created PSD peaks around 0.1 Hz in all parameters (Figures 4.5a3, 4.5b3, 4.5c3, 4.5d3, and 4.5e3). The intensities of LFOs were represented by the magnitudes of PSD(f) in the low frequency range (0.05 to 0.15 Hz). The SNR of LFOs in MAP and cerebral hemodynamic variables were improved in the protocols of HUT and paced breathing. Among these physiological variables, least SNR in detecting LFOs was found in Δ[Hb] (Figures 4.5d1, 4.5d2, 4.5d3).
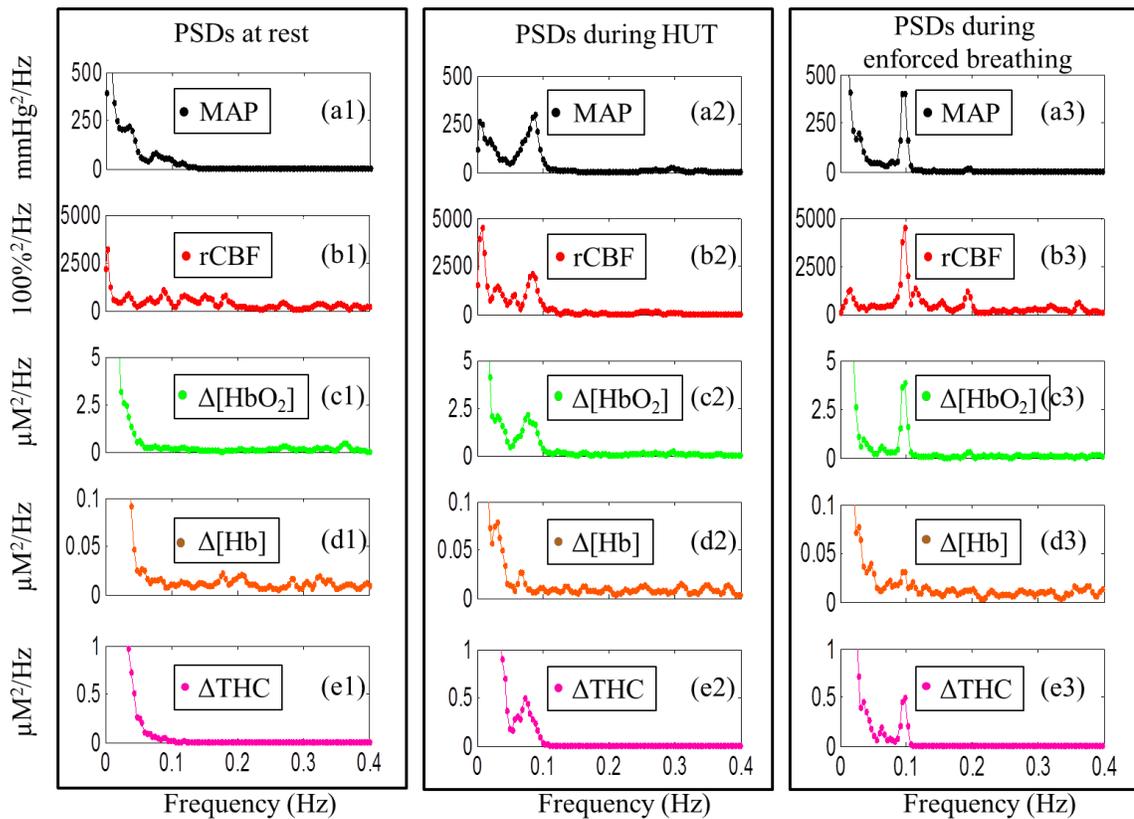
Figure 4.5 PSDs of MAP and cerebral hemodynamics under three physiological conditions in subject's left hemisphere.
(a1), (b1), (c1), (d1) and (e1): PSDs at rest; (a2), (b2), (c2), (d2) and (e2): PSDs during HUT; (a3), (b3), (c3), (d3) and (e3): PSDs during paced breathing.

The relationship (phase shift and coherence) between the LFOs of each paired signals was shown in Figure 4.6. The data in Figure 4.6 were obtained from the same subject's left hemisphere (Figures 4.4 and 4.5), and similar results were found in

subject's right hemisphere (data not shown). At rest, all paired variables had low levels of coherence. The Coh(f) higher than 0.4 were only found in a few points (Figures 4.6a1, 4.6b1, 4.6c1, 4.6d1). During HUT and paced breathing at 0.1 Hz, coherences higher than 0.4 were mostly observed in the low frequency range of 0.05 to 0.1 Hz (Figures 4.6a2, 4.6b2, 4.6d2) or 0.09 to 0.11 Hz (Figures 4.6a3, 4.6b3, 4.6c3, 4.6d3), except the pair of MAP and Δ[Hb] (Figure 4.6c2).
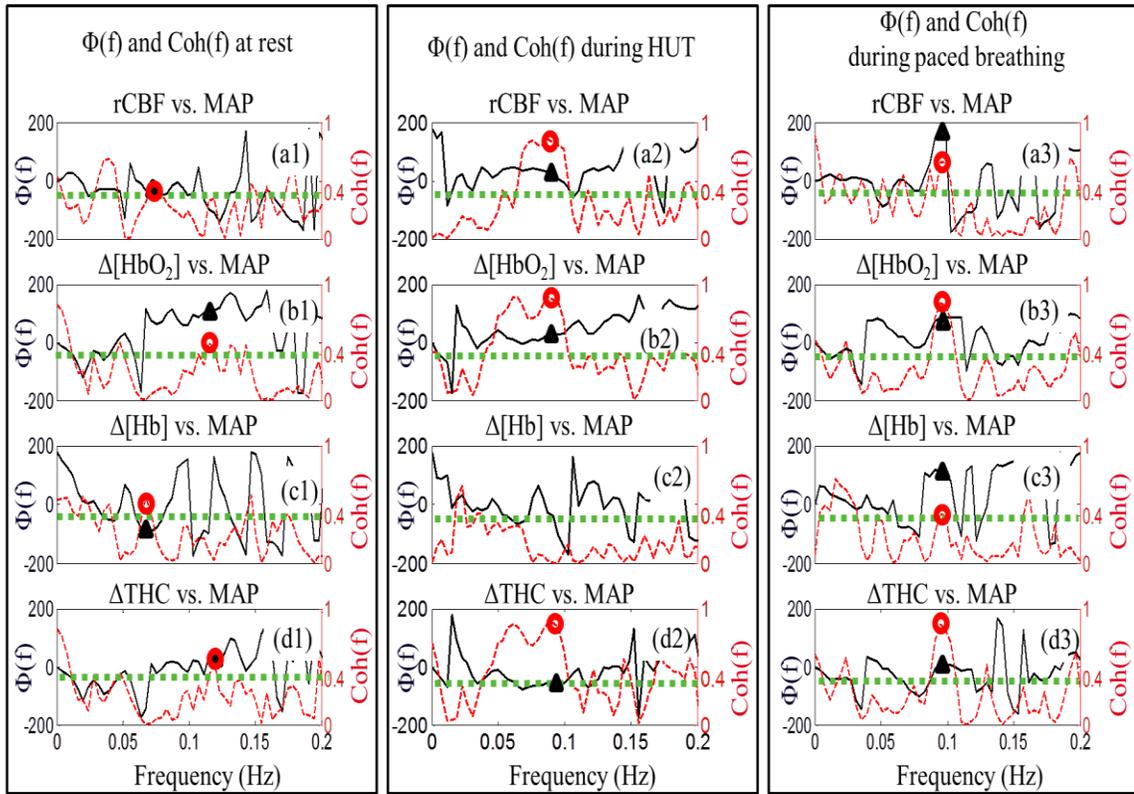
Figure 4.6 Phase ($\Phi(f)$) and coherence (Coh(f)) spectra of paired signals between the MAP and each of the cerebral hemodynamic parameters under three physiological conditions in subject's left hemisphere.
(a1), (b1), (c1) and (d1): spectra at rest; (a2), (b2), (c2) and (d2): spectra during HUT; (a3), (b3), (c3) and (d3): spectra during paced breathing. The solid lines represent the $\Phi(f)$ and the dashed lines represent the Coh(f). The horizontal dashed lines indicate the coherence threshold Coh = 0.4. The circles indicate the largest coherences within the low frequency range. The triangles indicate the most reliable phase shifts within the low frequency range.

4.3.2 Average Results
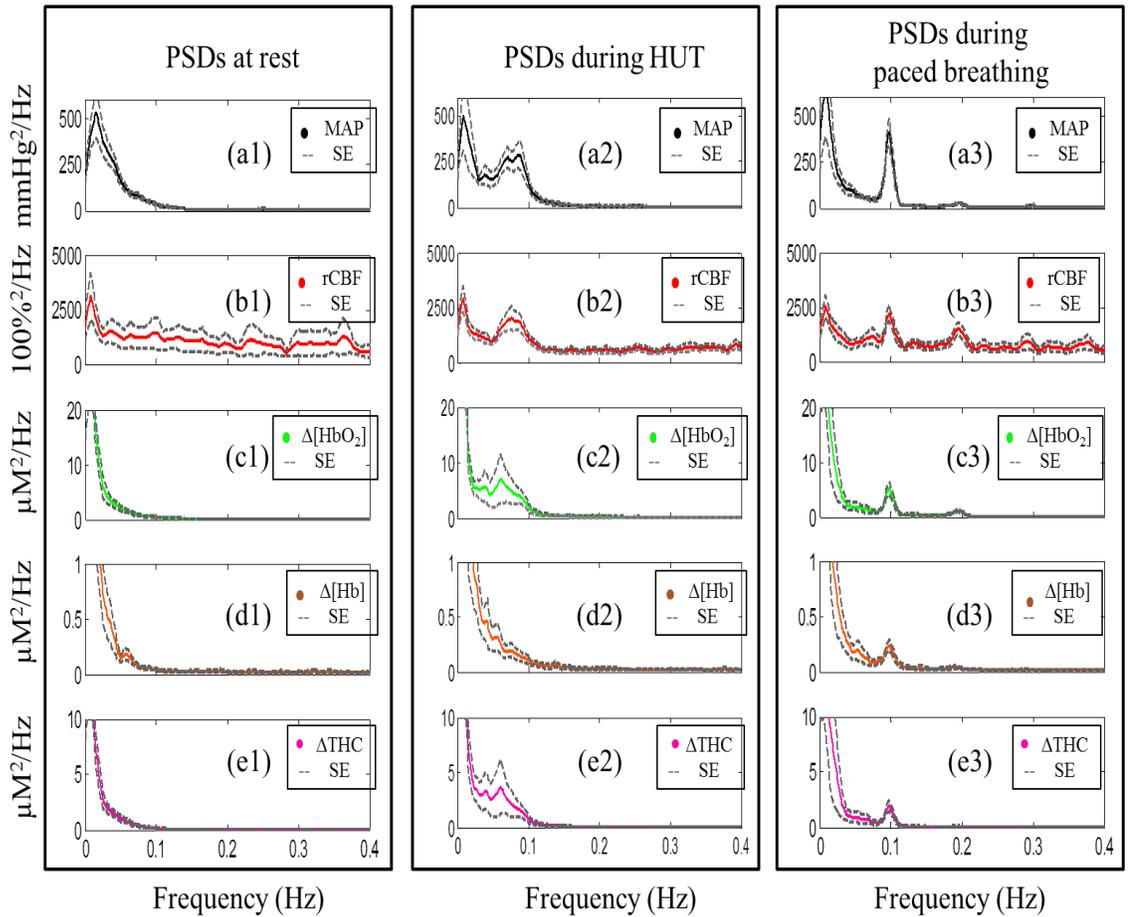
Figure 4.7 Average PSDs of MAP and cerebral hemodynamic parameters over subjects (n = 15) under three physiological conditions in subject's left hemispheres. The solid curves indicate the mean value of PSDs while the dashed curves surrounding the dashed curve represent the range of data variations (standard errors).

Fifteen healthy subjects were tested in this study. The average PSDs of MAP and cerebral hemodynamic parameters in the left hemispheres over 15 subjects under the three physiological conditions are presented in Figure 4.7. Data are shown as mean ± standard error. Results in the right hemispheres were similar (data not shown). Similar trends were found in the average and individual (Figure 4.5) PSDs. Δ[Hb] had smaller average LFO amplitudes under all physiological conditions ($\leq$ 0.23 μM^2/Hz) than

$\Delta[HbO_2]$ (≥ 0.69 $\mu M^2/Hz$) and ΔTHC (≥ 0.32 $\mu M^2/Hz$). Compared to resting state, both

HUT and paced breathing generated larger increases in LFO amplitudes.

Table 4.1 Average LFO frequencies, leading times, phase shifts, and success rates of cerebral hemodynamic LFO measurements

Number of Subjects (n = 15) Significant level of Coh (Coh > 0.4)		Average LFO frequencies (Hz) Average leading times (second) Average phase shifts (degree) (Number of successful measurements; Success rates)			
		rCBF	$\Delta[HbO_2]$	$\Delta[Hb]$	ΔTHC
Rest	Left side	0.078 ±0.011 1.77 ±1.72 49.3 ±46.2 (13; 87%)	0.079 ±0.012 1.54 ±1.65 48.6 ±48.2 (10; 67%)	0.080 ±0.010 0.08 ±3.84 4.7 ±122.4 (7; 47%)	0.078 ±0.012 0.76 ±1.48 23.6 ±44.8 (11; 73%)
	Right side	0.086 ±0.014 0.95 ±1.61 29.7 ±49.9 (12; 80%)	0.084 ±0.010 1.27 ±1.17 41.1 ±32.8 (11; 73%)	0.080 ±0.008 -0.93.±3.11 -31.1 ±92.6 (9; 60%)	0.083 ±0.010 0.26 ±1.22 7.0 ±35.9 (11; 73%)
HUT	Left side	0.076 ±0.010 1.65 ±0.65 45.7 ±19.1 (15; 100%)	0.076 ±0.010 1.16 ±0.59 29.5 ±11.8 (15; 100%)	0.074 ±0.009 -1.18 ±4.09 -38.1±117.1 (11; 73%)	0.076 ±0.009 -0.37 ±0.53 -11.3 ±16.6 (15; 100%)
	Right side	0.076 ±0.010 1.66 ±0.63 45.3 ±16.7 (15; 100%)	0.076 ±0.010 0.96 ±0.59 24.4 ±12.7 (15; 100%)	0.076 ±0.011 -1.48 ±4.06 -45.6 ±99.6 (13; 87%)	0.076 ±0.009 -0.54 ±0.69 -16.9 ±22.5 (15; 100%)
Paced breathing at 0.1 Hz	Left side	0.098 ±0.003 2.14 ±2.40 68.0 ±88.9 (14; 93%)	0.097 ±0.002 1.42 ±0.82 68.9 ±45.4 (14; 93%)	0.098 ±0.007 -0.03 ±2.91 -16.2 ±111.3 (13; 87%)	0.097 ±0.002 0.57 ±1.24 20.1 ±41.4 (15; 100%)
	Right side	0.097 ±0.002 2.60 ±2.11 77.7 ±80.4 (14; 93%)	0.098 ±0.003 1.66 ±0.93 60.3 ±32.7 (15; 100%)	0.097 ±0.002 -0.97 ±3.04 -22.9 ±99.7 (13; 87%)	0.097 ±0.002 0.47 ±1.24 9.3 ±41.6 (15; 100%)

Reliable LFOs and phase shifts were selected by the coherence level larger than 0.4 (Chapter 4.2.3). Table 4.1 and Figure 4.8 show the summary of LFO frequencies, leading times, phase shifts, and success rates for detecting reliable LFOs. Data are shown as mean ± standard deviation unless otherwise noted. Since the LFO leading times were

calculated from phase shifts, leading times and phase shifts revealed equivalent information about the relationship between the MAP and cerebral hemodynamic parameters. For simplicity, we only discuss phase shifts. Δ[Hb] results (Table 4.1 and Figure 4.8) are excluded in the following reports due to its large signal variations ($92.6° \leq$ std(Φ) $\leq 122.4°$) and low success rates (47 to 87%).
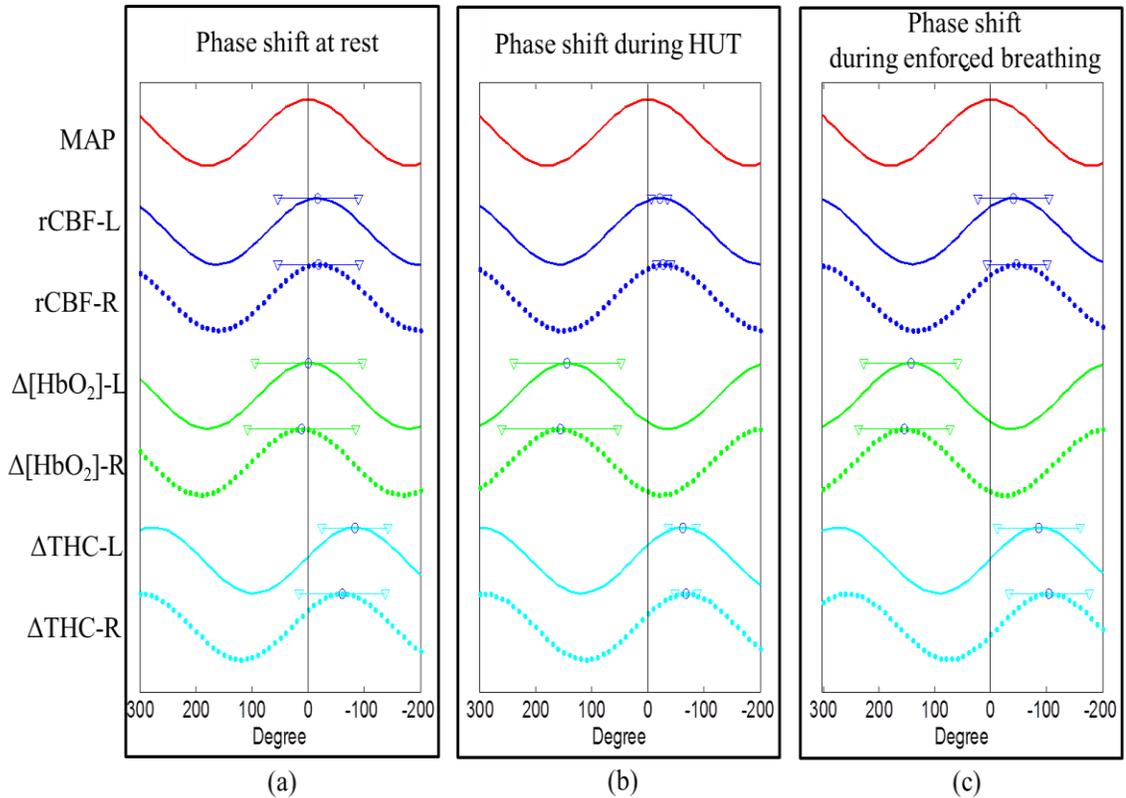
Figure 4.8 Average phase shifts of cerebral hemodynamics relative to MAP over 15 subjects under three physiological conditions in left and right hemispheres.
(a) phase shifts at rest; (b) phase shifts during HUT; (c) phase shifts during paced breathing. For cerebral hemodynamic data, the solid and dashed curves demonstrate the signals obtained form left and right hemispheres, respectively. The vertical lines indicate the peaks of MAP oscillations. The empty circles indicate the peaks of cerebral hemodynamic oscillations. The error bars represent the standard deviations of the phase shifts.

70

At rest, relatively low success rates (67 to 87%) were observed in detecting LFOs. Moreover, LFO frequencies were obtained in a relatively wide range (0.078 to 0.086 Hz). The phase shifts exhibited relative large standard deviations ($32.8° \leq std(\Phi) \leq 49.9°$). Also, relatively large differences between the phase shifts in left and right hemispheres were obtained in cerebral hemodynamic parameters ($7.5° \leq |\Phi_{left} - \Phi_{right}| \leq 19.6°$).

During HUT, success rates in capturing LFOs were 100% for all hemodynamic parameters (except $\Delta[Hb]$) from both hemispheres. LFO frequencies appeared at ~0.076 Hz. Compared to the results at rest, the standard deviations of phase shifts were much smaller ($11.8° \leq std(\Phi) \leq 22.5°$) during HUT (Table 1 and Figure 4.8). There were minor differences in phase shifts between left and right hemispheres ($0.4° \leq |\Phi_{left} - \Phi_{right}| \leq 5.6°$).

During paced breathing at 0.1 Hz, rCBF, $\Delta[HbO_2]$ and ΔTHC showed high success rates (93 to 100%). LFO frequencies exhibited at ~0.1 Hz as expected. However, phase shifts had much larger standard deviations ($32.7° \leq std(\Phi) \leq 45.4°$ for $\Delta[HbO_2]$ and ΔTHC, and $80.4° \leq std(\Phi) \leq 88.9°$ for rCBF) compared to those during HUT (Table 1). Also, phase shift differences between left and right hemispheres ($8.6° \leq |\Phi_{left} - \Phi_{right}| \leq 10.8°$) were larger than those exhibited during HUT.

4.4 Discussion

4.4.1 NIRS/DCS Technologies Facilitate Detection of LFOs in Cerebral Hemodynamics

Although NIRS has been previously employed to investigate LFOs in cerebral microvasculature [7, 148], it cannot measure tissue CBF directly. Moreover, cerebral tissue hemodynamics (i.e., CBF and cerebral oxygenation) are usually interactive and

coupled. It is thus crucial to directly and simultaneously quantify multiple cerebral hemodynamic parameters in microvasculature. Nevertheless, only a few studies have aimed to concurrently detect LFOs in CBFV and cerebral oxygenation [7, 153]. In the present study, we demonstrated, *for the first time*, that DCS can detect LFOs of CBF and that the upgraded hybrid NIRS/DCS device can simultaneously capture multiple LFOs of cerebral hemodynamic variables (i.e. rCBF, $\Delta[HbO_2]$, $\Delta[Hb]$ and ΔTHC). Multiple hemodynamic parameters from both cerebral hemispheres were simultaneously acquired using two hybrid fiber-optic probes, and then used to calculate cerebral LFOs.

4.4.2 Comparison of LFOs among Different Hemodynamic Parameters under Different Physiological Conditions

Among these hemodynamic parameters, LFOs of rCBF, $\Delta[HbO_2]$ and ΔTHC had relatively stable phase shifts ($std(\Phi) \leq 88.9°$) and were detected at reasonable success rates ($\geq 67\%$) under the three physiological conditions. Compared to other variables, LFOs of $\Delta[Hb]$ were much weaker, which agreed with previous findings [7, 148]. As a consequence, the phase shifts of $\Delta[Hb]$ had large variations. The weak LFOs of $\Delta[Hb]$ were likely caused by the low amplitude of $\Delta[Hb]$ in cerebral blood. Cerebral blood has a high oxygen saturation varying from almost 100% in arterial blood to ~60% in venous blood, indicating the small percentage of [Hb] in cerebral blood [154]. It is also possible that the cerebral venula (containing more [Hb]) is less responsible to blood pressure variations than the arteriole (containing more $[HbO_2]$) [155]. As a result, $\Delta[Hb]$ exhibited the least magnitude and SNR of LFOs, and was therefore excluded from the following discussions.

LFOs at rest were weak, resulting in low SNRs [150]. As a result, success rates were low and LFO frequencies, phase shifts, and phase differences between the two hemispheres had large variations (SDs) at rest. HUT and paced breathing significantly enhanced LFOs through different mechanisms. During paced breathing, LFOs at 0.1 Hz were elevated by respiration-induced MAP oscillation [150]. However, there were large inter-subject variations in phase shifts of cerebral hemodynamics, which might be attributed to the heterogeneous responses to paced breathing among subjects. The hypocapnia might be induced by relatively deep and slow breathing pattern used in the present study, resulting in increased variations in cerebral hemodynamics [150]. LFOs during HUT were enhanced probably through the increased sympathetic nervous activity [142, 151]. Previous study has demonstrated that a single burst in sympathetic nervous system can initiate a cycle of increasing and decreasing arterial pressure at ~0.1 Hz via the baroreflex feedback loop [156]. The sympathetic nervous activity bursts in series each ~10 s during HUT [157], which can significantly enhance LFOs of MAP through baroreflex resonance. Moreover, compared to the paced breathing protocol, the HUT protocol is easier to control and more objective. Overall, signals obtained during HUT were most stable (smallest standard deviations) and robust (highest success rates) among the three physiological conditions.

4.4.3 Comparison of LFO Measurements with Other Studies

Transfer function analysis has been used by several research groups to study LFOs in cerebral hemodynamics at rest [142, 146, 147], during HUT [142, 146, 147] and during paced breathing at 0.1 Hz [7, 26, 148]. However, no one has ever quantified

cerebral LFOs under all three physiological conditions in a single study. Therefore, our results were compared respectively to those with comparable data in corresponding physiological condition.

At rest, success rates and phase shifts of LFOs in CBF measured by DCS ($80\% \leq$ success rate $\leq 87\%$, $29.7° \leq \Phi \leq 49.3°$, n = 15) are in reasonable agreement with those of CBFV measured by TCD ($92\% \leq$ success rate $\leq 100\%$, $44.9° \leq \Phi \leq 56.3°$, $20 \leq n \leq 50$) [142, 146, 147].

During HUT, our results of LFOs in CBF (success rate = 100%, $45.3° \leq \Phi \leq 45.7°$, n = 15) are similar to those in CBFV (success rate = 100%, $40.6° \leq \Phi \leq 50.2°$, $20 \leq n \leq 47$) [142, 146, 147].

It is not surprising that the LFO frequencies obtained during paced breathing at 0.1 Hz in the present study are highly consistent with other studies [7, 26, 148]. During paced breathing, success rates for extracting reliable LFOs of cerebral hemodynamics ($\geq$ 93% for rCBF and $\Delta[HbO_2]$, 100% for ΔTHC, n = 15) in the present study are close to those (100% for CBFV and $\Delta[HbO_2]$, 97% for ΔTHC, n = 38) documented by Reinhard et al [7]. The phase shifts in CBF ($68.0° \leq \Phi \leq 77.7°$, n = 15) are also similar to those in CBFV ($64.8° \leq \Phi \leq 70.5°$, $38 \leq n \leq 50$) recorded by Reinhard et al and Diehl et al [7, 26]. However, inter-subject variations of phase shifts in CBF ($80.4° \leq std(\Phi) \leq 88.9°$, n = 15) extracted in our study are much larger than those in CBFV ($26.1° \leq std(\Phi) \leq 29.8°$, $38 \leq n \leq 50$) [7, 26]. These large fluctuations might be attributed to the fact that the CBF in microvasculature is more sensitive to the hypocapnia induced by the paced respiration than the CBFV in large cerebral vessels [158]. In addition, the phase shifts of $\Delta[HbO_2]$ ($68.9 \pm 45.4°$ and $60.3 \pm 32.7°$ for the left and right hemisphere, respectively, n = 15) are

quite different from the results measured by Reinhard et al. (Φ = -23.5 $\pm$ 23.9 °, n = 38) and Obrig et al. (Φ = ~0°, n = 3) [7, 148]. Phase shifts of LFOs in ΔTHC in our measurements (20.1 $\pm$ 41.4 ° and 9.3 $\pm$ 41.6 ° for the left and right hemisphere, respectively, n = 15) are also distinct from those (Φ = -22.6 $\pm$ 30.5 °, n = 38) reported by Reinhard et al [7]. The causes for these differences are unclear. Several factors are likely to be involved, such as number of subjects and age differences among studies, tissue heterogeneity responses (e.g., different penetration depths using different S-D separations of 3 to 5 centimeters for oxygenation measurements), instrumentation differences (e.g., frequency-domain versus continuous-wave), vascular reactivity differences in response to CO_2 oscillations during paced breathing, and subject training differences for controlled breathing.

4.4.4 Study Limitations

NIR measurements with S-D separations of 2.5 and 3 cm have similar sensitive areas and penetration depths. However, it should be noticed that optical fibers for DCS and NIRS in our hybrid fiber-optic probe (Figure 4.1a) were arranged in a special pattern to minimize the interference between DCS and NIRS measurements [77]. As a result, the centers of our DCS and NIRS fiber pairs were not aligned precisely in the plane of forehead, which may result in slight difference in detection regions for DCS and NIRS measurements. Tissue heterogeneous responses from different regions may lead to certain discrepancy between the DCS and NIRS measurements.

The physiological manipulations used (i.e., HUT and enforced breathing) in this study to enhance LFOs may not be easily performed in some patient populations. For

example, it may be difficult for patients with vascular diseases to keep their breathing at a low frequency of 0.1 Hz for 10 minutes. Furthermore, the HUT may induce vasovagal syncope in both health and disease populations [159].

Cerebral hemodynamics is also influenced by the changes in arterial carbon dioxide (CO_2) content via changes in respiration (e.g., enforced breathing). Therefore, future study should also include the assessments of CO_2 and respiratory rate [181].

For comparison purposes, successful LFO measurements were characterized by coherence level larger than 0.4, which is an empirical value. In fact, the significant level of coherence should be determined statistically. More specifically, LFO measurements are considered successful if the coherence coefficient is significantly different from 0 [150]. Using this objective criterion for judging the coherence level would increase the success rates of our LFO measurements.

4.5 Conclusions

A novel hybrid NIRS/DCS device was successfully upgraded and used for concurrent measurements of LFOs of rCBF and cerebral oxygenation (i.e., $\Delta[HbO_2]$, $\Delta[Hb]$ and ΔTHC). Cerebral hemodynamic LFOs in the left and right hemispheres were measured and compared under three different physiological conditions (i.e., at rest, during HUT, and during paced breathing). rCBF, $\Delta[HbO_2]$, and ΔTHC were found to be reliable hemodynamic parameters in detecting LFOs. Among the three physiological conditions, HUT was determined as the most robust and stable protocol for quantifying phase shifts of LFOs in hemodynamic parameters. Success rates in detecting cerebral LFOs were close to those in other relevant studies. Future study will investigate cerebral

LFOs in patients with cerebral disease/damage (e.g., stroke, carotid stenosis, and neurocognitive impairment) and evaluate their dynamic CA via the determination of LFO phase shifts. It is expected that direct and concurrent measurements of LFOs in CBF and cerebral oxygenation will bring new and informative perspectives about mechanisms of CA and pathologies of diseases/damages in the brain.

CHAPTER 5 DIFFUSE OPTICAL MONITORING OF CEREBRAL HEMODYNAMICS FOR THE PREDICTION OF VASOVAGAL SYNCOPE

5.1 Background

During the HUT tests as described in Chapter 4, several healthy subjects experienced vasovagal presyncope symptoms (i.e., a sudden drop in blood pressure, dizziness, blurred vision, sweating, and heart palpitation). Dramatic decreases in CBF were also observed in these subjects. It is known that when cerebral vasculature loses its ability to maintain the CBF above a critical level (i.e., failure of CA), vasovagal syncope (VVS) may occur [14]. Although our previous studies have evaluated dynamic CAs in TD (Chapter 3) and FD (Chapter 4), cerebral hemodynamics at the condition of losing CA has not been monitored. Therefore, more healthy subjects were recruited in this study to continuously monitor cerebral hemodynamics and MAP during VVS using the novel dual-wavelength DCS flow-oximeter (Chapter 2.5) and a finger plethysmography.

VVS, the most commonly occurring syncope, has been widely studied using HUT test [15, 16]. Central hypovolemia [160, 161] and increased sympathetic outflow [161-163] induced by HUT may eventually trigger a vasovagal reaction which is a malfunctioning of autonomic nervous system. The vasovagal reaction results in decreases in blood pressure and heart rate which may lead to VVS even in healthy volunteers [17]. The pathophysiology of vasovagal reaction is not fully known. However, sudden drops in arterial blood pressure, CBFV in the MCA, and cerebral oxygenation have been previously observed during VVS [164, 165]. Simultaneous and continuous quantification

of these physiological parameters during VVS is rare, but critical for predicting VVS and determining which variable eventually triggers VVS.

The sudden decrease of blood pressure is well known to be an indicator for developing VVS. Thus, ABP has been measured continuously in previous studies using a finger plethysmograph or an invasive catheter [165-167]. TCD has been frequently used to monitor CBFV in large cerebral vessel (e.g., MCA) in these studies [165-167]. Some studies have measured ABP and CBFV [166] or ABP and cerebral oxygenation [168] simultaneously to determine which variable triggers VVS. Rapid declines in cerebral hemodynamics during VVS were found occurring earlier than ABP drops [166, 168]. So far very few studies have assessed dynamic changes of ABP, CBFV, and cerebral oxygenation concurrently during VVS [152, 167]. However, these studies did not intend to quantitatively determine the eventual trigger of VVS.

In this study, a finger plethysmograph and a novel custom-designed dual-wavelength DCS flow-oximeter (Chapter 2.5) were used to simultaneously monitor MAP, dynamic changes of CBF and concentration changes of oxygenated- ($\Delta[HbO_2]$), deoxygenated- ($\Delta[Hb]$) and total hemoglobin (ΔTHC) in healthy subjects during 30-minute $70°$ HUT tests. The ability of maintaining stable MAP, CBF and cerebral oxygenation was challenged by the HUT. Instability of these parameters may result in VVS. Dynamic changes in multiple physiological variables (i.e., MAP, CBF, $\Delta[HbO_2]$, $\Delta[Hb]$ and ΔTHC) were continuously monitored during the postural change (i.e., HUT). The ultimate goals are to evaluate each parameter's sensitivity to predict VVS and investigate which variable eventually triggers VVS.

5.2 Methods

5.2.1 Subjects

Table 5.1 Subject characteristics

Subject	Sex	Age (years)	Values at Supine		HUT Duration (min)	Valid Measurements during HUT		
			MAP (mm Hg)	HR (BPM)		MAP (%)	CBF (%)	Oxygenation (%)
Presyncope Group (N = 6)								
S1	F	57	95	70	15.4	√	√	√
S2	F	60	105	62	2.7	N/A	√	N/A
S3	F	60	81	71	10.6	√	√	N/A
S4	F	39	82	77	5.9	√	√	√
S5	M	40	72	58	2.5	√	√	√
S6	M	24	96	50	9.3	√	√	√
Control Group (N = 8)								
C1	M	47	83	67	30.0	√	√	√
C2	M	55	77	70	30.0	√	√	√
C3	M	59	79	65	30.0	√	√	√
C4	F	51	95	77	30.0	√	√	√
C5	F	48	85	80	30.0	√	√	√
C6	F	46	75	61	30.0	√	√	√
C7	F	33	87	66	30.0	√	√	√
C8	M	26	80	63	30.0	√	√	√

Fourteen healthy adults (6 males and 8 females) without known cerebral or cardiac diseases were recruited in this study (Table 5.1). All participants signed consent forms approved by the University of Kentucky Institutional Review Board. Six (2 males and 4 females) out of the fourteen subjects experienced presyncopal symptoms (i.e., sudden drop in blood pressure, sweating, dizziness, blurred vision, and heart palpitation) during $70°$ HUT. For comparisons, the remaining 8 subjects without presyncope were used as a control group. MAP data from one subject with presyncope (S2) was excluded due to its poor SNR. Two subjects with presyncope (S2 and S3) did not have oxygenation

data since one of the two lasers in DCS flow-oximeter was not working properly during the measurements.

5.2.2 Experimental Protocol

Relative changes of rCBF, $\Delta[HbO_2]$, $\Delta[Hb]$, and ΔTHC during HUT were monitored by the custom-designed dual-wavelength DCS flow-oximeter. Here "r" denotes the relative change with the unit %, while "Δ" indicates the absolute change in unit of μM. Details about the DCS flow-oximeter can be found in Chapter 2.5. A fiber-optic probe was taped in the middle of forehead at the position of 1 cm above the eyebrows for the optical measurements of cerebral hemodynamic parameters. The separation between source and detector fibers was 2.5 cm. To fix the probe on the frontal head, a self-adhesive elastic band was used to wrap the probe tightly around the forehead. The noninvasive finger plethysmograph (Portapres, FMS Inc., Netherlands) was used to continuously monitor the beat-to-beat MAP in unit of mm Hg and heart rate (HR) in unit of beats-per-minute (BPM). The plethysmograph finger sensor on the middle finger of left hand was maintained at the heart level. Data sampling rate for both optical and MAP/HR measurements is 1 Hz.

A 30-minute 70 ° HUT protocol was adopted in the present study, which is similar to the 10-minute 70 ° HUT protocol described in Chapter 4. This protocol was selected because previous studies had found that it may induce VVS in healthy subjects [159, 169]. More specifically, the subject was asked to lay supine on a tilt table. To immobilize the body, two Velcro strips were placed over the chest and thighs respectively. Following the supine control for ~10 minutes, the subject was tilted up to 70 ° and instructed to remain

still for 30 minutes if possible. However, when presyncopal symptoms appeared during standing at 70 °, the subject was tilted back to supine position immediately for recovery. The recovery period at supine position was ~5 minutes.

5.2.3 Data Analysis

To reduce high frequency noise, a 10-point sliding average was applied on all raw data. The averaged data from the 30-second right before the onset of HUT were used to represent their baseline values at supine position, since the supine MAP and HR were fairly stable. In order to compare HUT induced changes among the measured parameters (i.e., MAP, rCBF, $\Delta[HbO_2]$, $\Delta[Hb]$, ΔTHC) with different units, we normalized (divided) all variables respectively to the averaged values of the 30-second data segment immediately after the tilt table was positioned to 70 °. rMAP, rCBF, $r[HbO_2]$, $r[Hb]$, and rTHC indicated the relative values normalized (divided) by their baseline values, respectively. For quantifying $r[HbO_2]$, $r[Hb]$ and rTHC, baseline values of these variables were assigned to be 23.6, 13.0 and 37.5 μmol/L, respectively, according to the literature [170]. All baselines were assigned to be 100% after the normalization.

Similar to previous results in others' studies [163, 164, 167], subjects with presyncope exhibited two stages of physiological responses during HUT (see Figure 5.1 and Figure 5.2 in Chapter 5.3): a slow and gradual change in each measured variable at Stage I before a break-point and a rapid and dramatic change at Stage II after a break-point. In presyncope subjects, the maximum changes in all measured variables occurred at Stage II. To compare the sensitivities of measured variables for predicting VVS, we

quantified the minimum values of rMAP, rCBF, r[HbO$_2$], and rTHC, and maximum of r[Hb] in control and presyncope subjects during HUT. To determine which variable triggered the VVS, we evaluated the onset time of rapid/dramatic dynamic changes before presyncope following the method suggested by Dan et al [166]. Briefly, the measured time course data during HUT for each variable were linearly fitted by two straight lines which represent the slow and rapid changes, respectively [166]. The two straight lines (Figure 5.1(b) and Figure 5.2(a)) were connected at a break-point. We moved the break-point from the beginning to the end of HUT along each dataset, and calculated the corresponding mean squared errors (MSEs) of the linear best fittings. The final break-point separating the two stages was selected at the time point where the smallest MSE was observed. Time differences of break-points between the rMAP and each of the other hemodynamic parameters (i.e., rCBF, r[HbO$_2$], r[Hb], rTHC) were quantified for comparison.

The differences of mean values between the presyncope and control groups were tested by two-tailed Student t-tests. The time differences of break-points between rMAP and each of the other hemodynamic parameters were compared with zero using two-tailed paired Student t-tests. P-values less than 0.05 are considered significant. All average results are presented as mean $\pm$ standard deviation (SD).

5.3 Results

5.3.1 Individual Results

Figure 5.1 shows illustrative results of MAP and cerebral hemodynamics from a control subject (C1 in Table 5.1) without presyncope (Figure 5.1a), and a subject (S1 in Table 5.1) with presyncope (Figure 5.1b) and corresponding MSEs of the two-line fittings (Figure 5.1c). Sudden changes at the onset of HUT were observed in all measured parameters from the two subjects (Figures 5.1a and 5.1b). During HUT, all variables in the control subject (C1) were relatively stable (Figure 5.1a). In the control subject, the minima of rMAP, rCBF, $r[HbO_2]$ and rTHC (C1) were 85%, 68%, 96% and 95% of the 30-second mean value right after tilt-onset (assigned to be 100%), respectively, and the maximum r[Hb] was 129% (Figure 5.1a). By contrast, most parameters measured from the presyncope subject (S1) showed relatively larger variations. The rCBF reduction during HUT was associated with a decrease in $r[HbO_2]$ and an increase in r[Hb]. Since $[HbO_2]$ accounts for more than 60% of the THC in CBF [154], rTHC primarily followed the trend of $r[HbO_2]$. Two stages of physiological responses were observed in the measured variables during HUT including slow and gradual changes at Stage I and rapid and dramatic changes at Stage II. For each parameter, the break-point between the two stages was determined mathematically by the minimum value of MES. However, nadirs of MSEs were not always clear in all measured parameters. The maximum changes during HUT were observed at Stage II. The minimum value of rCBF (15%) was much smaller than those of rMAP (67%), $r[HbO_2]$ (65%) and rTHC (94%). The maximum r[Hb] was 150%. The onset times of rapid changes in rCBF, $r[HbO_2]$, r[Hb], and rTHC at the break-points were -3, +231, +320, and +234 seconds relative to that of rMAP,

respectively (Figures 5.1b and 5.1c). The positive or negative value of each onset time indicated that the rapid and dramatic change of the measured parameter occurred later or earlier than that of rMAP (as a zero reference for the comparison).
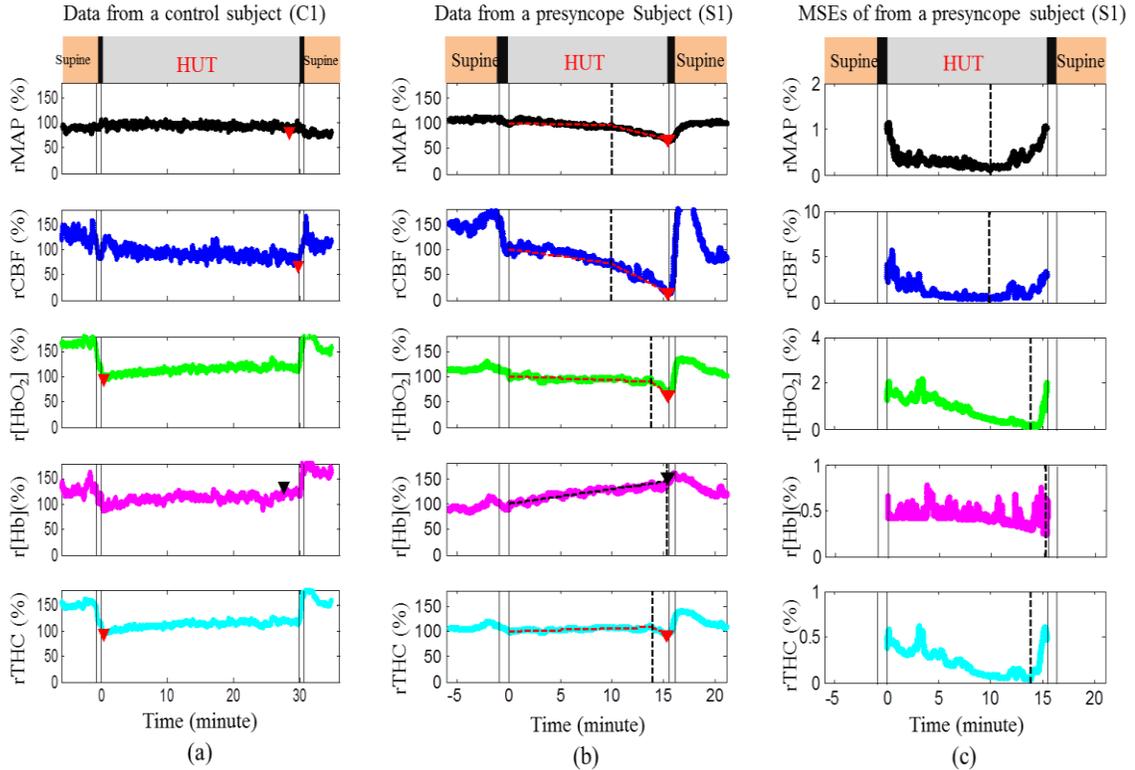
Figure 5.1 MAP and cerebral hemodynamics from a control subject (a) and a presyncope subject (S1) (b), and corresponding MSEs of the two-line linear fittings in the subject with presyncope (S1) (c).
During HUT, all measured variables were relatively stable in the control subject (C1) but exhibited two-stage physiological responses in the subject (S1) with presyncope (i.e., slow and gradual changes at Stage I, and rapid and dramatic changes at Stage II). The solid vertical lines indicate the beginning and ending of tilting up and tilting down. The triangles indicate the minima of rMAP, rCBF, r[HbO$_2$] and rTHC, and the maximum of r[Hb] during HUT. The two connected dashed lines on top of the raw data (b) demonstrate the two-line fitting results. The dashed vertical lines indicate the break-points separating the Stage I and Stage II.
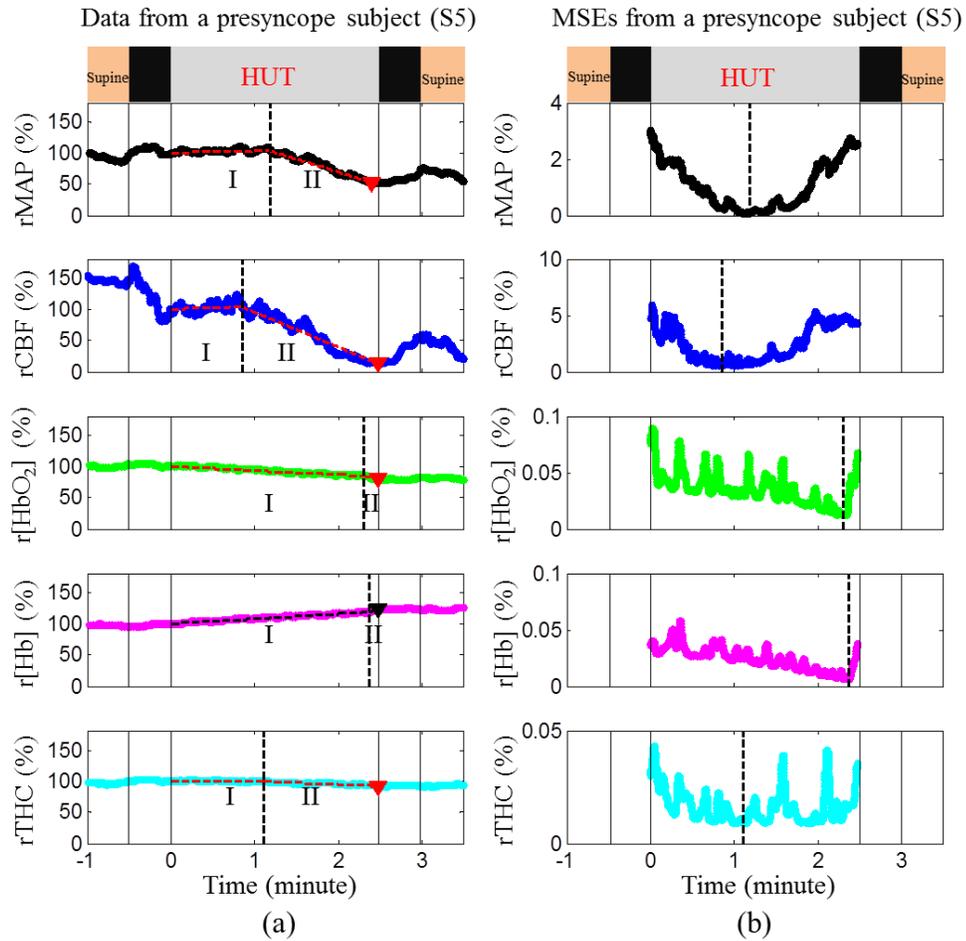
Figure 5.2 MAP and cerebral hemodynamics during HUT (a) and corresponding MSEs of the two-line linear fittings (b) in the subject with presyncope (S5).
All symbols and lines in this figure represent the same meanings as those used in Figure 5.1. Physiological response trends to HUT in this subject were similar to those shown in Figure 5.1 (b) although large variations existed between them in terms of how much and how fast these changes were.

Similar trends were observed from all subjects with presyncope although large inter-subject variations existed among these subjects. Figure 5.2 shows the data from another subject (S5 in Table 5.1) with presyncope. Note that the time scales in horizontal axes of Figure 5.1 and Figure 5.2 were not identical due to the different HUT durations. Similarly, the minimum value of rCBF (15%) at Stage II was much smaller than those of

rMAP (52%), r[HbO$_2$] (80%), and rTHC (92%). The maximum value of r[Hb] was 123%. All variables changed slowly before the break-points at Stage I and quickly thereafter at Stage II. The onset times of rCBF, r[HbO$_2$], r[Hb], and rTHC at the break-points were -20, +68, +72, and -4 seconds relative to that of rMAP, respectively. It should be noticed that the two stages of dynamic changes were more obvious in rMAP and rCBF than those in other variables, and rCBF exhibited greater and earlier decrease at Stage II than other parameters in the subjects with presyncope (Figures 5.1 and 5.2).

5.3.2 Average Results

In the presyncope group, the average time from the beginning of tilting to the onset of presyncope was 7.7 $\pm$ 5.0 minutes. No significant differences in age, supine MAP and HR before tilting were founded between the presyncope and control groups (Table 5.2).

Table 5.2 Average age, supine MAP and HR, and HUT duration

Average Age, Supine MAP and HR, and HUT Duration	Age (years)	Supine MAP (mm Hg)	Supine HR (BPM)	HUT Duration (min)
Presyncope Group (N = 6)	46.7 $\pm$ 14.7	88.4 $\pm$ 12.1	64.6 $\pm$ 10.0	7.7 $\pm$ 5.0
Control Group (N = 8)	45.6 $\pm$ 11.0	82.6 $\pm$ 6.5	68.6 $\pm$ 6.8	30.0 $\pm$ 0.0
All Groups (N = 14)	46.1 $\pm$ 12.2	85.1 $\pm$ 9.4	66.9 $\pm$ 8.2	20.5 $\pm$ 11.8
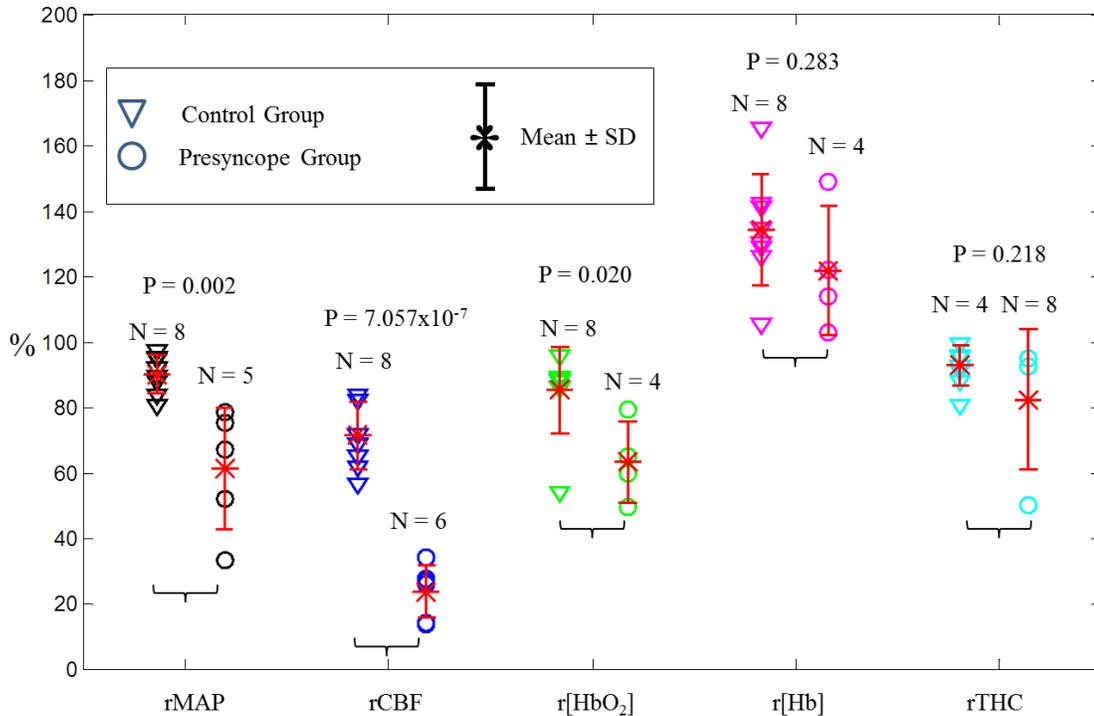
Figure 5.3 Distributions of maximum r[Hb] and minimum rMAP, rCBF, r[HbO$_2$] and rTHC in the control and presyncope groups.
The triangles and circles represent individuals without and with presyncope, respectively. The asteroids with error bars represent the group means $\pm$SDs.

Figure 5.3 shows the minimum values of rMAP, rCBF, r[HbO$_2$] and rTHC, and maximum values of r[Hb] during HUT measured from the subjects with valid data. Compared to control group, presyncope group had significantly lower mean minimum values of rMAP (61 $\pm$19%), rCBF (24 $\pm$8%), and r[HbO$_2$] (64 $\pm$12%). However among these three parameters (i.e., rMAP, rCBF, r[HbO$_2$]), only the minimum values of rCBF exhibited a obvious threshold (~50%) to distinguish all individuals in presyncope group (range: 15 to 35%) from those in control group (range: 57 to 85%). There was a time interval of 80 $\pm$79 seconds (range: 14 to 224 seconds) from rCBF reaching the threshold of 50% decline to the occurrence of presyncope. Furthermore, there were no significant differences in maximum r[Hb] and minimum rTHC between the two groups.
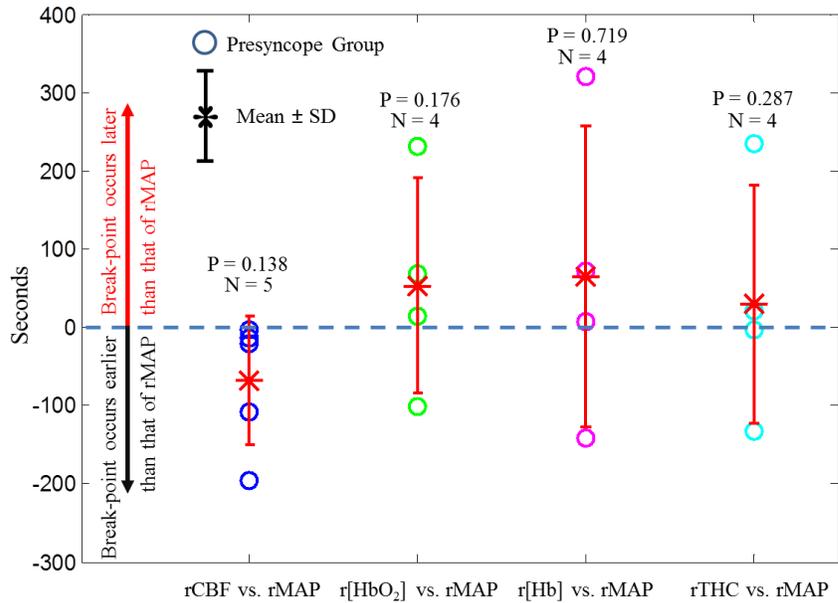
Figure 5.4 Onset time differences at the break-points of rCBF, r[HbO$_2$], r[Hb] and rTHC relative to rMAP in the presyncope group.
The asteroids with error bars represent the group means ± standard deviations. The dashed horizontal line represents 0 second. The negative/positive value below/above the dashed horizontal line (0 second) indicates that the break-point of cerebral hemodynamic parameters (i.e., rCBF, r[HbO$_2$], r[Hb] and rTHC) occurred earlier/later than that of rMAP.

Figure 5.4 displays the time differences at the break-points in rCBF, r[HbO$_2$], r[Hb], and rTHC relative to rMAP in presyncope group. Only rapid changes of rCBF after the break-points occurred consistently earlier (range: 3 to 195 seconds) than those of rMAP in all presyncope subjects compared to the other hemodynamic parameters. On average, the break-points were observed in the sequence of rCBF (-68 ± 82 seconds), rMAP (0 second), rTHC (30 ± 152 seconds), r[HbO$_2$] (53 ± 138 seconds), and r[Hb] (64 ± 192 seconds) when using rMAP as the reference (0 second). However, none of these

time differences at the break-points was significantly different from 0 second (p > 0.05) due to the large data variation and small number of subjects.

5.4 Discussion

Since cerebral hypoperfusion and hypoxia may be the reasons causing the losses of consciousness and postural tone during VVS [164, 165], direct and concurrent measurement of dynamic changes in CBF and cerebral oxygenation during VVS is crucial. A noninvasive device that can simultaneously measure CBF and cerebral oxygenation is appealing for predicting VVS. The novel dual-wavelength DCS flow-oximeter is a portable, rapid, and relatively inexpensive device which offers continuously and concurrently measurements of CBF and cerebral oxygenation during on-going tests [63, 69, 77, 106, 107]. We reported in the present study the first noninvasive and continuous monitoring of both CBF and cerebral oxygenation within the same region of brain cortex during VVS using the emerging DCS flow-oximeter.

Larger variations in MAP and cerebral hemodynamics during HUT were observed in subjects with presyncope (Figures 5.1b and 5.2a) compared to the controls without presyncope (Figure 5.1a). More specifically, MAP, CBF, [HbO$_2$] and THC decreased and [Hb] increased during HUT. These results are consistent with reports from previous studies [133, 152, 165, 168, 171].

We observed two-stage physiological responses during HUT in the presyncope group: slow and gradual changes before the break-points at Stage I, and rapid and dramatic changes after the break-points at Stage II (Figures 5.1b and 5.2a). Other groups also found similar two-stage responses in MAP, CBFV, and [HbO$_2$] during HUT-induced

VVS [152, 165-168]. These changes are expected as HUT caused gradual decreases in MAP and CBF at Stage I which resulted in gradual decreases in [HbO_2] and THC as well as a gradual increase in [Hb]. These gradual and slow changes then reached the break-points leading to Stage II during which physiological autoregulation eventually failed to prevent the sharp dynamic changes in the measured parameters. The maximum changes of all physiological variables occurred after the break-points at Stage II. Taken together, it is anticipated that the abrupt and large physiological changes at Stage II trigged VVS eventually.

Among all the measured variables in subjects with presyncope, rCBF showed the largest changes (76 ± 8% decline) at Stage II compared to rMAP (38 ± 19% decline), r[HbO_2] (36 ± 64% decline), rTHC (18 ± 22% decline), and r[Hb] (22 ± 20% increase) (Figure 5.3). This suggests that rCBF is the most sensitive parameter for the evaluation of VVS. Similar results were previously found in subjects with VVS induced by HUT [172]; percentage maximum drops of mean CBFV (58 ± 14%) in MCA were much larger than the decreases in systolic (37 ± 23%) and diastolic (32 ± 20%) blood pressures during VVS. In another study, a significant decrease of diastolic CBFV (~ 40%) in MCA of subjects with VVS was observed by Schondorf et al [173]. Apparently, the maximum rCBF drops (76 ± 8%) in microvasculature shown in the present study were larger than the maximum decreases of mean CBFV (58 ± 14%) [172] or diastolic CBFV (~ 40%) [173], suggesting that CBF in small vessels may be more sensitive than CBFV in large vessels for the evaluation of VVS.

Moreover, Joo et al found that CBF in the prefrontal cortex measured by SPECT during HUT was negatively correlated to the total number of syncopal episodes [174],

which had been proven to be the most powerful predictor of a future syncope [175]. Therefore, CBF measurement holds potential to assess the recurrence rate of VVS.

The most important finding in the present study is the threshold of ~50% rCBF decline during HUT, which can be used to completely distinguish controls from presyncope subjects (Figure 5.3). Potentially, real-time continuous monitoring of CBF may provide prognostic information for the occurrence of VVS, i.e., a CBF decrease larger than 50% may result in VVS. Although Njemanze also suggested that a ~50% drop of mean CBFV in MCA was the critical limit to maintain posture tone and consciousness, there were overlaps in their data across the control and VVS groups with this threshold of 50% CBFV decline [172]. Moreover, the time durations from rCBF reaching this threshold to the occurrence of presyncope in the present study were 80 ± 79 seconds (range: 14 to 224 seconds). Given the fact that the syncope occurs about two minutes after presyncope symptoms [168], detection of the early decrease in rCBF to 50% offers a time window of more than 2 minutes for predicting/preventing VVS.

Our study found that rCBF reached the break-point earlier (Figure 5.4) than other measured variables, although the time differences at break-points were not statistically significant. For example, the break-point of rCBF exhibited at 68 ± 82 seconds (range: 3 to 195 seconds) before rMAP. The insignificance may attribute to the small number of subjects and large variations in time differences (i.e., 68 ± 82 seconds). Nevertheless, our findings are consistent with the results documented by Dan et al where the CBFV drops were found to significantly lead the MAP declines by 67 seconds (range: 9 to 197 seconds) [166]. The earlier changes in CBF or CBFV compared to other physiological variables imply that the cerebral hypoperfusion at Stage II after the break-point may be

the primary trigger resulting in rapid changes in other physiological parameters. It is known that the right insular cortex is responsible for regulating sympathetic activities such as blood pressure and heart rate [171, 174, 176]. Reduced CBF in the right insular cortex may possibly suppress sympathetic activities, eventually triggering VVS [174].

As expected, cerebral hypoperfusion (i.e., CBF reduction) occurred during presyncope along with cerebral hypoxia (i.e., $[HbO_2]$ decrease and $[Hb]$ increase). Among all measured cerebral oxygenation parameters, only the minimum values of $r[HbO_2]$ during HUT exhibited significant differences between the control and presyncope groups ($86 \pm 13\%$ versus $64 \pm 12\%$, p = 0.020, see Figure 5.3). This may be due to the relatively larger changes in $[HbO_2]$ (compared to $[Hb]$ and THC) during VVS observed in our study and from previous investigations [152, 168]. In addition, due to the relatively smaller changes in $r[HbO_2]$, $r[Hb]$ and rTHC compared to other measured variables (i.e., rMAP and rCBF) their break-points were not always clear during presyncope (Figure 5.2a). This led to large variations in time differences between cerebral oxygenation variables and MAP determined at the break-points (Figure 5.4), and possibly resulted in evaluation errors.

5.5 Conclusions

This study focuses on testing the feasibility of the novel dual-wavelength DCS flow-oximeter in detecting physiological responses during VVS. All measured physiological parameters were fairly stable during HUT in control subjects without presyncope. By contrast, subjects with presyncope exhibited two stage responses: slow and gradual changes at Stage I before the break-points and rapid and dramatic changes at

Stage II after the break-points. Among all measured variables, rCBF had the largest decrease and reached the break-point at earliest time at Stage II, implying the best sensitivity of rCBF for the evaluation of VVS. Most importantly, a threshold of ~50% rCBF decrease determined from this study can be potentially used to predict the occurrence of VVS. Ultimately, such information may be used to warn subjects at high risk for the recurrence of VVS, or even avoid VVS via an automatic feedback (e.g., an anti-gravity suit used for an Air Force pilot) for keeping cerebral hemodynamics in a normal level.

CHAPTER 6 STUDY SUMMARY, LIMITATIONS, AND FUTURE
PERSPECTIVES

6.1 Study Summary

In this dissertation, I described the development of various NIR diffuse optical instruments for cerebral hemodynamic measurements including a fast DCS flowmeter with an autocorrelator working in burst mode, an upgraded hybrid NIRS/DCS device integrating a commercial tissue-oximeter (Imagent) and a custom-made DCS flowmeter, and a custom-designed dual-wavelength DCS flow-oximeter. I also reported clinical applications of these techniques in quantification of cerebral hemodynamics and CA. More specifically, I explored to evaluate dynamic CAs in both time-domain and frequency-domain via simultaneous measurements of CBF, cerebral oxygenation, and MAP. The results reported in this dissertation have been presented in local/regional/national/international conferences and some of them have been published or submitted to peer-reviewed journals [25, 113, 177] (see attached CV).

My major contributions in these studies include the following aspects. I have designed, constructed, and tested an upgraded new generation hybrid NIRS/DCS device (Chapter 2), which can measure CBF and cerebral oxygenation simultaneously, providing critical information for evaluation of cerebral hemodynamics and CA. In the upgraded hybrid device, I adopted a new autocorrelator board working in burst mode, which dramatically increased DCS sampling rate. High sampling rate is necessary to capture instantaneous changes in cerebral hemodynamics (e.g., LFO signals) for evaluation of dynamic CA. I wrote the control program for the upgraded hybrid NIRS/DCS instrument

using Microsoft Visual Basic, which automatically controlled data collection and storage as well as the communication between the two devices. ABP waveform outputs from the finger plethysmograph were also recorded by our instrument (Chapter 4). I have also participated in the development of a novel portable dual-wavelength DCS flow-oximeter which can simultaneously measure relative changes of CBF and cerebral oxygenation (Chapter 2). I also designed several detector fiber bundles for spatially averaging DCS signals, which significantly improved the SNR of DCS measurements (Chapters 4 and 5).

In terms of clinical studies, I recruited research subjects, designed experimental protocols, implemented data collections, and created the methods for data analysis (Chapters 3, 4 and 5). The general methods of data analysis in these studies were implemented in Matlab (Chapters 3, 4, and 5). In Chapter 3, I reported our first attempt to evaluate dynamic CA in cerebral microvasculature in patients with OSA. In Chapter 4, I reported the first successful detection of LFOs in both CBF and cerebral oxygenation. In this study, I have determined the best hemodynamic parameters (i.e., CBF, $[HbO_2]$ and THC) among our measured variables and optimal physiological condition (HUT) in detecting LFOs for the quantification of LFO phase shifts. We expected that direct and simultaneous measurements of LFOs in CBF and cerebral oxygenation will bring new insights about CA mechanisms and pathologies of cerebral diseases. In Chapter 5, I reported, *for the first time*, the simultaneous monitoring of CBF and cerebral oxygenation during VVS. Our results suggest that CBF has the best sensitivity for the assessment of VVS and is likely the final trigger of VVS. Most importantly, a threshold of ~50% rCBF decline is determined which can completely separate the subjects with or without presyncope, suggesting its potential for predicting VVS.

6.2 Study Limitations and Future Perspectives

Technical limitations and improvements. The uses of 2.5 cm S-D separation in the present studies for DCS measurements [38, 50, 63, 64, 148] (Chapters 3, 4, and 5) and 3 cm S-D separation for NIRS measurements (Chapter 4) have been demonstrated previously in various human studies. Also, Monte Carlo simulations of NIR light paths in human brain have shown that the 2.5 cm and 3 cm S-D separations are sufficient to detect tissue hemodynamics in prefrontal cortex [178]. However, there are always some contributions to the cortex signals from the overlaying tissues (e.g., skin and skull), i.e., the partial volume effect [112, 179]. In the future, multiple S-D separations and multi-layer theoretical models [180] should be used to precisely quantify cerebral hemodynamics.

The ~2 Hz sampling rate by adopting the burst mode and the spatial averaging method used in our study provided adequate SNRs to capture fast dynamic changes in cerebral hemodynamics. However, a faster sampling rate is always appealing as it can reduce measurement errors in detection of rapid hemodynamic changes (e.g., after an autoregulation stimulus and during VVS) as well as diminish the low frequency alias (e.g., cardiac frequency at ~ 1Hz), which may contaminate LFO signals. Several methods may be attempted in the future to improve data acquisition rate while maintain SNRs including using a faster autocorrelator, spatial averaging signals from more detection channels, and adopting few-mode fibers to replace the currently used single-mode fibers [108].

Currently, The DCS/NIRS instruments need off-line data analysis. Online and continuous reporting of hemodynamic results is critical for clinical applications. For example, the predication and prevention of VVS should be done in real time. In addition, current control software requires manual inputs of instrument configuration for different experiments, which is difficult for beginners. An easy-to-use control panel should be developed to enable automatic loading of instrument settings for different applications.

Experimental/clinical limitations and improvements. Physiological manipulations used in our studies either created relatively small hemodynamic variations (i.e., bilateral thigh pressure cuff occlusion) or may result in VVS (i.e., HUT). Other manipulations should be explored in the future to create relative large cerebral hemodynamic perturbations without causing syncope.

Although we used both TD and FD methods to quantify dynamic CA, the sensitivities of the two methods in evaluating CA have not been directly compared yet. Future study will assess both TD and FD dynamic CAs in the same subject population to evaluate and optimize the approaches for the assessment of dynamic CA.

CBF is also sensitive to changes in arterial carbon dioxide (CO_2) content via changes in respiration. Therefore, investigation of cerebral hemodynamics and CA should also include the assessment of CO_2 levels (e.g., End Tidal CO_2) and respiratory rate [181], which will be the subject of future work.

The numbers of subjects reported in this dissertation are small. More subjects will be recruited to improve the statistic power of our study. Future study should also include more patient populations (e.g., stroke, carotid artery stenosis, orthostatic hypotension) to test the capability of our novel techniques in diagnosis of cerebral vascular diseases.

It is expected that with further technical development/improvement and more clinical applications in large patient populations, the NIRS/DCS techniques described in this dissertation might emerge as important tools for the diagnosis of cerebral vascular diseases and management of therapies at the bedside of clinic.

APPENDIX: GLOSSARY

SYMBOLS

α Ratio of Dynamic to Static Scatterers (0 - 1)

ac   Modulated Light Amplitude

C   Hemoglobin Concentration of Whole Blood

γ Percentage of Blood Volume Contained in the Venous Compartment

D   Photon Diffusion Constant

D_b Effective Diffusion Coefficient

DC   Average Light Intensity

AC   Peak-to-peak Light Intensity

g_1 Normalized Electric Field Temporal Autocorrelation Function

G_1 Unnormalized Electric Field Temporal Autocorrelation Function

g_2 Normalized Intensity Temporal Autocorrelation Function

I   Intensity

k_0 Wavevector of Photons in Medium ($k0 = 2\pi / \lambda$

λ Wavelength

n   Ratio of Sample and Air Index of Refraction

φ Phase Shift Between the Detected and Source NIR Light

r   Position Vector

ρ Source-detector Separation

$<\Delta r^2(\tau)>$ Mean square displacement q D S τ

S_{AC} Slope of ρ vs. AC component light intensity Curve

S_{DC} Slope of ρ vs. DC component light intensity Curve

$S\varphi$	Slope of ρ vs. Phase shift Curve
S_0	Source-light Distribution
τ	Correlation Function Decay Time
μ_a	Absorption Coefficient
$\mu_s{}'$	Reduced Scattering Coefficient
v	Speed of Light in Medium
ω	Angular Frequency of Modulation

TERMS

[Hb]	deoxygenated hemoglobin concentration (unit μM)
[HbO_2]	oxygenated hemoglobin concentration (unit μM)
Δ[Hb]	deoxygenated hemoglobin concentration change (unit μM)
Δ[HbO_2]	oxygenated hemoglobin concentration change (unit μM)
ΔTHC	total hemoglobin concentration change (unit μM)
r[Hb]	relative deoxygenated hemoglobin concentration change (unit %)
r[HbO_2]	relative oxygenated hemoglobin concentration change (unit %)
rCBF	relative cerebral blood flow change (unit %)
rMAP	relative mean arterial pressure change (unit %)
rTHC	relative total hemoglobin concentration (unit %)
ABP	Arterial Blood Pressure
APD	Avalanche Photodiode
ASL-MRI	Arterial Spin-Labeled Magnetic Resonance Imaging (Perfusion MRI)
BFI	Blood Flow Index (αD_B)

BOLD-MRI	Blood Oxygen Level Dependent Magnetic Resonance Imaging
BPM	Beat per Minute
CA	Cerebral autoregulation
CBF	Cerebral Blood Flow
Coh	Coherence
CW	Continuous Wave
CT	Computed Tomography
DCS	Diffuse Correlation Spectroscopy
DAP	Diastolic Arterial Pressure
DLS	Dynamic Light Scattering
DWS	Diffusing Wave Spectroscopy
$EtCO_2$	End-tidal CO_2
FD	Frequency-Domain
Hb	Deoxy-hemoglobin
HbO_2	Oxy-hemoglobin
HUT	Head-up Tilting
LFO	Low Frequency Oscillation
MAP	Mean Arterial Blood Pressure
MCA	Middle Cerebral Artery
NIR	Near-Infrared
NIRS	Near-Infrared Spectroscopy
OSA	Obstructive Sleep Apnea
PET	Positron Emission Tomography

PMT Photomultiplier Tube

PSD Power Spectrum Density

SBP Systolic Blood Pressure

SNR Signal to Noise Ratio

S_tO_2 Tissue Blood Oxygen Saturation

TCD Transcranial Doppler

TD Time-Domain

TFA Transfer Function Analysis

THC Total Hemoglobin Concentration

VVS Vasovagal Syncope

REFERENCES

[1] Mohrman, D.E. and L.J. Heller, *Cardiovascular Physiology*. 6 ed2006, New York, NY: McGraw-Hill Medical. 1-4.

[2] Paulson, O.B., S. Strandgaard, and L. Edvinsson, *Cerebral Autoregulation.* Cerebrovascular and Brain Metabolism Reviews, 1990. **2**(2): p. 161-192.

[3] Chillon, J.-M. and G. Baumbach, *Autoregulation: arterial and intracranial pressure*, in *Cerebral blood flow and metabolism*, L. Edvinsson and K. DN, Editors. 2002, Lippincott Williams & Wilkins: Philadelphia. p. 395-412.

[4] Roger, V.L., et al., *Heart disease and stroke statistics--2012 update: a report from the American Heart Association.* Circulation, 2012. **125**(1): p. e2-e220.

[5] del Zoppo, G.J., R. Von Kummer, and G.F. Hamann, *Ischaemic damage of brain microvessels: inherent risks for thrombolytic treatment in stroke.* Journal of Neurology Neurosurgery and Psychiatry, 1998. **65**(1): p. 1-9.

[6] Durduran, T., et al., *Transcranial optical monitoring of cerebrovascular hemodynamics in acute stroke patients.* Opt Express, 2009. **17**(5): p. 3884-902.

[7] Reinhard, M., et al., *Oscillatory cerebral hemodynamics - the macro- vs. microvascular level.* Journal of the Neurological Sciences, 2006. **250**(1-2): p. 103-109.

[8] Hu, H.H., et al., *Transfer function analysis of cerebral hemodynamics in patients with carotid stenosis.* Journal of Cerebral Blood Flow and Metabolism, 1999. **19**(4): p. 460-465.

[9] Somers, V.K., et al., *Sleep apnea and cardiovascular disease - An American Heart Association/American College of Cardiology Foundation Scientific Statement from the American Heart Association Council for High Blood Pressure Research Professional Education Committee, Council on Clinical Cardiology, Stroke Council, and Council on Cardiovascular Nursing.* Circulation, 2008. **118**(10): p. 1080-1111.

[10] Khayat, R., B. Patt, and D. Hayes, *Obstructive sleep apnea: the new cardiovascular disease. Part I: obstructive sleep apnea and the pathogenesis of vascular disease.* Heart Failure Reviews, 2009. **14**(3): p. 143-153.

[11] Yaggi, H.K., et al., *Obstructive Sleep Apnea as a Risk Factor for Stroke and Death.* New England Journal of Medicine, 2005. **353**(19): p. 2034-2041.

[12] Canessa, N., et al., *Obstructive sleep apnea: brain structural changes and neurocognitive function before and after treatment.* Am J Respir Crit Care Med, 2011. **183**(10): p. 1419-26.

[13] Urbano, F., et al., *Impaired cerebral autoregulation in obstructive sleep apnea.* Journal of Applied Physiology, 2008. **105**(6): p. 1852-1857.

[14] van Lieshout, J.J., et al., *Syncope, cerebral perfusion, and oxygenation.* Journal of Applied Physiology, 2003. **94**(3): p. 833-848.

[15] Kapoor, W.N., *Evaluation and Outcome of Patients with Syncope.* Medicine, 1990. **69**(3): p. 160-175.

[16] Kenny, R.A., et al., *Head-up Tilt - a Useful Test for Investigating Unexplained Syncope.* Lancet, 1986. **1**(8494): p. 1352-1355.

[17] Furlan, R., et al., *Cardiac autonomic patterns preceding occasional vasovagal reactions in healthy humans.* Circulation, 1998. **98**(17): p. 1756-1761.

[18]   Panerai, R.B., *Cerebral autoregulation: From models to clinical applications.* Cardiovascular Engineering, 2008. **8**(1): p. 42-59.

[19]   van Beek, A.H., et al., *Cerebral autoregulation: an overview of current concepts and methodology with special focus on the elderly.* J Cereb Blood Flow Metab, 2008. **28**(6): p. 1071-85.

[20]   Lassen, N.A., *Cerebral Blood Flow and Oxygen Consumption in Man.* Physiological Reviews, 1959. **39**(2): p. 183-238.

[21]   Obrist, W.D., et al., *Regional Cerebral Blood-Flow Estimated by Xenon-133 Inhalation.* Stroke, 1975. **6**(3): p. 245-256.

[22]   Panerai, R.B., *Assessment of cerebral pressure autoregulation in humans - a review of measurement methods.* Physiological Measurement, 1998. **19**(3): p. 305-338.

[23]   Aaslid, R., et al., *Assessment of Cerebral Autoregulation Dynamics from Simultaneous Arterial and Venous Transcranial Doppler Recordings in Humans.* Stroke, 1991. **22**(9): p. 1148-1154.

[24]   Zhang, R., et al., *Transfer function analysis of dynamic cerebral autoregulation in humans.* American Journal of Physiology-Heart and Circulatory Physiology, 1998. **43**(1): p. H233-H241.

[25]   Cheng, R., et al., *Noninvasive optical evaluation of spontaneous low frequency oscillations in cerebral hemodynamics.* Neuroimage, 2012. **62**(3): p. 1445-1454.

[26]   Diehl, R.R., et al., *Phase Relationship between Cerebral Blood-Flow Velocity and Blood-Pressure - a Clinical-Test of Autoregulation.* Stroke, 1995. **26**(10): p. 1801-1804.

[27]   Morita, Y., J.E. Hardebo, and E. Bouskela, *Influence of Cerebrovascular Sympathetic, Parasympathetic, and Sensory Nerves on Autoregulation and Spontaneous Vasomotion.* Acta Physiologica Scandinavica, 1995. **154**(2): p. 121-130.

[28]   Vern, B.A., et al., *Low-frequency oscillations of cortical oxidative metabolism in waking and sleep.* J Cereb Blood Flow Metab, 1988. **8**(2): p. 215-26.

[29]   Auer, D.P., *Spontaneous low-frequency blood oxygenation level-dependent fluctuations and functional connectivity analysis of the 'resting' brain.* Magn Reson Imaging, 2008. **26**(7): p. 1055-64.

[30]   Edlow, B.L., et al., *The effect of healthy aging on cerebral and systemic hemodynamic responses to posture change*, in *Brain 09*2009, International Society of Cerebral Blood Flow and Metabolism: Chicago.

[31]   Markus, H.S., *Transcranial Doppler ultrasound.* British Medical Bulletin, 2000. **56**(2): p. 378-388.

[32]   Latchaw, R.E., et al., *Guidelines and recommendations for perfusion imaging in cerebral ischemia: A scientific statement for healthcare professionals by the writing group on perfusion imaging, from the Council on Cardiovascular Radiology of the American Heart Association.* Stroke, 2003. **34**(4): p. 1084-1104.

[33]   Wintermark, M., et al., *Using 80 kVp versus 120 kVp in perfusion CT measurement of regional cerebral blood flow.* American Journal of Neuroradiology, 2000. **21**(10): p. 1881-1884.

[34]   Mahagne, M.H., et al., *Voxel-based mapping of cortical ischemic damage using Tc 99m L,L-ethyl cysteinate dimer SPECT in acute stroke.* 2004. **14**(1): p. 23-32.

[35]   Baron, J.C., *Mapping the ischaemic penumbra with PET: implications for acute stroke treatment.* 1999. **9**(4): p. 193-201.

[36]   Detre, J.A., et al., *Perfusion Imaging.* Magnetic Resonance in Medicine, 1992. **23**(1): p. 37-45.

[37]   Kidwell, C.S., J.R. Alger, and J.L. Saver, *Beyond mismatch: evolving paradigms in imaging the ischemic penumbra with multimodal magnetic resonance imaging.* Stroke, 2003. **34**: p. 2729-2735.

[38]   Edlow, B.L., et al., *The effects of healthy aging on cerebral hemodynamic responses to posture change.* Physiological Measurement, 2010. **31**(4): p. 477-495.

[39]   Bosomtwi, A., et al., *Quantitative evaluation of microvascular density after stroke in rats using MRI.* Journal of Cerebral Blood Flow and Metabolism, 2008. **28**(12): p. 1978-1987.

[40]   Brown, W.R. and C.R. Thore, *Cerebral microvascular pathology in ageing and neurodegeneration.* Neuropathology and Applied Neurobiology, 2011. **37**(1): p. 56-74.

[41]   Marinoni, M., et al., *Technical limits in transcranial Doppler recording: inadequate acoustic windows.* Ultrasound in Medicine and Biology, 1997. **23**(8): p. 1275-7.

[42]   Haacke, E.M., et al., *In vivo measurement of blood oxygen saturation using magnetic resonance imaging: A direct validation of the blood oxygen level-dependent concept in functional brain imaging.* Human Brain Mapping, 1997. **5**(5): p. 341-346.

[43]   Kleinschmidt, A., et al., *Simultaneous recording of cerebral blood oxygenation changes during human brain activation by magnetic resonance imaging and near-infrared spectroscopy.* J. Cereb. Blood Flow Metab., 1996. **16**(5): p. 817-826.

[44]   Villringer, K., et al., *Assessment of local brain activation. A simultaneous PET and near-infrared spectroscopy study.* Adv Exp Med Biol, 1997. **413**: p. 149-53.

[45]   Huppert, T.J., et al., *A temporal comparison of BOLD, ASL, and NIRS hemodynamic responses to motor stimuli in adult humans.* Neuroimage, 2006. **29**(2): p. 368-82.

[46]   Wang, J., et al., *Arterial spin labeling perfusion fMRI with very low task frequency.* Magnetic Resonance in Medicine, 2003. **49**(5): p. 796-802.

[47]   Boas, D.A., Gaudette, T.J., and Arridge, S.R., *Simultaneous imaging and optode calibration with diffuse optical tomography.* Optics Express, 2001. **8**: p. 263-270.

[48]   Cooper, R.J., et al., *Transient haemodynamic events in neurologically compromised infants: A simultaneous EEG and diffuse optical imaging study.* Neuroimage, 2011. **55**(4): p. 1610-1616.

[49]   De Blasi, R.A., et al., *Cerebral and muscle oxygen saturation measurement by frequency-domain near-infra-red spectrometer.* Med Biol Eng Comput, 1995. **33**(2): p. 228-30.

[50]   Sassaroli, A., et al., *Phase Difference between Low-Frequency Oscillations of Cerebral Deoxy- and Oxy-Hemoglobin Concentrations during a Mental Task.* J Innov Opt Health Sci, 2011. **4**(2): p. 151-158.

[51]   Zwart, A., et al., *Multicomponent analysis of hemoglobin derivatives with reversed-optics spectrophotometer.* Clin Chem, 1984. **30**(3): p. 373-9.

[52] Prahl, S. *Optical Absorption of Hemoglobin*. Available from: http://omlc.ogi.edu/spectra/hemoglobin/.

[53] Ferrari, M., M. Muthalib, and V. Quaresima, *The use of near-infrared spectroscopy in understanding skeletal muscle physiology: recent developments.* Philos Trans A Math Phys Eng Sci, 2011. **369**(1955): p. 4577-90.

[54] Liebert, A., et al., *Time-Resolved Multidistance Near-Infrared Spectroscopy of the Adult Head: Intracerebral and Extracerebral Absorption Changes from Moments of Distribution of Times of Flight of Photons.* Appl. Opt., 2004. **43**(15): p. 3037-3047.

[55] Siegel, A.M., Marota, J.A., and Boas, D.A., *Design and evaluation of a continuous-wave diffuse optical tomography system.* Optics Express, 1999. **4**: p. 287-298.

[56] Arridge, S.R. and W.R.B. Lionheart, *Nonuniqueness in diffusion-based optical tomography.* Opt Lett, 1998. **23**(11): p. 882-884.

[57] Cheung, C., et al., *In vivo cerebrovascular measurement combining diffuse near-infrared absorption and correlation spectroscopies.* Physics in Medicine and Biology, 2001. **46**(8): p. 2053-2065.

[58] Culver, J.P., et al., *Evidence that cerebral blood volume can provide brain activation maps with better spatial resolution than deoxygenated hemoglobin.* Neuroimage, 2005. **27**(4): p. 947-59.

[59] Dietsche, G., et al., *Fiber-based multispeckle detection for time-resolved diffusing-wave spectroscopy: characterization and application to blood flow detection in deep tissue.* Appl Opt, 2007. **46**(35): p. 8506-14.

[60] Durduran, T., et al., *Optical measurement of cerebral hemodynamics and oxygen metabolism in neonates with congenital heart defects.* Journal of Biomedical Optics, 2010. **15**(3): p. -.

[61] Gagnon, L., et al., *Investigation of diffuse correlation spectroscopy in multi-layered media including the human head.* Optics Express, 2008. **16**(20): p. 15514-15530.

[62] Li, J., et al., *Transient functional blood flow change in the human brain measured noninvasively by diffusing-wave spectroscopy.* Opt Lett, 2008. **33**(19): p. 2233-5.

[63] Shang, Y., et al., *Cerebral monitoring during carotid endarterectomy using near-infrared diffuse optical spectroscopies and electroencephalogram.* Phys Med Biol, 2011. **56**(10): p. 3015-32.

[64] Zirak, P., et al., *Effects of acetazolamide on the micro- and macro-vascular cerebral hemodynamics: a diffuse optical and transcranial doppler ultrasound study.* Biomed Opt Express, 2010. **1**(5): p. 1443-1459.

[65] Buckley, E.M., et al., *Cerebral hemodynamics in preterm infants during positional intervention measured with diffuse correlation spectroscopy and transcranial Doppler ultrasound.* Optics Express, 2009. **17**(15): p. 12571-12581.

[66] Roche-Labarbe, N., et al., *Noninvasive optical measures of CBV, StO(2), CBF index, and rCMRO(2) in human premature neonates' brains in the first six weeks of life.* Hum Brain Mapp, 2010. **31**(3): p. 341-52.

[67] Yu, G., et al., *Noninvasive monitoring of murine tumor blood flow during and after photodynamic therapy provides early assessment of therapeutic efficacy.* Clinical Cancer Research, 2005. **11**(9): p. 3543-3552.

[68]   Durduran, T., et al., *Spatiotemporal quantification of cerebral blood flow during functional activation in rat somatosensory cortex using laser-speckle flowmetry.* J Cereb Blood Flow Metab, 2004. **24**(5): p. 518-25.

[69]   Shang, Y., et al., *Diffuse optical monitoring of repeated cerebral ischemia in mice.* Opt Express, 2011. **19**(21): p. 20301-20315.

[70]   Zhou, C., et al., *Diffuse Optical Monitoring of Hemodynamic Changes in Piglet Brain with Closed Head Injury.* Journal of Biomedical Optics, 2009. **14**(034015).

[71]   Durduran, T., et al., *Diffuse optical measurement of blood flow, blood oxygenation, and metabolism in a human brain during sensorimotor cortex activation.* Opt Lett, 2004. **29**(15): p. 1766-8.

[72]   Yu, G., et al., *Validation of diffuse correlation spectroscopy for muscle blood flow with concurrent arterial spin labeled perfusion MRI.* Optics Express, 2007. **15**(3): p. 1064-1075

[73]   Kim, M.N., et al., *Noninvasive measurement of cerebral blood flow and blood oxygenation using near-infrared and diffuse correlation spectroscopies in critically brain-injured adults.* Neurocrit Care, 2010. **12**(2): p. 173-80.

[74]   Pantoni, L., *Cerebral small vessel disease: from pathogenesis and clinical characteristics to therapeutic challenges.* Lancet Neurol, 2010. **9**(7): p. 689-701.

[75]   Macey, P.M., et al., *Brain morphology associated with obstructive sleep apnea.* Am J Respir Crit Care Med, 2002. **166**(10): p. 1382-7.

[76]   Fantini, S., M.A. Franceschini, and E. Gratton, *Semi-Infinite-Geometry Boundary-Problem for Light Migration in Highly Scattering Media - a Frequency-Domain Study in the Diffusion-Approximation.* Journal of the Optical Society of America B-Optical Physics, 1994. **11**(10): p. 2128-2138.

[77]   Shang, Y., et al., *Portable optical tissue flow oximeter based on diffuse correlation spectroscopy.* Optics Letters, 2009. **34**(20): p. 3556-3558.

[78]   Chance, B. and R. Alfano. *Proceedings of Optical Tomography, Photon Migration, and Spectroscopy of Tissue and Model Media: Theory, Human Studies, and Instrumentation*. 1995. SPIE.

[79]   Yodh, A. and B. Chance, *Spectroscopy and Imaging with Diffusing Light.* Physics Today, 1995. **48**(3): p. 34-40.

[80]   Fantini, S., Franceschini, M.A., Maier, J.S., Walker, S., and Gratton, E., *Frequency domain multi-source optical spectrometer and oximeter.* Proc. SPIE, 1994. **2326**: p. 108-116.

[81]   Irwin, D., et al., *Influences of tissue absorption and scattering on diffuse correlation spectroscopy blood flow measurements.* Biomed Opt Express, 2011. **2**(7): p. 1969-85.

[82]   Boas, D.A. and A.G. Yodh, *Spatially varying dynamical properties of turbid media probed with diffusing temporal light correlation.* Journal of the Optical Society of America A-Optics Image Science and Vision, 1997. **14**(1): p. 192-215.

[83]   Boas, D.A., L.E. Campbell, and A.G. Yodh, *Scattering and Imaging with Diffusing Temporal Field Correlations.* Physical Review Letters, 1995. **75**(9): p. 1855-1858.

[84]   Boas, D., *Diffuse Photon Probes of Structural and Dynamical Properties of Turbid Media: Theory and Biomedical Applications*, in *Physics*1996, University of Pennsylvania, Dissertation: Philadelphia. p. 244.

[85]   Delpy, D.T., et al., *Estimation of optical pathlength through tissue from direct time of flight measurement.* Phys Med Biol, 1988. **33**: p. 1433-1442.

[86]   Curcio, J.A. and C.C. Petty, *The Near Infrared Absorption Spectrum of Liquid Water.* J. Opt. Soc. Am., 1951. **41**(5): p. 302-302.

[87]   Duncan, A., et al., *Optical pathlength measurements on adult head, calf and forearm and the head of the newborn infant using phase resolved optical spectroscopy.* Phys Med Biol, 1995. **40**(2): p. 295-304.

[88]   Yodh, A.G. and D.A. Boas, *Functional Imaging with Diffusing Light*, in *Biomedical Photonics*2003, CRC Press. p. 21-1.

[89]   Furutsu, K., *On the diffusion equation derived from the space-time transport equation.* J. Opt. Soc. Am. A, 1980. **70**: p. 360.

[90]   Patterson, M.S., B. Chance, and B.C. Wilson, *Time Resolved Reflectance and Transmittance for the Noninvasive Measurement of Tissue Optical-Properties.* Appl Opt, 1989. **28**(12): p. 2331-2336.

[91]   Aronson, R., *Boundary conditions for diffusion of light.* J.Opt.Soc.of Am.A, 1995. **12**: p. 2532-2539.

[92]   Haskell, R.C., et al., *Boundary conditions for the diffusion equation in radiative transfer.* J.Opt.Soc.of Am.A, 1994. **11**: p. 2727-2741.

[93]   Pine, D.J., et al., *Diffusing-wave spectroscopy: Dynamic light scattering in the multiple scattering limit.* J.Phys.France, 1990. **51**: p. 2101-2127.

[94]   Hueber, D.M., et al., *New optical probe designs for absolute (self-calibrating) NIR tissue hemoglobin measurements.* 1999: p. 618-631.

[95]   Pine, D.J., et al., *Diffusing-Wave Spectroscopy.* Physical Review Letters, 1988. **60**(12): p. 1134-1137.

[96]   Maret, G. and P.E. Wolf, *Multiple light scattering from disordered media. The effect of brownian motion of scatterers.* Z. Phys. B., 1987. **65**: p. 409-413.

[97]   Ackerson, B.J., Pusey, P.N., *Shear-induced order in suspensions of hard-spheres.* Phys. Rev. Lett., 1988. **61**: p. 1033-1036.

[98]   Ackerson, B.J., et al., *Correlation transfer: Application of radiative transfer solution methods to photon correlation problems.* J.Thermophys.and Heat Trans., 1992. **6**: p. 577-588.

[99]   Rice, S.O., *Mathematical analysis of random noise*, in *Noise and Stochastic Processes*, N. Wax, Editor 1954, Dover: New York. p. 133.

[100]   Einstein, A., *On the Motion of Small Particles Suspended in Liquids at Rest Required by the Molecular-Kinetic Theory of Heat.* Annalen der Physik, 1905. **17**: p. 549-560.

[101]   Menon, C., et al., *An integrated approach to measuring tumor oxygen status using human melanoma xenografts as a model.* Cancer Research, 2003. **63**(21): p. 7232-7240.

[102]   Yu, G., et al., *Noninvasive monitoring of murine tumor blood flow during and after photodynamic therapy provides early assessment of therapeutic efficacy.* Clin Cancer Res, 2005. **11**(9): p. 3543-52.

[103]   Munk, N., et al., *Noninvasively measuring the hemodynamic effects of massage on skeletal muscle: A novel hybrid near-infrared diffuse optical instrument.* J Bodyw Mov Ther, 2012. **16**(1): p. 22-8.

[104] Shang, Y., et al., *Noninvasive optical characterization of muscle blood flow, oxygenation, and metabolism in women with fibromyalgia.* Arthritis Research & Therapy, 2012. **14**(6).

[105] Shang, Y., et al., *Effects of muscle fiber motion on diffuse correlation spectroscopy blood flow measurements during exercise.* Biomed Opt Express, 2010. **1**(2): p. 500-511.

[106] Yu, G., et al., *Intraoperative evaluation of revascularization effect on ischemic muscle hemodynamics using near-infrared diffuse optical spectroscopies.* J Biomed Opt, 2011. **16**(2): p. 027004.

[107] Dong, L., et al., *Noninvasive diffuse optical monitoring of head and neck tumor blood flow and oxygenation during radiation delivery.* Biomedical Optics Express, 2012. **3**(2): p. 259-272.

[108] Li, J., et al., *Noninvasive detection of functional brain activity with near-infrared diffusing-wave spectroscopy.* Journal of Biomedical Optics, 2005. **10**(4): p. 044002-1-12.

[109] Sunar, U., et al., *Noninvasive diffuse optical measurement of blood flow and blood oxygenation for monitoring radiation therapy in patients with head and neck tumors: a pilot study.* J Biomed Opt, 2006. **11**(6): p. 064021.

[110] Yu, G., et al., *Time-dependent blood flow and oxygenation in human skeletal muscles measured with noninvasive near-infrared diffuse optical spectroscopies.* J Biomed Opt, 2005. **10**(2): p. 024027.

[111] Cheng, R., et al., *Noninvasive quantification of skeletal muscle microvasculature blood flow in mouse thigh by diffuse correlation spectroscopy.* Applied Optics (submitted), 2013.

[112] Durduran, T., *Non-Invasive Measurements of Tissue Hemodynamics with Hybrid Diffuse Optical Methods*, 2004, University of Pennsylvania.

[113] Cheng, R., et al. *Noninvasive Optical Evaluation of Cerebral Autoregulation in Patients with Obstructive Sleep Apnea.* 2010. Optical Society of America.

[114] Gurley, K., Y. Shang, and G. Yu, *Noninvasive optical quantification of absolute blood flow, blood oxygenation, and oxygen consumption rate in exercising skeletal muscle (vol 17, 075010, 2012).* J Biomed Opt, 2012. **17**(7).

[115] Buckley, E.M., et al., *Validation of diffuse correlation spectroscopic measurement of cerebral blood flow using phase-encoded velocity mapping magnetic resonance imaging.* J Biomed Opt, 2012. **17**(3): p. 037007-1.

[116] Li, X., *Fluorescence and diffusive wave diffraction tomographic probes in turbid media*, in *Physics & Astronomy*1998, University of Pennsylvania, Dissertation: Philadelphia.

[117] Pogue, B.W. and M.S. Patterson, *Frequency-domain optical absorption spectroscopy of finite tissue volumes using diffusion theory.* Phys Med Biol, 1994. **39**(7): p. 1157-80.

[118] Wolf, R.L., et al., *Optical coherent backscattering by random media: An experimental study.* J. Phys. France, 1988. **49**: p. 60-75.

[119] Middleton, A.A. and D.S. Fisher, *Discrete scatterers and autocorrelations of multiply scattered light.* Phys.Rev.B, 1991. **43**: p. 5934-5938.

[120] Pine, D.J., et al., *Diffusing-wave spectroscopy.* Phys.Rev.Lett., 1988. **60**: p. 1134-1137.

[121] MacKintosh, F.C. and S. John, *Diffusing-wave spectroscopy and multiple scattering of light in correlated random media.* Phys.Rev.B, 1989. **40**: p. 2382-2406.

[122] Zhou, C., *In-vivo Optical Imaging and Spectroscopy of Cerebral Hemodynamics*, 2007, University of Pennsylvania.

[123] Benaron, D.A. and D.K. Stevenson, *Optical time-of-flight and absorbance imaging of biologic media.* Science, 1993. **259**(5100): p. 1463-6.

[124] Jacques, S.L., *Time-resolved reflectance spectroscopy in turbid tissues.* IEEE Transactions on Biomedical Engineering, 1989. **36**: p. 1155-1161.

[125] Patterson, M.S., B. Chance, and B.C. Wilson, *Time resolved reflectance and transmittance for the non-invasive measurement of tissue optical properties.* Applied Optics, 1989. **28**: p. 2331-2336.

[126] Yodh, A.G., P.D. Kaplan, and D.J. Pine, *Pulsed diffusing-wave spectroscopy: High resolution through nonlinear optical gating.* Phys.Rev.B, 1990. **42**: p. 4744-4747.

[127] Bålfors, E.M. and K.A. Franklin, *Impairment of cerebral perfusion during obstructive sleep apneas.* Am J Respir Crit Care Med, 1994. **150**(6): p. 1587-1591.

[128] Hajak, G., et al., *Sleep apnea syndrome and cerebral hemodynamics.* Chest, 1996. **110**(3): p. 670-9.

[129] Siebler, M., et al., *Cerebral blood flow velocity alterations during obstructive sleep apnea syndrome.* Neurology, 1990. **40**(9): p. 1461-2.

[130] Siebler, M. and A. Nachtmann, *Cerebral hemodynamics in obstructive sleep apnea.* Chest, 1993. **103**(4): p. 1118-9.

[131] Nasr, N., et al., *Cerebral autoregulation in patients with obstructive sleep apnea syndrome during wakefulness.* Eur J Neurol, 2009. **16**(3): p. 386-91.

[132] Kamba, M., et al., *Cerebral metabolic impairment in patients with obstructive sleep apnoea: an independent association of obstructive sleep apnoea with white matter change.* Journal of Neurology Neurosurgery and Psychiatry, 2001. **71**(3): p. 334-339.

[133] Carey, B.J., et al., *Cerebral autoregulatory responses to head-up tilt in normal subjects and patients with recurrent vasovagal syncope.* Circulation, 2001. **104**(8): p. 898-902.

[134] Tiecks, F.P., et al., *Evaluation of impaired cerebral autoregulation by the Valsalva maneuver.* Stroke, 1996. **27**(7): p. 1177-82.

[135] Flemons, W.W., et al., *Home diagnosis of sleep apnea: a systematic review of the literature. An evidence review cosponsored by the American Academy of Sleep Medicine, the American College of Chest Physicians, and the American Thoracic Society.* Chest, 2003. **124**(4): p. 1543-79.

[136] Budhiraja, R., S. Parthasarathy, and S.F. Quan, *Endothelial dysfunction in obstructive sleep apnea.* J Clin Sleep Med, 2007. **3**(4): p. 409-15.

[137] Maiorana, A., et al., *Exercise and the nitric oxide vasodilator system.* Sports Medicine, 2003. **33**(14): p. 1013-1035.

[138] Imadojemu, V.A., et al., *Sympathetic chemoreflex responses in obstructive sleep apnea and effects of continuous positive airway pressure therapy.* Chest, 2007. **131**(5): p. 1406-1413.

[139] Ruland, S. and V. Aiyagari, *Cerebral autoregulation and blood pressure lowering.* Hypertension, 2007. **49**(5): p. 977-978.

[140] Mayer, S., *Studien zur Physiologie des Herzens und der Blutgefässe.* Sitzungsberichte Akademie der Wissenschaften, 1876. **74**: p. 281-307.

[141] Bertram, D., et al., *The arterial baroreceptor reflex of the rat exhibits positive feedback properties at the frequency of Mayer waves.* Journal of Physiology-London, 1998. **513**(1): p. 251-261.

[142] Diehl, R.R., et al., *Spontaneous blood pressure oscillations and cerebral autoregulation.* Clin Auton Res, 1998. **8**(1): p. 7-12.

[143] Katura, T., et al., *Quantitative evaluation of interrelations between spontaneous low-frequency oscillations in cerebral hemodynamics and systemic cardiovascular dynamics.* Neuroimage, 2006. **31**(4): p. 1592-1600.

[144] Biswal, B., et al., *Functional Connectivity in the Motor Cortex of Resting Human Brain Using Echo-Planar Mri.* Magnetic Resonance in Medicine, 1995. **34**(4): p. 537-541.

[145] Wang, K., et al., *Altered functional connectivity in early Alzheimer's disease: A resting-state fMRI study.* Hum Brain Mapp, 2007. **28**(10): p. 967-978.

[146] Diehl, R.R., et al., *Cerebrovascular mechanisms in neurocardiogenic syncope with and without postural tachycardia syndrome.* J Auton Nerv Syst, 1999. **76**(2-3): p. 159-66.

[147] Haubrich, C., et al., *Dynamic autoregulation testing in the posterior cerebral artery.* Stroke, 2004. **35**(4): p. 848-852.

[148] Obrig, H., et al., *Spontaneous low frequency oscillations of cerebral hemodynamics and metabolism in human adults.* Neuroimage, 2000. **12**(6): p. 623-39.

[149] Fantini, S., et al., *Non-invasive optical monitoring of the newborn piglet brain using continuous-wave and frequency-domain spectroscopy.* Phys Med Biol, 1999. **44**(6): p. 1543-63.

[150] Reinhard, M., et al., *Transfer function analysis for clinical evaluation of dynamic cerebral autoregulation- a comparison between spontaneous and respiratory-induced oscillations.* Physiological Measurement, 2003. **24**(1): p. 27-43.

[151] Levine, B.D., et al., *Cerebral Versus Systemic Hemodynamic during Graded Orthostatic Stress in Humans.* Circulation, 1994. **90**(1): p. 298-306.

[152] Krakow, K., et al., *Simultaneous assessment of brain tissue oxygenation and cerebral perfusion during orthostatic stress.* European Neurology, 2000. **43**(1): p. 39-46.

[153] van Beek, A.H., et al., *Oscillations in cerebral blood flow and cortical oxygenation in Alzheimer's disease.* Neurobiol Aging, 2011.

[154] Tong, Y. and B.D. Frederick, *Time lag dependent multimodal processing of concurrent fMRI and near-infrared spectroscopy (NIRS) data suggests a global circulatory origin for low-frequency oscillation signals in human brain.* Neuroimage, 2010. **53**(2): p. 553-64.

[155] Mcculloch, J., L. Edvinsson, and P. Watt, *Comparison of the Effects of Potassium and Ph on the Caliber of Cerebral Veins and Arteries.* Pflugers Archiv-European Journal of Physiology, 1982. **393**(1): p. 95-98.

[156] Julien, C., *The enigma of Mayer waves: Facts and models.* Cardiovascular Research, 2006. **70**(1): p. 12-21.

[157] Furlan, R., et al., *Oscillatory patterns in sympathetic neural discharge and cardiovascular variables during orthostatic stimulus.* Circulation, 2000. **101**(8): p. 886-892.

[158] Segal, S.S., *Regulation of blood flow in the microcirculation.* Microcirculation, 2005. **12**(1): p. 33-45.

[159] Wang, S.Q., et al., *Blood pressure regulation in diabetic patients with and without peripheral neuropathy.* American Journal of Physiology-Regulatory Integrative and Comparative Physiology, 2012. **302**(5): p. R541-R550.

[160] Matzen, S., et al., *Blood volume distribution during head-up tilt induced central hypovolaemia in man.* Clinical Physiology, 1991. **11**(5): p. 411-22.

[161] Sander-Jensen, K., et al., *Hypotension Induced by Passive Head-up Tilt - Endocrine and Circulatory Mechanisms.* American Journal of Physiology, 1986. **251**(4): p. R742-R748.

[162] Burke, D., G. Sundlof, and B.G. Wallin, *Postural Effects on Muscle Nerve Sympathetic Activity in Man.* Journal of Physiology-London, 1977. **272**(2): p. 399-414.

[163] Joyner, M.J., J.T. Shepherd, and D.R. Seals, *Sustained Increases in Sympathetic Outflow during Prolonged Lower Body Negative-Pressure in Humans.* Journal of Applied Physiology, 1990. **68**(3): p. 1004-1009.

[164] Schondorf, R., J. Benoit, and T. Wein, *Cerebrovascular and cardiovascular measurements during neurally mediated syncope induced by head-up tilt.* Stroke, 1997. **28**(8): p. 1564-1568.

[165] Colier, W., et al., *Cerebral and circulatory haemodynamics before vasovagal syncope induced by orthostatic stress.* Clinical Physiology, 1997. **17**(1): p. 83-94.

[166] Dan, D., et al., *Cerebral blood flow velocity declines before arterial pressure in patients with orthostatic vasovagal presyncope.* Journal of the American College of Cardiology, 2002. **39**(6): p. 1039-1045.

[167] Madsen, P., et al., *Near-infrared spectrophotometry determined brain oxygenation during fainting.* Acta Physiologica Scandinavica, 1998. **162**(4): p. 501-507.

[168] Szufladowicz, E., et al., *Near-infrared spectroscopy in evaluation of cerebral oxygenation during vasovagal syncope.* Physiological Measurement, 2004. **25**(4): p. 823-836.

[169] Leonelli, F.M., et al., *False positive head-up tilt: Hemodynamic and neurohumoral profile.* Journal of the American College of Cardiology, 2000. **35**(1): p. 188-193.

[170] Gatto, R., et al., *Frequency domain near-infrared spectroscopy technique in the assessment of brain oxygenation: A validation study in live subjects and cadavers.* Journal of Neuroscience Methods, 2006. **157**(2): p. 274-277.

[171] Folino, A.F., *Cerebral autoregulation and syncope.* Progress in Cardiovascular Diseases, 2007. **50**(1): p. 49-80.

[172] Njemanze, P.C., *Critical Limits of Pressure-Flow Relation in the Human Brain.* Stroke, 1992. **23**(12): p. 1743-1747.

[173]   Schondorf, R., J. Benoit, and R. Stein, *Cerebral autoregulation in orthostatic intolerance.* Neuro-Cardiovascular Regulation: From Molecules to Man, 2001. **940**: p. 514-526.

[174]   Joo, E.Y., et al., *Cerebral blood flow abnormalities in patients with neurally mediated syncope.* Journal of Neurology, 2011. **258**(3): p. 366-372.

[175]   Sheldon, R., et al., *Risk factors for syncope recurrence after a positive tilt-table test in patients with syncope.* Circulation, 1996. **93**(5): p. 973-981.

[176]   Colivicchi, F., et al., *Cardiac autonomic derangement and arrhythmias in right-sided stroke with insular involvement.* Stroke, 2004. **35**(9): p. 2094-2098.

[177]   Cheng, R., et al., *Near-infrared Diffuse Optical Monitoring of Cerebral Blood Flow and Oxygenation for the Prediction of Vasovagal Syncope.* Journal of Cerebral Blood Flow and Metabolism (submitted), 2013.

[178]   Li, T., H. Gong, and Q. Luo, *Visualization of light propagation in visible Chinese human head for functional near-infrared spectroscopy.* J Biomed Opt, 2011. **16**(4): p. 045001.

[179]   Gagnon, L., et al., *Quantification of the cortical contribution to the NIRS signal over the motor cortex using concurrent NIRS-fMRI measurements.* Neuroimage, 2012. **59**(4): p. 3933-40.

[180]   Farrell, T.J., M.S. Patterson, and M. Essenpreis, *Influence of layered tissue architecture on estimates of tissue optical properties obtained from spatially resolved diffuse reflectometry.* Applied Optics, 1998. **37**(10): p. 1958-1972.

[181]   Carey, B.J., et al., *Carbon dioxide, critical closing pressure and cerebral haemodynamics prior to vasovagal syncope in humans.* Clinical Science, 2001. **101**(4): p. 351-358.

VITA

Ran Cheng, Ph.D. candidate
Department of Biomedical Engineering
University of Kentucky
Lexington, KY 40506-0070

EDUCATION

Huazhong University of Science and Technology, Wuhan, Hubei, China

B.E., Biomedical Engineering, June 2008

University of Kentucky, Lexington, Kentucky, USA

Ph.D. candidate, Biomedical Engineering, August 2008 - present

PROFESSIONAL POSITIONS

Research Assistant, Department of Biomedical Engineering, University of Kentucky, Lexington, KY

August, 2008 – present

HONORS AND ACTIVITIES

Outstanding Graduate Student of Department of Biomedical Engineering, University of Kentucky, 2013

Conference Travel Support Awards, University of Kentucky, 2010-2013

Delta Epsilon Iota Academic Honor Society, 2012-present

Treasurer, Biomedical Engineering Society, University of Kentucky Student Chapter, 2009-2011

PROFESSIONAL MEMBERSHIPS

Optical Society of America (OSA), 2010- 2012

Biomedical Engineering Society (BMES), 2009 - 2011

American College of Sports Medicine (ACSM), 2013 – present

PUBLICATIONS

Peer-reviewed Papers

1. **<u>R. Cheng</u>**, Y. Shang, S. Wang, J. Evans, A. Rayapati, D.C. Randall, G, Yu, "Near-infrared Diffuse Optical Monitoring of Cerebral Blood Flow and Oxygenation for the Prediction of Vasovagal Syncope" (**submitted**, 2013)

2. **<u>R. Cheng</u>***, X. Zhang*, A. Daugherty, H. Shin, G. Yu, "Noninvasive Quantification of Post-occlusive Reactive Hyperemia in Mouse Thigh Muscle by Near-infrared Diffuse Correlation Spectroscopy" (***co-first author, submitted,** 2013)

3. X. Zhang*, **<u>R. Cheng</u>***, D. Rowe, P. Sethu, A. Daugherty, G. Yu, H. Shin, "The Shear-sensitive Regulation of Neutrophil Flow Behavior and Its Putative Role in Microvascular Blood Flow Dysregulation in Hypercholesterolemia" (***co-first author, submitted,** 2013)

4. Y. Shang, Y. Lin, B. Henry, **<u>R. Cheng</u>**, C. Huang, K.R. Swartz, S.S. Salles, G. Yu, "Noninvasive Evaluation of Electrical Stimulation Impacts on Muscle Hemodynamics via Integrating Diffuse Optical Spectroscopies with Muscular Stimulator", *Journal of Biomedical Optics*, (**under revision**, 2013)

5. G. Yu, **<u>R. Cheng</u>**, J. Yang, Z. Yang, M. Xun, T. Liu, Y. Li, "Near-infrared diffuse correlation spectroscopy (DCS) for noninvasive monitoring of photodynamic therapy (PDT)," *International Journal of Biomedical Engineering*, Invited Review, (**In press,** 2013)

6. **<u>R. Cheng</u>**, Y. Shang, D. Hayes, Jr., S. P. Saha, G, Yu, "Noninvasive Optical Evaluation of Spontaneous Low Frequency Oscillations in Cerebral Hemodynamics", *NeuroImage,* 62(3), 1445-1454, 2012

7. L. Dong, M. Kudrimoti, **<u>R. Cheng</u>**, Y. Shang, E. L. Johnson, S. D. Stevens, B. J. Shelton, and G. Yu, "Noninvasive diffuse optical monitoring of head and neck tumor blood flow and oxygenation during radiation delivery," *Biomedical Optics Express*, *3,* 259-272, 2012

8. N. Munk. B. Symons, Y. Shang, **<u>R. Cheng</u>**, and G. Yu, "Noninvasively measuring hemodynamic effects of massage on skeletal muscle: a novel hybrid near infrared diffuse optical instrument", *Journal of Bodywork & Movement Therapies*, 16(1), 22-28, 2012

9. D. Irwin, L. Dong, Y. Shang, **<u>R. Cheng</u>**, M. Kudrimoti, S. D. Stevens and G. Yu, *"*Influences of tissue absorption and scattering on diffuse correlation spectroscopy blood flow measurements*" Journal of Biomedical Optics* 2, 1969–1985, 2011

10. Y. Shang, **R. Cheng**, L. Dong, S. J Ryan, S. P. Saha ang G. Yu, "Cerebral monitoring during carotid endarterectomy using near-infrared diffuse optical spectroscopies and electroencephalogra" *Physics in Medicine and Biology* 56, 3015–3032, 2011

11. G. Yu, Y. Shang, Y. Zhao, **R. Cheng**, L. Dong, and S. P. Saha, "Intraoperative evaluation of revascularization effect on ischemic muscle hemodynamics using near-infrared diffuse optical spectroscopies" *Journal of Biomedical Optics*, 16(2), 027004, 2011

12. Y. Shang, Y. Zhao, **R. Cheng**, L. Dong, D. Irwin, and G. Yu, "Portable optical tissue flow oximeter based on diffuse correlation spectroscopy", *Optics Letters*,34(22), 3556-3558, 2009

Book Chapter

13. G. Yu, T. Durduran, C. Zhou, **R. Cheng**, A. G. Yodh, "Near-infrared Diffuse Correlation Spectroscopy (DCS) for Assessment of Tissue Blood Flow", in "Handbook of Biomedical Optics*", Chapter 13*, D.A. Boas, C. Pitris, and N. Ramanujam, Editors, Taylor & Francis Books, Inc. (2010)

Conference Abstracts/Proceedings

1. X. Zhang, **R. Cheng**, D. Rowe, P. Sethu, G. Yu, A. Daugherty, H. Y. Shin, "The Contributory Role of Impaired Neutrophil Fluid Shear Mechanotransduction in Hypercholesterolemia-Related Dysregulation of Microvascular Blood Flow", BMES 2013 Annual Scientific Meeting, Seattle, WA, 2013 (**Oral Presentation**)

2. **R. Cheng**, X. Zhang, H. Shin, G. Yu, "Noninvasive quantification of skeletal muscle microvasculature blood flow in mouse thigh by diffuse correlation spectroscopy", 60th Annual Meeting of American College of Sports Medicine (ACSM), Indianapolis, IN, 2013

3. **R. Cheng**, Y. Shang, S. Wang, J. Evans, A. Rayapati, D.C. Randall, G. Yu, "Near-infrared Diffuse Optical Monitoring of Cerebral Blood Flow and Oxygenation for the Prediction of Vasovagal Syncope", CCTS Scientific Meeting & Appalachian Health Summit, Columbus, OH, 2013

4. **R. Cheng**, Y. Shang, D. Hayes, Jr., S. Saha, G. Yu, "Noninvasive Optical Evaluation of Spontaneous Low Frequency Oscillations in Cerebral Blood Flow and Oxygenation", CCTS Scientific Meeting & Appalachian Health Summit, Columbus, OH, 2013

5. **R. Cheng**, Y. Shang, S. Wang, J. Evans, A. Rayapati, D.C. Randall, G. Yu, "Near-infrared Diffuse Optical Monitoring of Cerebral Blood Flow and

Oxygenation for the Prediction of Vasovagal Syncope", Annual CCTS Spring Conference, Lexington, KY, 2013 (**Oral Presentation**)

6. X. Zhang, **R. Cheng**, A. Daugherty, G. Yu, H. Y. Shin, "Rheological Impact of Dysregulated Neutrophil Shear Stress Mechanotransduction on Hypercholesterolemia-Related Microvascular Pathophysiology", UK CCTS Spring Conference, Lexington, KY, 2013 (**Oral Presentation**)

7. **R. Cheng**, X. Zhang, H. Shin, G. Yu, "Noninvasive quantification of skeletal muscle microvasculature blood flow in mouse thigh by diffuse correlation spectroscopy", Muscle Retreat, Lexington, KY 2012

8. **R. Cheng**, Y. Shang, S. Saha, G. Yu, "Noninvasive Optical Evaluation of Spontaneous Low Frequency Oscillations in Cerebral Blood Flow and Oxygenation", Markesbery Symposium of Aging and Dementia, Lexington, KY, 2012

9. **R. Cheng**, Y. Shang, G. Yu, "Noninvasive Optical Evaluation of Cerebral Autoregulation in Patients with Obstructive Sleep Apnea", Markesbery Symposium of Aging and Dementia, Lexington, KY, 2012

10. Y. Shang, **R. Cheng**, L. Dong, S. J Ryan, S. P. Saha ang G. Yu, "Cerebral monitoring during carotid endarterectomy using near-infrared diffuse optical spectroscopies and electroencephalogra", Markesbery Symposium of Aging and Dementia, Lexington, KY, 2012

11. **R. Cheng**, Y. Shang, G. Yu, "Noninvasive Optical Detection of Spontaneous Low Frequency Oscillations in Cerebral Blood Flow", OSA Biomedical Optics (BIOMED), Miami, FL, 2012 (**Oral Presentation**)

12. L. Dong, M. Kudrimoti, **R. Cheng**, Y. Shang, E. L. Johnson, S. D. Stevens, B. J. Shelton, G. Yu, "Noninvasive diffuse optical monitoring of hemodynamic changes in head and neck tumor during radiation delivery", OSA Biomedical Optics (BIOMED), Miami, FL, 2012

13. L. Dong, D. Irwin, Y. Shang, **R. Cheng**, M. Kudrimoti, S. D. Stevens, and G. Yu, "Influences of Tissue Optical Properties on Diffuse Correlation Spectroscopy Blood Flow Measurements", OSA Biomedical Optics (BIOMED), Miami, FL, 2012

14. Y. Shang, **R. Cheng**, L. Dong, S. J. Ryan, S. P. Saha, G. Yu, "Comparison of diffuse optical spectroscopies and electroencephalogram for cerebral monitoring during carotid endarterectomy", OSA Biomedical Optics (BIOMED), Miami, FL, 2012

15. **R. Cheng**, Y. Shang, G. Yu, "Noninvasive Optical Detection of Spontaneous Low Frequency Oscillations in Cerebral Blood Flow", CCTS Spring Conference, Lexington, KY, 2012 (**Oral Presentation**)

16. **R. Cheng**, Y. Shang, G. Yu, "Noninvasive Optical Evaluation of Spontaneous Low Frequency Oscillations in Cerebral Blood Flow and Oxygenation", Gill Heart Cardiovascular Research Day, Poster Section, University of Kentucky, Lexington, KY, 2011

17. Y. Shang, **R. Cheng**, L. Dong, S.J. Ryan, S.P. Saha, and G. Yu, "Use of Diffuse Optical Spectroscopies and Electroencephalogram for Cerebral Monitoring During Carotid Endarterectomy", ECI (Engineering Conference International) conference Advances in Optics for Biotechnology, Medicine and Surgery XII, Naples, FL, USA, 2011.

18. Y. Shang, Y. Zhao, **R. Cheng**, L. Dong, S.P. Saha, and G. Yu, "Diffuse Optical Evaluation of Revascularization Effect on Ischemic Muscle Hemodynamics in Lower Extremities", ECI (Engineering Conference International) conference Advances in Optics for Biotechnology, Medicine and Surgery XII, Naples, FL, USA, 2011.

19. D. Irwin, L. Dong, Y. Shang, **R. Cheng**, M. Kudrimoti, S.D. Stevens, and G. Yu, "Influences of Tissue Absorption and Scattering on Diffuse Correlation Spectroscopy Blood Flow Measurements", ECI (Engineering Conference International) conference Advances in Optics for Biotechnology, Medicine and Surgery XII, Naples, FL, USA, 2011

20. B. Symons, N. Munk, Y. Shang, **R. Cheng**, and G. Yu, "*Lower Limb Massage Increases Skeletal Muscle Blood Flow in Young Women*" 58th Annual Meeting and 2nd World Congress on Exercise is Medicine of the American College of Sports Medicine 2011, Denver, CO, USA, 2011

21. D. Irwin, L. Dong, Y. Shang, **R. Cheng**, S. Steven, M. Kudrimoti, G. Yu, "Influences of Tissue Absorption and Scattering on Diffuse Correlation Spectroscopy Blood Flow Measurements in Head and Neck Tumors", UK Markey Cancer Research Day, Lexington, KY, 2010

22. Y. Shang, **R. Cheng**, L. Dong, D. Irwin, K. M. Gurley, K. R. Swartz, S. S. Salles, G. Yu, "Evaluation of Electronic Stimulation Impact on Muscle hemodynamics Using Diffuse Optical Spectroscopies", 23rd Annual Physical Medicine and Rehabilitation Research Day, Lexington, KY, 2010

23. Y. Shang, **R. Cheng**, L. Dong, S. P. Saha, and G. Yu, "*Detection of Cerebral Ischemia during Carotid Dendarterectomy using Near-Infrared Diffuse Optics Spectroscopies*", 52nd Annual World Congress, International College of Angiology (ICA) 2010, Lexington, KY, USA, 2010

24. **R. Cheng**, Y. Shang, G. Yu, and S.u P. Saha, "*Intraoperative Evaluation of Revascularization Effect on Ischemic Muscle Hemodynamics Using Near-infrared Diffuse Optical Spectroscipies*", 52nd Annual World Congress, International College of Angiology (ICA) 2010, Lexington, KY, USA, 2010 (**Oral Presentation**)

25. **R. Cheng**, Y. Shang, D. Kameny, D. Hayes, Jr., G. Yu, *"Noninvasive Optical Evaluation of Cerebral Autoregulation in Patients with Obstructive Sleep Apnea"*, in April, 2010 Biomedical Optics and 3-D Imaging, OSA Optics & Photonics Congress. Miami, FL, USA, 2010

26. Y. Shang, **R. Cheng**, L. Dong, S. P. Saha, and G. Yu, "Diffuse Optical Detection of Cerebral Ischemia During Carotid Endarterectomy*"*, in 2010 Biomedical Optics and 3-D Imaging, OSA Optics & Photonics Congress. Miami, FL, USA, 2010

27. Y. Shang, Y. Zhao, **R. Cheng**, L. Dong, D. Irwin, K. R Swartz, S. S. Salles, and G. Yu, "Diffuse Optical Spectroscopies for Evaluation of Muscle Hemodynamic Enhancements by Electrical Stimulation*"*, in 2010 Biomedical Optics and 3-D Imaging, OSA Optics & Photonics Congress. Miami, FL, USA, 2010

28. G. Yu, Y. Shang, Y. Zhao, **R. Cheng**, L. Dong, D. Irwin, and S. P. Saha, "Portable Optical Tissue Flow Oximeter for Evaluation of Revascularization Effect on Ischemic Muscle Hemodynamics*"*, in 2010 Biomedical Optics and 3-D Imaging, OSA Optics & Photonics Congress. Miami, FL, USA, 2010

29. G. Yu, Y. Shang, Y. Zhao, **R. Cheng**, L. Dong, D. Irwin, *"A portable optical tissue flow-oximeter based on diffuse correlation spectroscopy"*, in BiOS SPIE Photonics West. San Francisco, CA, USA, 2010 (**Oral presentation**)

30. Y. Shang, Y. Zhao, **R. Cheng**, L. Dong, S. P. Saha and G. Yu, "*Intraoperative assessment of acute revascularization effect on ischemic muscle perfusion and oxygenation*", The International Society for Optical Engineering (SPIE) Photonics West, San Francisco, CA, USA, 2010 (**Oral presentation**)

31. N. Munk, B. Symons, Y. Shang, **R. Cheng**, G. Yu, *"Measuring the Effects of Massage on Skeletal Muscle Blood Flow: A Novel Hybrid Near-Infrared Diffuse Optical Instrument"*, in 2010 Highlighting Massage Therapy in Complementary and Integrative Medicine (CIM) Research, Seattle, WA, USA, 2010

32. **R. Cheng**, Y. Shang, S. P. Saha, and G. Yu, "Intraoperative Evaluation of Revascularization Effect on Ischemic Muscle Hemodynamics Using Near-infrared Diffuse Optical Spectroscipies", UK Muscle Biology Fall Retreat, Lexington, KY, 2010

33. Y. Shang, Y. Zhao, **R. Cheng**, L. Dong, D. Irwin, K. R. Swartz, S. S. Salles, and G. Yu, "Diffuse Optical Spectroscopies for Evaluation of Muscle Hemodynamic Enchantments by Electrical Stimulation," UK Muscle Biology Fall Retreat, Lexington, KY, 2010

34. **R. Cheng**, Y. Shang, D. Kameny, D. Hayes Jr., G. Yu, "Noninvasive Optical Evaluation of Cerebral Autoregulation in Patients with Obstructive Sleep Apnea," UK Gill Heart Institute Cardiovascular Research Day, Lexington, KY, 2009

35. Y. Shang, **R. Cheng**, L. Dong, S. P. Saha, and G. Yu, "Detection of Cerebral Ischemia During Carotid Endarterectomy Using Near-infrared Diffuse Optical Spectroscopies", UK Gill Heart Cardiovascular Research Day, Lexington, KY, 2009

36. **R. Cheng**, Y. Shang, Y. Zhao, L. Dong, D. Hayes, Jr., G. Yu *, "Noninvasive Diffuse Optical Evaluation of Cerebral Autoregulation"*, in Fall Annual Meeting of the Biomedical Engineering Society. Pittsburgh, PA, USA, 2009

37. Y. Shang, Y. Zhao, **R. Cheng**, D. Irwin, L. Dong, K. R. Swartz, S. S. Salles, and G. Yu, "*Noninvasive Assessment of Muscle Hemodynamic Enhancement by Electrical Stimulation Using Diffuse Optical Spectroscopies*", Fall Annual Meeting of the Biomedical Engineering Society, Pittsburgh, PA, USA, 2009 (**Oral presentation**)

38. Y. Zhao, Y. Shang, **R. Cheng**, L. Dong, S. P. Saha, and G. Yu, "*Diffuse Optical Monitoring of Revascularization Effect on Skeletal Muscle Perfusion*", Fall Annual Meeting of the Biomedical Engineering Society, Pittsburgh, PA, USA, 2009

39. G. Yu, Y. Zhao, Y. Shang, **R. Cheng**, L. Dong, and S. P. Saha, "*Intraoperative Evaluation of Revascularization Effect on Ischemic Muscle Perfusion*", 2nd Photonics and OptoElectronics Meetings (POEM 2009), Wuhan, China, 2009

40. G. Yu, Y. Shang, Y. Zhao, **R. Cheng**, D. Irwin, Li. Dong, K. R. Swartz, and S. S. Salles, "*Diffuse Optical Evaluation of Muscle Hemodynamic Responses to Electrical Stimulation*", 2nd Photonics and OptoElectronics Meetings (POEM 2009), Wuhan, China, 2009 (**Oral presentation**)

41. Y. Shang, Y. Zhao, **R. Cheng**, L. Dong, S. P. Sibu, and G. Yu "Intraoperative Assessment of Acute Revascularization Effect on Ischemic Muscle Perfusion", Adult Skeletal Muscle Symposium: Clinical Problems, Molecular Targets, University of Kentucky, 2009

42. Y. Shang, Y. Zhao, **R. Cheng**, D. Irwin, L. Dong, K. R. Swartz, S. S. Salles, and G. Yu, "Noninvasive Assessment of Muscle Hemodynamic Enhancement by Electrical Stimulation Using Diffuse Optical Spectroscopies," Adult Skeletal Muscle Symposium: Clinical Problems, Molecular Targets, University of Kentucky, 2009